

ADVANCES IN ELECTROMETALLURGY

No. 4 Volume 8 2010

ELECTRON BEAM PROCESSES

- N. P. Tribug, V. A. Berezos, V. A. Kryzhanovskii and A.Yu. Severin*, Investigations of the processes of production of hot-rolled pipes from ingots of VT20 titanium alloy produced by electron beam melting 227
- S. V. Akhonin, M. P. Kruglenko and V. I. Kostenko*, Removal of refractory inclusions from titanium in electron beam melting by the precipitation mechanism 232
- A. I. Ustinov, S. A. Demchenkov, V. A. Telichko and S.S. Polishchuk*, Thermal stability of nanostructured $Al_{63}Cu_{26}Fe_{11}$ vacuum condensates 237
- V.O. Mushegyan and A.A. Tarasyuk*, The determination of the optimum conditions of electron beam heating in melting of molybdenum in MV-1 equipment 244

PLASMA-ARC TECHNOLOGY

- V. A. Shapovalov, K. A. Tsykulenko, I. V. Sheiko and V. I. Kolesnichenko*, Plasma metallurgy and service life of plasma torches 249

GENERAL PROBLEMS OF METALLURGY

- G. M. Grigorenko, Yu. M. Pomarin, V. V. Lakomskii, V. Yu. Orlovskii and I. I. Alekseenko*, Properties of Kh13-type steels alloyed with nitrogen 255

ELECTROMETALLURGY OF STEEL AND FERROALLOYS

- A. I. Panchenko, A. S. Salnikov and M. I. Gasik*, Development and application of the innovation technology of melting ShKh15SG-V ball bearing electric steel 259

NEW MATERIALS

- S. V. Maksimova and V. F. Khorunov*, Brazing of titanium aluminide with rapidly hardened foils 268
- I. S. Malashenko, V. E. Mazurak, V. V. Kurenkova, T. N. Kushnareva and Yu. V. Gusev*, Repair of flaps of the regulating nozzle of aviation gas turbine engines by high-temperature vacuum brazing 274

Advances in Electrometallurgy is a cover-to-cover English translation of *Sovremennaya Elektrometallurgiya*, published four times a year by International Association 'Welding' at the E.O. Paton Electric Welding Institute, National Academy of Sciences of Ukraine, 11 Bozhenko Street, 03680 Kyiv, Ukraine

Editor-in-Chief

B.E. Paton

Editorial Board

D. Ablitzer (France)

D.M. Dyachenko, Executive secretary (Ukraine)

J. Foct (France)

T. El Gammal (Germany)

M.I. Gasik (Ukraine)

G.M. Grigorenko, Deputy Chief editor (Ukraine)

B. Koroushich (Slovenia)

V.I. Lakomsky (Ukraine)

V. Lebedev (Ukraine)

S.F. Medina (Spain)

L.B. Medovar (Ukraine)

A. Mitchell (Canada)

B.A. Movchan (Ukraine)

A.N. Petrunko (Ukraine)

Ts.V. Rashev (Bulgaria)

N.P. Trigub (Ukraine)

A.A. Troyansky (Ukraine)

M.L. Zhadkevich (Ukraine)

All rights reserved. This publication and each of the articles contained here are protected by copyright. Permission to reproduce materials from this journal must be obtained in writing from the Publisher

Published by

Cambridge International Science Publishing Ltd
7 Meadow Walk, Great Abington, Cambridge CB21 6AZ, England
Tel: +44 (0) 1223 893295; Fax: +44 (0) 1223 894539
email: cisp@cisp-publishing.com; <http://www.cisp-publishing.com>

Removal of refractory inclusions from titanium in electron beam melting by the precipitation mechanism

S. V. Akhonin, M. P. Kruglenko and V. I. Kostenko

E.O. Paton Electric Welding Institute, Kiev; Strategiya BM Company, Kiev

Processes of removal of refractory inclusions of titanium in electron beam cold hearth melting are considered. The regularities are established for the process of gravitation precipitation on the surface of the skull of α -titanium particles, saturated with interstitial impurities, and inclusions in the form of nitrides and titanium oxides and carbides of refractory metals, allowing determination of the required dimensions of the cold hearth to provide guaranteed removal of refractory inclusions of titanium by their precipitation in electron beam melting.

An important problem for all industrial producers of titanium ingots and semifinished products is the task of removal from the metal of inclusions with the higher content of the α -phase stabilising interstitial impurities: nitrogen, oxygen and carbon, which consist of the solid particles of α -titanium, saturated with these impurities, and also from the chemical compounds of these elements with titanium – nitrides, oxides and carbides, and also complex compounds (of the type of oxycarbonitrides). In the literature, these inclusions are referred to as low density inclusions (LDI) [1].

The hardness of these inclusions is more than three times higher than that of the titanium matrix. In addition, they are susceptible to brittle fracture. Therefore, these particles are stress concentrators and the sources of nucleation of fatigue cracks [2], leading to the failure of highly stressed components for important applications and, consequently, to catastrophic breakdowns.

In addition to nitrogen-containing low-density inclusions, a serious problem in the titanium ingots is also caused by the inclusions formed by chemical compounds with high density and high melting point – the

so-called high-density inclusions (HDI) [3]. In most cases, the sources of these inclusions are the fragments of cutting tools based on the carbides of refractory metals (WC, MoC, etc) which penetrate into the metal together with the charge components, mostly shavings. The presence of the HDI-type inclusions in the components greatly reduces the fatigue characteristics of the metal.

It is very difficult to remove the LDI and HDI refractory inclusions by vacuum-arc remelting (VAR) and they are found in titanium even after triple VAR of billets [4]. The lower efficiency of the vacuum arc remelting technology in relation to the processes of refining titanium to remove the HDI and LDI inclusions is caused by the fact that the density of the majority of these inclusions is higher than that of the liquid titanium. After falling into the liquid metal pool, they rapidly descend to the bottom and are ‘frozen’ into the metal of the ingots at the solidification front.

The complete removal of the LDI and HDI inclusions is one of the most important tasks of improving the technology of melting ingots of titanium and its alloys used for the manufacture of components for important

applications.

The LDI and HDI inclusions are removed from liquid titanium by cold hearth remelting [5]. The heat source for the melt in the intermediate container is either the electron beam or plasma arc. The method of electron beam cold hearth melting of titanium is used most widely in industry (Fig. 1).

The intermediate container (cold hearth) has the form of a copper water-cooled surface, restricted by the walls, with one of the walls containing an orifice for the discharge of liquid metal (discharge spout). The charge, supplied from the loading chamber is melted in the cold hearth by electron beams.

The cold hearth is used for averaging the chemical composition and refining the melt to remove the impurities and inclusions. A skull forms on the bottom of the cold hearth in the form of a layer of solidified metal which protects the walls and the bottom against interaction with molten metal.

One of the main mechanisms for the removal of refractory inclusions from titanium is gravitational precipitation of the inclusions: in melting, the liquid metal in the cold hearth flows in the horizontal direction, whereas the inclusions with higher density in comparison with liquid titanium travel downwards under

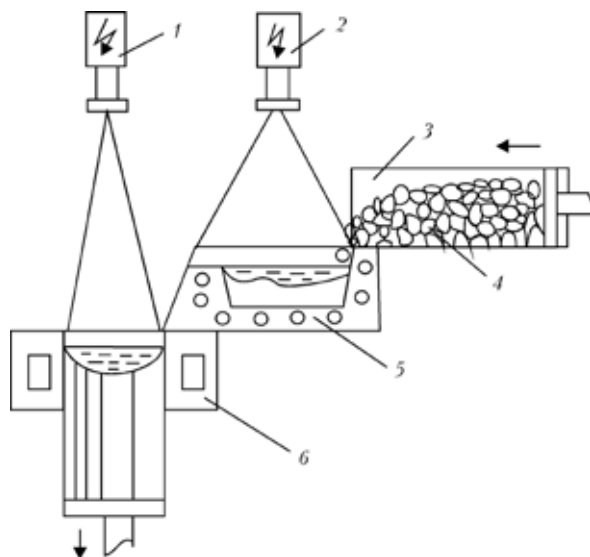


Fig. 1. The diagram of electron beam cold hearth melting: 1, 2) the electron beam guns; 3) the loading mechanism; 4) the initial charge; 5) the cold hearth; 7) the solidification mould.

the effect of the gravitational force (Fig. 2), settle on the surface of the skull and are 'frozen' in it.

To determine the relationships governing the removal of the LDI and HDI refractory inclusions from titanium in electron beam melting by the precipitation mechanism, it is taken into account that, according to the Stokes law, in the range of low Reynolds numbers ($Re < 100$) the speed of movement of the particles in the liquid is directly proportional to the driving force. The rate of precipitation v under the effect of gravitational force for a refractory particle in the form of a sphere can be calculated by the Stokes equation [6]:

$$v = \frac{2 \Delta \rho g r^2}{9 \eta}, \quad (1)$$

where $\rho = \rho_{in} - \rho_{Ti}$ is the difference between the densities of the inclusion and the liquid titanium, respectively, kg/m^3 ; g is the free-fall acceleration, m/s ; r is the radius of the inclusion, m ; η is the coefficient of viscosity of liquid titanium, $Pa \cdot s$.

Taking into account equation (1), the precipitation time of the refractory inclusion τ_s on the bottom of the liquid metal pool can be estimated using the following equation:

$$\tau_s = \frac{h}{v} = \frac{18 \eta h}{\Delta \rho g d^2}, \quad (2)$$

where h is the depth of the molten pool in the cold hearth, m ; d is the characteristic size of the inclusion, m .

It should be mentioned that the depth of the molten pool in the cold hearth in electron beam on melting usually does not exceed 0.03

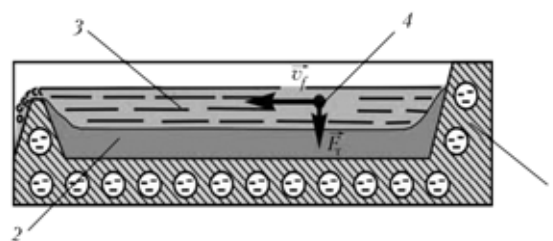


Fig. 2. The scheme of the process of precipitation of a refractory inclusion: 1) the cold hearth; 2) the skull; 3) the melt; 4) the refractory inclusion.

m. For the liquid metals, including titanium, the viscosity coefficient η may equal 5×10^{-3} Pa · s [6], and the density of liquid titanium equals 4110 kg/m^3 .

As an example, the precipitation time of a tungsten carbide inclusion with a density of $14\,000 \text{ kg/m}^3$ will be calculated (Fig. 3).

Analysis of the results shows that the high-density refractory inclusions precipitate at a high rate in the skull (the inclusion with a diameter of 0.5 mm passes through the thickness of the liquid molten pool in the cold hearth at a time of 0.25 s). The precipitation time of a high-density inclusion is inversely proportional to its size. For example, the precipitation time of an inclusion with a diameter $100 \text{ }\mu\text{m}$ is as long as 6 s .

An important technological and design parameter of electroslag remelting technology are the dimensions of the cold hearth whose length should be sufficient for the guaranteed precipitation of the refractory inclusion of the critical size. To determine the zone of the cold hearth in which the high-density refractive inclusions precipitate, it is necessary to determine the flow speed of the liquid titanium in the process of electron beam melting.

The linear flow speed of liquid titanium v_f is determined by the geometrical dimensions of the cold hearth and is linked by the following equation with the mass melting rate:

$$v_f = \frac{m}{3600 h S \rho_{\text{Ti}}}, \quad (3)$$

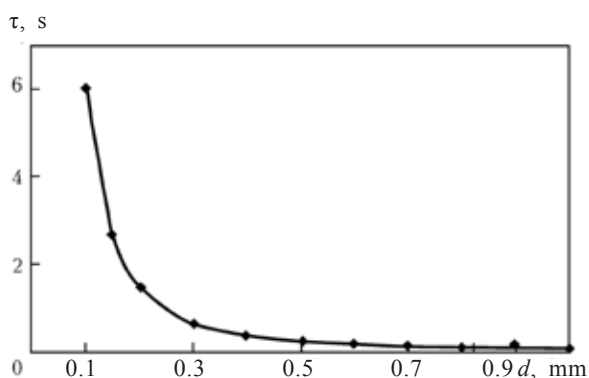


Fig. 3. Dependence of the precipitation time of a tungsten carbide inclusion on its diameter.

where m is the mass melting rate, kg/h; S is the width of the titanium melt flow in the cold hearth, m.

For example, for the width of the molten flow $S = 0.4 \text{ m}$, the depth of the molten pool in the cold hearth of $h = 0.03 \text{ m}$ and the mass melting rate of $m = 500 \text{ kg/h}$, the flow speed of liquid titanium is $3 \cdot 10^{-3} \text{ m/s}$.

In the case of penetration of a refractory inclusion with diameter d into the cold hearth prior to precipitation on the surface of the skull, the inclusion is carried by the liquid titanium flow over the distance L which can be calculated from the following equation:

$$L = v_f \tau_s = \frac{m \eta}{200 S \rho_{\text{Ti}} \Delta \rho g d^2}, \quad (4)$$

Assuming that the critical size of the refractory inclusion is $100 \text{ }\mu\text{m}$, using the equation (4) for the tungsten carbide it can be determined that the path of the inclusion up to the moment of falling into the cold hearth in the area of precipitation on the surface of the skull is 8 mm .

It should be noted that the distance over which the liquid metal carries the inclusion is independent of melting parameters that are difficult to determine, such as the depth of the pool. Consequently, the accuracy of the calculations can be greatly improved.

The most widely encountered type of low-density inclusions are the particles of α -titanium with a higher content of α -phase stabilising interstitial impurities (nitrogen, oxygen), formed during the production of titanium sponge. These inclusions amount to approximately 95% of all LDI refractive inclusions [7].

According to the equilibria diagrams of the titanium–nitrogen and titanium–oxygen assistance, the increase of the concentration of interstitial impurities in titanium increases the melting point of the titanium particles enriched with these impurities. For example, the melting point of α -titanium at a nitrogen content of more than 4.1% exceeds 2020°C (Fig. 4), whereas the melting point of pure titanium is 1668°C .

The density of titanium in the liquid state at room temperature is equal to 4500 kg/m³. To determine the density of the particles of α -titanium, saturated with nitrogen and oxygen at the melting point of titanium, it is assumed that the coefficient of linear expansion of titanium in the temperature range 20–16 60°C, according to the handbook data [8], can be approximated by the expression $\alpha = 1.04 \cdot 10^{-5} \text{ K}^{-1}$. Taking this into account, at the temperature of liquid titanium the linear dimensions of the inclusions increase by 1.7%, and the density of the particles of α -titanium equals 4278 kg/m³.

Thus, the difference of the density between the solid particles of α -titanium and liquid titanium is $\Delta\rho = 168 \text{ kg/m}^3$. Substituting the calculated values into the equation (4) gives the following dependence of the path L of the α -titanium inclusion up to the moment of its precipitation on the bottom of the molten pool in the cold hearth on the melting rate and the diameter of the inclusions:

$$L = \frac{3.7 \cdot 10^{-12} m}{Sd^2} \quad (5)$$

For example, for an α -titanium inclusion with a diameter 100 μm at a melting rate of 500 kg/h and the width of the titanium molten flow in the cold hearth of 0.4 m, the path L from the area of penetration equals 0.46 m (Fig. 5).

In addition to the refractory inclusions of α -titanium, the LDI inclusions can also be

represented by the particles of nitrides, oxides and carbides. To determine the possibility of removing these inclusions from the titanium melt, it is necessary to calculate the density of these inclusions at the liquid titanium temperature assuming that the coefficient of linear expansion of these inclusions is equal to that of titanium (Table 1).

Analysis of the results shows that in the process of electron beam melting all the refractory titanium inclusions with interstitial impurities, with the exception of titanium dioxide with different crystallographic structure, precipitate on the bottom of the cold hearth and are removed from the melt. The inclusions of the titanium carbide and titanium oxide of the same size will settle on the surface of the skull at the same distance from the area of penetration into the melt because the densities of these inclusions are practically identical. At the same time, the titanium dioxide inclusions rise to the surface of the melt under the effect of the Archimedes force.

Consequently, the refractive inclusions transferred by the titanium flow to the maximum distance from the area of penetration into the cold hearth are the particles of -tita-

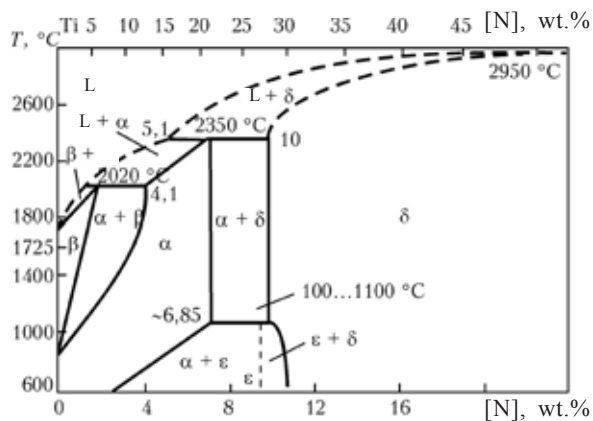


Fig. 4. The equilibrium diagram of the titanium–nitrogen system.

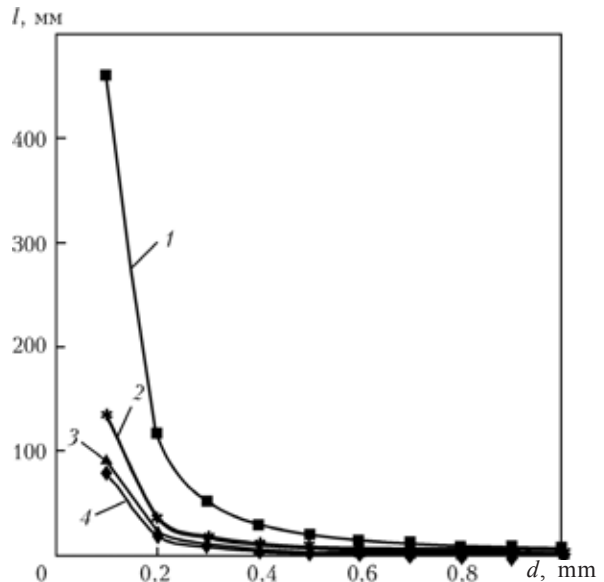


Fig. 5. Dependence of the path l of the low-density inclusion up to settling on the surface of the skull on the size of the inclusion: 1) α -Ti, 2) TiO, 3) TiN, 4) WC.

Table 1. The calculated density of some LDI inclusions at 1668°C

Type of inclusion	Density at 20°C, kg/m ³	Melting point, °C	Density at 1668°C, kg/m ³	$\Delta\rho = \rho_{in} - \rho_{Ti}$ at 1668°C, kg/m ³
Titanium nitride TiN	5210	2950	4952	842
Titanium carbide TiC	4940	3067	4696	586
Titanium oxide TiO	4930	1780	4686	576
Rutile TiO ₂	4235	1870	4026	-84
Anatase TiO ₂	4050	1870	3850	-260
Brookite TiO ₂	4120	1870	3916	-194

nium saturated with the interstitial impurities. Therefore, when designing the cold hearth ensuring guaranteed removal of the refractive inclusions by their precipitation, it is necessary to take into account the planned melting rate and calculate the dimensions of the cold hearth using equation (5).

Thus, in the process of electron beam melting of titanium almost all refractory inclusions of the LDI and aged TI type, with the exception of titanium dioxide inclusions, settle on the bottom of the cold hearth and are removed from the melt. The refractory inclusions, transferred by the titanium flow to the maximum distance from the area of penetration into the cold hearth, are represented mostly by the saturated interstitial impurities of the α -titanium particles. The relationships, determined in the present study,

can be used to determine the dimensions of the cold hearth ensuring guaranteed removal of the refractory inclusions from titanium by precipitation.

References

1. Henry J.L., et al., Met. Trans., 1973, No. 4, 1859–1864.
2. Koshelan A.V. and Raichenko A.I., Prots.Lit'ya, 1989, No. 3, 44–52.
3. Mitchel A., J. Vac, Technol., 1987, No. 4, 2672–2677.
4. Musatov M.I., et al., The development of melting of defects free ingots, in: Science, production and application of titanium in the conversion conditions, VILS, Moscow, 1994, 226–233.
5. Paton B.E., et al., Electron beam melting of titanium, Naukova Dumka, Kiev, 2006.
6. Popel' S.I., et al., The theory of metallurgical processes, Metallurgiya, Moscow, 1986.
7. Bellot J.P., et la., Light Metals, 1984, No. 2, 1187–1193.
8. Smitlz K.G., Metals, a handbook, Metallurgiya, Moscow, 1980.

Thermal stability of nanostructured $\text{Al}_{63}\text{Cu}_{26}\text{Fe}_{11}$ vacuum condensates

A. I. Ustinov, S. A. Demchenkov, V. A. Telichko and S.S. Polishchuk

E.O. Paton Electric Welding Institute, Kiev

Using the method of in-situ X-ray diffraction, the thermal stability in the process of heating of nanostructured vacuum condensates, produced by the method of electron-beam vacuum deposition of alloy $\text{Al}_{63}\text{Cu}_{26}\text{Fe}_{11}$, with the chemical composition similar to that of the quasi-crystal phase, was studied. It is shown that the vacuum condensates in the nanostructured state are heterophased and transform during heating to the icosahedral structure by a number of structural transformations. The temperature range of existence of intermediate phases are determined.

Introduction

The alloys with a complicated crystal structure (CCS), which include the quasi-crystals and approximants, are regarded, because of the unique combination of the properties, as promising materials for the development of coatings for functional applications [1–9].

In our previous studies it was shown for the first time that the method of electron beam deposition can be used for the formation of thick vacuum condensates with the quasi crystalline structure based on the Al–Cu–Fe alloy whose composition is close to the composition of the equilibrium quasi-crystalline phase, directly in the deposition process.

In addition, the experimental results show that the substrate temperature influences the microstructure of the deposited coatings: at the substrate temperature lower than 350°C, the grain size decreases to the nanoscale level [3, 4].

It was also shown that the nanostructured vacuum condensates with the CCS are characterised by higher strength properties, in comparison with the vacuum condensates with large grains. The high damping capac-

ity of the CCS enables them to be used as the coatings for suppressing the resonance vibrations in thin wall components, subjected to vibrational loading [4–6].

To evaluate the possibilities of using these materials as coatings for components working in the conditions of higher temperatures, investigations were carried out into the thermal stability of the nanostructured vacuum coatings produced as a result of electron beam deposition of the alloy with the $\text{Al}_{63}\text{Cu}_{26}\text{Fe}_{11}$ composition, similar to the composition of the icosahedral phase (*i*-phase), on substrates at temperatures lower than 300°C.

Examination by the method of in situ x-ray diffractometry of the nanostructured vacuum condensates in the process of continues heating in vacuum to temperatures close to the melting point of the alloy shows that this structure of the vacuum condensates is unstable and changes to the stable icosahedral phase through a number of intermediate phases.

Experimental procedure

The separated vacuum condensates with a

thickness of 50–60 μm were produced from the same source by the method of electron beam deposition (EB-PVD) on a steel substrate at a temperature of 250–300°C. The deposition rate was 2–3 $\mu\text{m}/\text{min}$. The source of the vapour phase was an ingot of $\text{Al}_{63}\text{Cu}_{26}\text{Fe}_{11}$ alloy with a diameter of 50 mm, 200 mm long, placed in a copper water-cooled crucible. The composition of the ingot was selected on the basis of the experimental results according to which the deposition of the vapour phase of the $\text{Al}_{63}\text{Cu}_{26}\text{Fe}_{11}$ alloy on the substrate at a temperature higher than 550°C leads to the formation of single-phase quasi-crystalline vacuum condensates.

The distribution of the chemical elements in the thickness of the vacuum condensates was determined in an Energy 200 energy-dispersing spectrometry module, fixed to the CamScan-4 scanning electron microscope.

The microstructure was examined by the methods of transmission electron microscopy in a Hitachi-800 electron microscope.

X-ray diffraction investigations of the structure of the produced vacuum condensates immediately after cooling and continuous heating were carried out in the standard geometry θ - 2θ in a DRON-4M diffractometer in $\text{Co}_{K\alpha}$ radiation.

The phase transformations in Al–Cu–Fe vacuum condensates were investigated by the method of high-temperature in situ x-ray diffraction in the irradiation of a cobalt anode in the temperature range 20–810°C, with a heating rate of approximately 10°C/min using UVD-2000 equipment in vacuum at a residual pressure of approximately $1 \cdot 10^{-3}$ Pa.

The diffraction diagrams were recorded using a bent linear position-sensitive detector (LPSD) of the flow type, working with the gas xenon–methane mixture (Fig. 1). The aperture of the LPSD ensured simultaneous recording of diffracted radiation in the angle range 40°, the focusing radius of the chamber of the detector was 200 mm, the angular resolution capacity 0.03°. To determine the coordinates of the recorded quantum, the LPSD used the time circuit of decoding the position information, taking into account

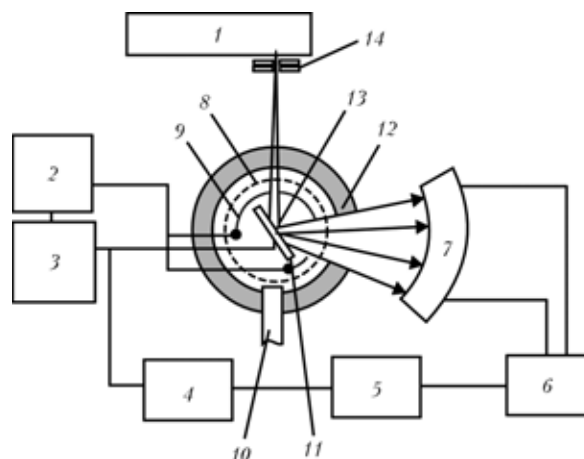


Fig. 1. Principal diagram of the high-temperature diffractometer using the linear position-sensitive detector for recording diffracted radiation: 1) x-ray tube, 2) the power source for the heat, 3) high-accuracy temperature regulator, 4) computer, 5) multichannel analyser, 6) signals transformer, 7) linear position-sensitive detector, 8) radiator for ensuring uniform heating of the specimen, 9) heater, 10) output to the diffusion pump, 11) specimen, 12) chamber, 13) thermocouple, 14) vertical and horizontal slits.

the difference in the duration of movement of the charge along the delay line from the area of collection to the resistance of the load of the line.

The information on the recording coordinate and the intensity of the deflected radiation was transferred through multichannel analyser to the input of a computer where data on the temperature of the specimen, arriving to the input of the computer through an analog–digital converter directly from the thermocouple, was also recorded. Continuous heating of the specimen was ensured using a high-precision temperature regulator, regulating the power of the heater in relation to the level of the signal, taken from the thermocouple.

Experimental results and discussion

Figure 2 shows the typical image of the cross-section of the vacuum condensates, characterised by a relatively high-density structure (without visible pores and inclusions) with a layered contrast. The alternation of the dark and light bands was nonuniform and changed in the range 1–5 μm . The distribution of the chemical elements of the thickness of the vacuum condensates indicates that it is

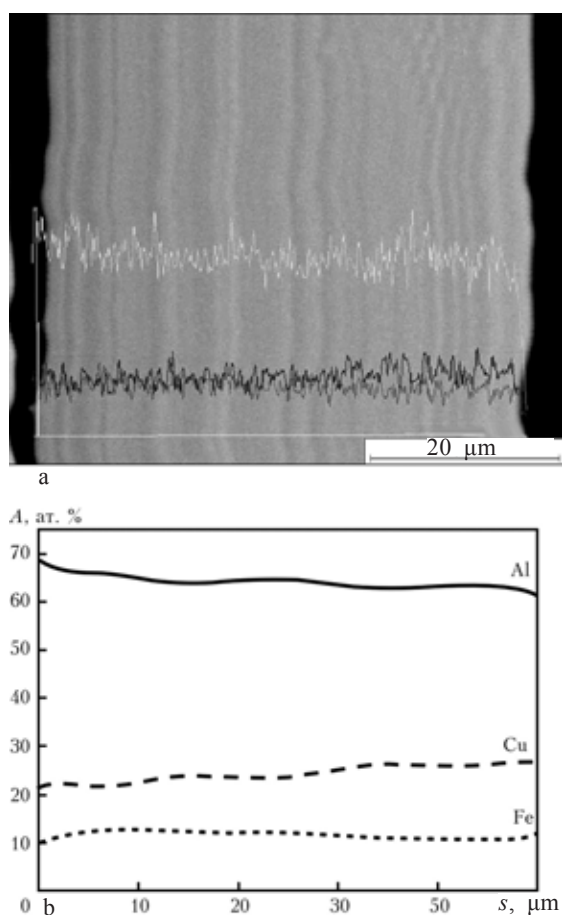


Fig. 2. Microstructure (a) and the variation of the chemical composition in the cross-section of the vacuum condensate based on the $\text{Al}_{63}\text{Cu}_{26}\text{Fe}_{11}$, deposited at a substrate temperature of 250–300°C (b); s is the thickness of the condensate, A is the chemical composition.

nonuniform, the deviation from the chemical composition of the $\text{Al}_{63}\text{Cu}_{26}\text{Fe}_{11}$ ingot is on average ± 2 at.%. When the local variation of the chemical composition in contrast of the microstructure images is compared, it may be seen that the darker interlayer is of the laminated structure of the vacuum condensates correlate with the increase of the aluminium concentration in the layer in contrast to the lighter interlayer. The probable reason for the formation of the laminated structure of the vacuum condensates may be the fluctuations of chemical composition of the vapour phase in evaporation of the multicomponent ingot.

The results of x-ray phase analysis of the deposited condensates are presented in Figure 3.

The diffraction diagram is characterised

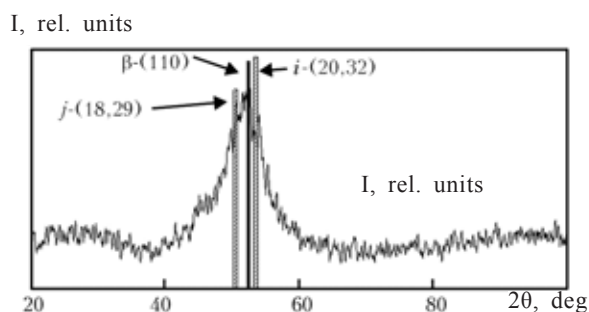


Fig. 3. Diffraction diagram (recorded in $\text{Co}_{K\alpha}$ radiation) of a vacuum condensate deposited at a substrate temperature of 250–300°C, immediately after deposition; I is intensity.

by a single wide peak in the range 40–60° with the maximum intensity in the range 52°. This diffraction pattern is similar to that of detected in the case of the amorphous structures. However, the amorphous-like diffraction peak on the diffraction diagram is situated in the angular range, corresponding to the position of the two most intensive diffraction peaks, characteristic of the quasi-crystalline structure and may be caused by overlapping of the peaks [4].

Evidently, this overlapping is the consequence of the widening of the diffraction peaks as a result of the reduction of the size of the crystals. In addition, the reduction of the substrate temperature may be accompanied not only by the reduction of the crystal size but also by the formation of diffraction peaks from the nanosized inclusions of the β -phase [4, 5]. The highest intensity peaks of this phase is situated in the same angle range.

Thus, the experimentally detected ‘x-ray amorphous’ structure of the vacuum condensates may be determined by their nanostructural condition, formed by the nanograins of the individual phases. To verify the assumption, the nanostructured state of the vacuum condensates was investigated by electron microscopic techniques.

Figure 4 shows the electron micro diffraction pattern of the structure of the $\text{Al}_{63}\text{Cu}_{26}\text{Fe}_{11}$ vacuum condensates. The presence of the continuous diffraction rings and the absence of the diffusion halo indicate the formation of the nanosized crystal structure. Analysis of the circular electron diffraction patterns

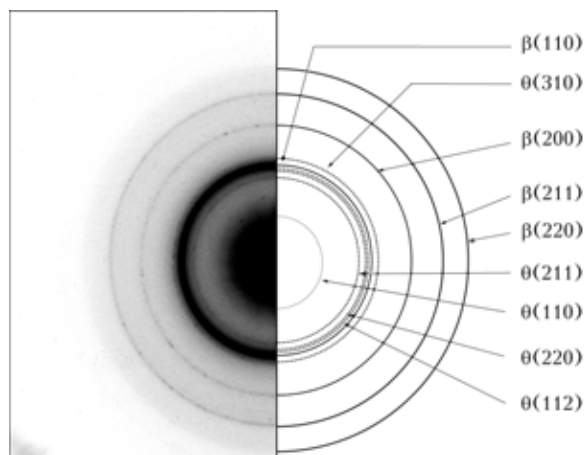


Fig. 4. Electron microdiffraction diagram of the structure of the $\text{Al}_{63}\text{Cu}_{26}\text{Fe}_{11}$ vacuum condensates.

indicates that the phase composition of the vacuum condensates is determined mainly by two phases: the cubic β -Al (Cu, Fe) phase and tetragonal θ - Al_2Cu phase.

The formation of a similar phase composition was also recorded in the initial stages of solid-phase reactions in the annealing of a mechanically activated mixture of the powders of aluminium, copper and iron in the composition $\text{Al}_{62}\text{Cu}_{25.5}\text{Fe}_{12.5}$ in the temperature range approximately 20–350°C [10–13] and the Al–Cu–Fe thin films produced by magnetron deposition of the $\text{Al}_{63}\text{Cu}_{26}\text{Fe}_{12}$ alloy at a temperature of 400°C [14].

Thus, the formation of the single wide diffraction peaks on the diffraction diagrams is determined by the nanostructured state of the vacuum condensates and associated mostly with the nanosized crystals of the β -phase whose size, according to the results of analysis of the physical width of the diffraction peaks, is less than 10 nm.

Figure 5 shows the characteristic x-ray diffraction patterns for several temperatures in the angle range $2\theta = 45\text{--}60^\circ$, obtained in continuous heating of the $\text{Al}_{63}\text{Cu}_{26}\text{Fe}_{11}$ vacuum condensates, deposited at a substrate temperature of 250–300°C. This angle range was selected as most representative with the most intensive peaks from the phases which may form as a result of phase transformations.

The diffraction diagrams shows that the nanostructured state (NSS) of the vacuum

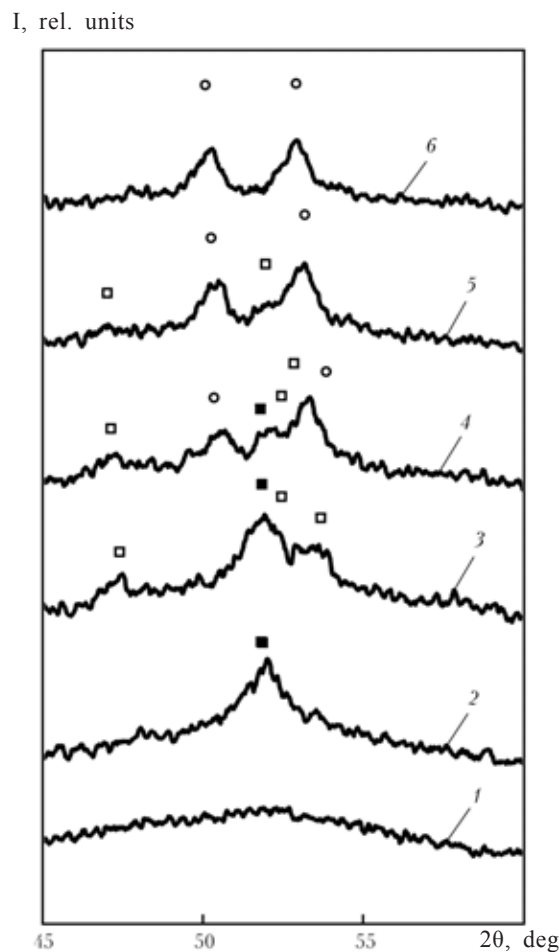


Fig. 5. Fragments of x-ray diffraction diagrams recorded in the process of continuous heating of the $\text{Al}_{63}\text{Cu}_{26}\text{Fe}_{11}$ vacuum condensate deposited at substrate temperatures of 250–300°C, heated to the following temperatures, °C: 1) 75; 2) 215; 3) 450; 4) 580; 5) 690; 6) 800; ■ – β -Al (Cu, Fe); □ – ω - $\text{Al}_7\text{Cu}_2\text{Fe}$; ○ – i -(AlCuFe).

condensate (up to 200°C) do not undergo any significant changes – the distribution of intensity in the investigated angular range remains almost constant. In heating above 200°C a narrower diffraction peak forms on the background of one amorphous-like peak in deposition typical of the β -phase. A further increase of the temperature of the specimen is accompanied by the increase of intensity of this diffraction peak to almost 400°C. The temperatures in the vicinity of 400°C close to the diffraction peak of the β -phase are characterised by the formation of an additional diffraction peak in deposition corresponding to the ω - $\text{Al}_7\text{Cu}_2\text{Fe}$ -phase. A further increase of the temperature reduces the intensity of

the diffraction peak of the β -phase, with a simultaneous increase of the volume fraction of the tetragonal ω -phase.

At temperatures of approximately 510–520°C, in addition to the reduction of the intensity of the diffraction peak of the β -phase, investigations show the formation of the diffraction peaks, typical of the quasi crystalline i -(AlCuFe)-phase.

Thus, the condensate is characterised by the formation of a heterophase state, containing ω -, β - and i -phases. A further increase of the temperature is accompanied by the processes of reduction of the volume fraction of the β -phase and by the increase of the volume fraction of the i - and ω -phases. This processes controlling in the temperature range 520–580°C. The diffraction peak from the β -phase completely disappears.

In heating above 590–600°C the volume fraction of the ω -phase in the condensate decreases and this is accompanied by the increase of the volume fraction of the i -phase after the formation in the vacuum condensates of the single-phase state at temperatures higher than 710°C.

A further increase of temperature to 810°C inclusive results in no changes in the structure of the vacuum condensates. After calling to room temperature, the quasi-crystalline structure of the vacuum condensate remains almost completely unchanged (Figure 6). The fragments of the diffraction diagram shows that all the diffraction peaks can be regarded as the peaks belonging to the icosahedral at quasi-crystalline phase [15].

Analysis of the physical with of the diffraction peaks of the intermediate and final phases indicates that the size of the crystals in the separated vacuum condensate during heating is slightly increases but remains smaller than 200 nm.

Thus, in the continuous heating of the nanostructured vacuum condensates based on the $\text{Al}_{63}\text{Cu}_{26}\text{Fe}_{11}$ alloy, whose chemical composition is close to the composition typical of the icosahedral phase, there were phase transformations, which can be described by the following chain:

I, rel. units

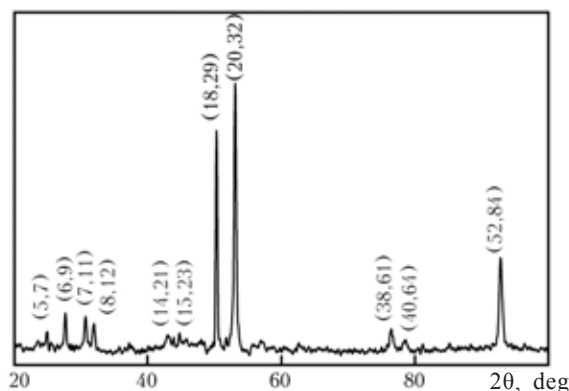
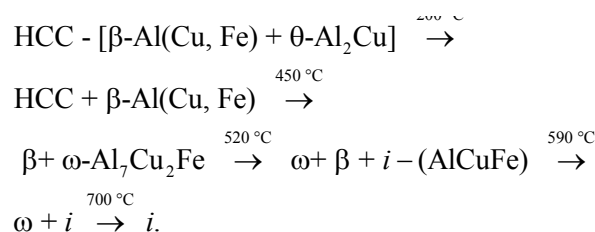


Fig. 6. X-ray diffraction diagram (recorded in CoK_{α} radiation) of the $\text{Al}_{63}\text{Cu}_{26}\text{Fe}_{11}$ vacuum condensate, at room temperature after continuous heating to 810°C.



In the first stage of the structural transformations in heating the nanocrystalline structure, the dominant process is the increase of the size of the crystals of the β -phase. This process may develop under the effect of the thermodynamic stimulus directed to reducing the specific surface of the boundaries of the nanocrystals. The low thermal activation of the process is supported by the presence in the vacuum condensates, obtained at the low deposition temperature, of the high concentration of nonequilibrium vacancies [16]. Other same time, it is also necessary to consider the effect of the two-phase state of the vacuum condensates on the structural transformations in heating. The interaction of the β -phase with the θ -phase may lead to the dissolution of the former and support the growth of the grains of the β -phase and the nucleation of the new $\omega\text{-Al}_7\text{Cu}_2\text{Fe}$ -phase as a result of the local change of the chemical composition of the β -phase and the displacement of the composition of the concentration region of existence of the ω -phase.

Thus, it may be assumed that this after

completing the process of growth of the grains of the β -phase in the initial stage of heating of the vacuum condensates, the latter remain chemically heterogeneous and this results in the transformation of the β -phase to the icosahedral structure through the intermediate ω -Al₇Cu₂Fe-phase.

A similar sequence of the phase transformations was detected in non-isothermal annealing of a mechanically activated mixture of the powders of aluminium, copper and iron with the ratio 62.0–25.5–12.5 at.% [10–13]. However, in annealing of the mechanically activated mixture of the powders, the formation of the ω -Al₇Cu₂Fe phase also observed at temperatures of approximately 350–380°C, and in the case of the vacuum condensates the formation of the ω -phase was recorded at a temperature of approximately 450°C. This may be associated with different heating rates of the specimens.

At the same time, the nucleation of the quasi crystalline *i*-phase in the vacuum condensates was detected at temperatures of approximately 520°C which is 70–80°C lower than in annealing of the mechanically activated mixture of the powders.

The formation of the single-phase quasicrystalline condition in annealing of the mechanically activated mixture of the powders was also observed at a higher temperature (approximately 750 in comparison with 700°C in the case of vacuum condensates).

Evidently, this may be associated with the presence of a large number of vacancy-type of defects formed in the vacuum condensates produced at low temperatures, and with extensive activation of the movement of the defects above the specific temperature (approximately 500°C) leading to the formation of the quasi crystalline phase at lower temperatures.

Conclusions

1. The experimental results show that the chemical composition of the Al₆₃Cu₂₆Fe₁₁ vacuum condensates is close to the chemical composition of the equilibria icosahedral phase produced by the methods of electron

beam deposition at substrate temperatures lower than 300°C, and the vacuum condensates have a hotel phase condition formed by the nanosized particles of the cubic phase β -Al (Cu, Fe) and the tetragonal θ -Al₂Cu phases.

2. The experimental results also show that the nanostructured state of the heterophase vacuum condensates is thermally unstable and transforms in subsequent heating to a stable icosahedral phase through the intermediate tetragonal ω -Al₇Cu₂Fe-phase.

3. It was found that the formation temperature of the icosahedral phase in continuous heating of the Al₆₃Cu₂₆Fe₁₁ vacuum condensates is lower than in the annealing of the mechanically activated mixture of the aluminium, copper and iron powders with the ratio 4.95:2.04:1.00 (atomic fractions) by 70–80°C.

References

1. Sordelet D. J., Dubois J. M. Perspectives and potential applications, MRS Bulletin, 1997, No. 22, P. 34–36.
2. Huttunen-Saarivirta E.. Microstructure, fabrication and properties of quasicrystalline Al–Cu–Fe alloys: a review, J. Alloys&Compounds, 2004, No. 363, P. 150–174.
3. Ustinov A.I., et al., Nanosisyemi, nanomateriali, naktekhnologii, 2004, No. 1, P. 203–213.
4. Structure and properties of quasicrystalline and approximant EB-PVD coatings of Al-based systems / A. Ustinov, S. Polishchuk, V. Skorodzievskii, V. Telychko, Z. Kristallogr., 2009, No. 224, P. 9–12.
5. Effect of grain size on damping capacity of quasicrystalline Al–Cu–Fe materials / A. I. Ustinov, S. S. Polishchuk, V. S. Skorodzievskii, V. V. Bliznuk, Surface & Coating Technology, 2008, No. 202, P. 5812–5816.
6. Ustinov A. I., Movchan B. A., Polishchuk S. S. Formation of nanoquasicrystalline Al–Cu–Fe coatings at electron beam physical vapor deposition, Scr. Mater, 2004., No. 50, P. 533–537.
7. Dubois J. M. New prospects from potential applications of quasicrystalline materials, Mater. Sci. Eng. A., 2000, No. 4, P. 294–296.
8. Comparative study of microstructural and tribological properties of sintered, bulk icosahedral samples, P. Brunet, L. M. Zhang, D. J. Sordelet et al., Ibid, 2000, No. 74, P. 294–296.
9. About the Al 3p density of states in Al–Cu–Fe compounds and its relation to the compound stability and apparent surface energy of quasicrystals, E. Belin-Ferre, J. M. Dubois, V. Fournee et al., Ibid, 2000, No. 818, P. 294–296.

10. In-situ time-resolved X-ray diffraction investigation of the wOy transition in Al–Cu–Fe quasicrystal-forming alloys, E. Otterstein, R. Nicula, M. Stir et al., *Mater. Sci. Forum*, 2007, No. 558/559, P. 943–947.
11. Quasicrystal phase formation in Al–Cu–Fe nanopowders during field-activated sintering (FAST), R. Nicula, F. Turquier, M. Stir et al., *J. Alloys & Compounds*, 2007, No. 434/435, P. 319–323.
12. Crystallochemical aspects of solid state reaction in mechanically alloyed Al–Cu–Fe quasicrystalline powders, A. I. Salimon, A. M. Korsunsky, E. V. Shelenkov et al., *Acta mater*, 2001, No. 49, P. 1821–1833.
13. Formation and stability of single-phase Al–Cu–Fe quasicrystals under pressure, F. Turquier, V. D. Cojocaru, M. Stir, et al., *Rev. Adv. Mater. Sci*, 2004, No. 8, P. 147–151.
14. Widjaja E. J., Marks L. D. Microstructural evolution in Al–Cu–Fe quasicrystalline thin films, *Thin Solid-Films*, 2003, No. 441, P. 63–71.
15. Cahn J. W., Schechtman D., Gratias D. Indexing of icosahedral quasiperiodic crystals, *J. Mater. Res*, 1986, No. 1, P. 13–26.
16. Positron annihilation study of vacancy-type defects in stoichiometric and non-stoichiometric Al–Cu–Fe quasicrystalline alloys, V. S. Mikhalekov, E. A. Tsapko, S. S. Polishchuk, A. I. Ustinov, *J. of Alloys and Compounds*, 2005, No. 386, P. 192–196.

The determination of the optimum conditions of electron beam heating in melting of molybdenum in MV-1 equipment

V.O. Mushegyan and A.A. Tarasyuk

Paton-Armenia E.O. Paton Electric Welding Institute, Kiev; Kiev Technical University KPI

The method of electron beam heating in melting of refractory metals with a cold hearth in MV-1 equipment is analysed. The optimum conditions of the effect of overlapping beams with compensation of superheating are determined. The procedure can be used for melting Mo ingots with the required chemical composition and high-quality surface.

Electron beam melting (EBM) together with vacuum-arc remelting (VAR) is the classic method of refining the melt and of the production of ingots of refractory metals [1, 2]. As a result of the high concentration of energy, flexibility and precision control, the electron beam is capable of melting and superheating the metals with the highest melting points, including molybdenum, whose melting point is 2617°C.

In contrast to vacuum arc melting where there are considerable restrictions in the selection of the re-melted material with respect to both the dimensions and purity (the content of impurities), electron beam melting is characterised by the maximum efficiency of removal of the harmful impurities and gases even from the metal with the highest degree of contamination, and there are almost no restrictions on the preparation and nature of the initial remelted material [3].

The electron beam melting of molybdenum is usually carried out directly in a solidification mould with the vertical or horizontal supply of a bar-shaped charge, or mostly in the form of compacted and subsequently sintered 'bars' [4].

To obtain a higher degree of purity of the

metal as a result of removal of the impurities, it is sometimes recommended to carry out double droplet remelting of the molybdenum material in a solidification mould. Electron beam cold hearth melting (EBCHM) offers even greater possibilities in the melting of a low-grade molybdenum charge: since the processes of melting and solidification do not depend on each other, the elements of the charged do not have to be bonded together, and the efficiency of removal of impurities from the metal increases as a result of additional holding in the cold hearth [5].

At the same time, to ensure the efficient control of the EBCHM process, it is necessary to control efficiently the distribution of the power of the electron beams with respect to all elements of the technological equipment - the zone of melting the charge in the feed device, the cold hearth and the solidification mould. This is carried out by the scanning and sweeping the electron beams of different configuration.

The Chistoe Zhelezo company, Erevan, Armenia, remelts the molybdenum concentrate in the form of sintered briquettes reduced from the concentrate (TU RE 28-54-529-61-661-2007) in MV-1 electron beam equipment,

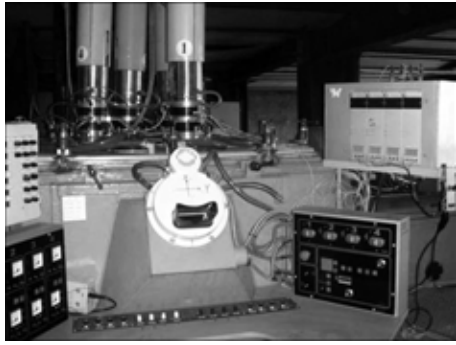


Fig. 1. MV-1 electron beam equipment (the control panel and a four electron beam guns).

developed at the Paton-Armenie Scientific and Technical Centre of the E.O. Paton Electric Welding Institute, Kiev, (Fig. 1) into ingots with a diameter of 70-130 mm [6].

Equipment uses for the first time the technology of melting molybdenum with a cold hearth and glow discharge electron beam guns [7]. This is caused by the need for the maximum 'cleaning' of the unconventional initial charge – sintered molybdenum briquettes with a diameter of 50 mm, 50–100 mm long, purity 98.5%.

The process of the melting molybdenum in the MV-1 equipment can be conventionally divided into several stages: preheating of the briquettes to ensure the release of gases, melting of the briquettes in the cold hearth and holding the metal in the molten condition; pouring the metal into the solidification mould and heating the surface of the metal in the mould for the formation of a high quality ingot.

Taking into account the high melting point of Mo, to ensure the required parameters of the productivity of melting and the efficiency of removal of impurities from the metal, the equipment contains four electron beam guns with a power of 100 kW each, which ensure functionally the above described stages of heating in the dynamic regime. The diagram of heating the metal in electron beam cold hearth melting of molybdenum in MV-1 equipment is shown in Fig. 2.

For each gun or a group of guns has a set of essential programs in the form of the

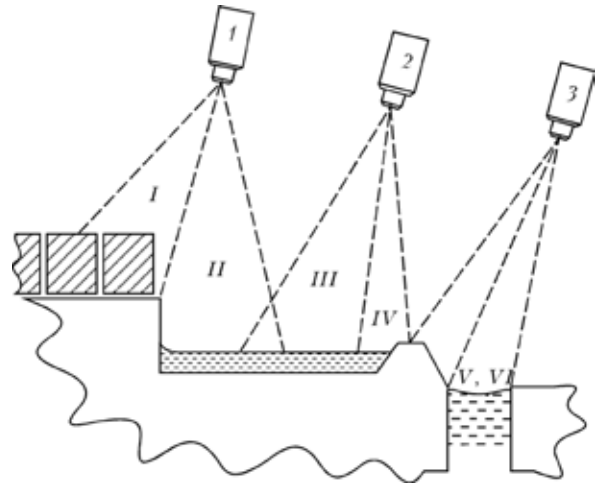


Fig. 2. Diagram of heating the consecutive working zones: I) the heating of molybdenum briquettes; II) melting in the cold hearth; III) maintenance of the liquid pool and the cold hearth, IV) maintaining discharge into the solidification mould; V, VI) heating of molybdenum in the solidification mould; VII) heating of the barrier in discharge and cleaning of the spout, 1) EBG1, EBG2; 2) EBG3, 3) EBG4.

sweeps of the electron beams within the limits of the given parameters using the modulation of the distribution of power in accordance with the selected melting conditions.

The selection and programming of the conditions of controlling heating are carried out using the control unit of the electron beam guns ARME 01, ensuring the following conditions of controlling the four-channel devices: the point – focusing of the beams in a point; the ring – the ring-shaped sweep of the beam takes place in the fourth channel; heating of the container – the third channel is characterised by sweep for the coating of the rectangular area; heating of the solidification mould – the fourth channel is characterised by the gradual formation of rings of different diameter for the coating, corresponding to the sweep of the filled circle; the frequency – the required frequency of repetition of the sweep is selected (the range of frequencies regulated by the sweep from 1 to 200 Hz); the distribution of power – the redistribution of power between the two types of sweep (the distribution of power between the sweeps is selected as the ratio is 25:75, 50:50, 0:100, etc); decrease – the transfer of

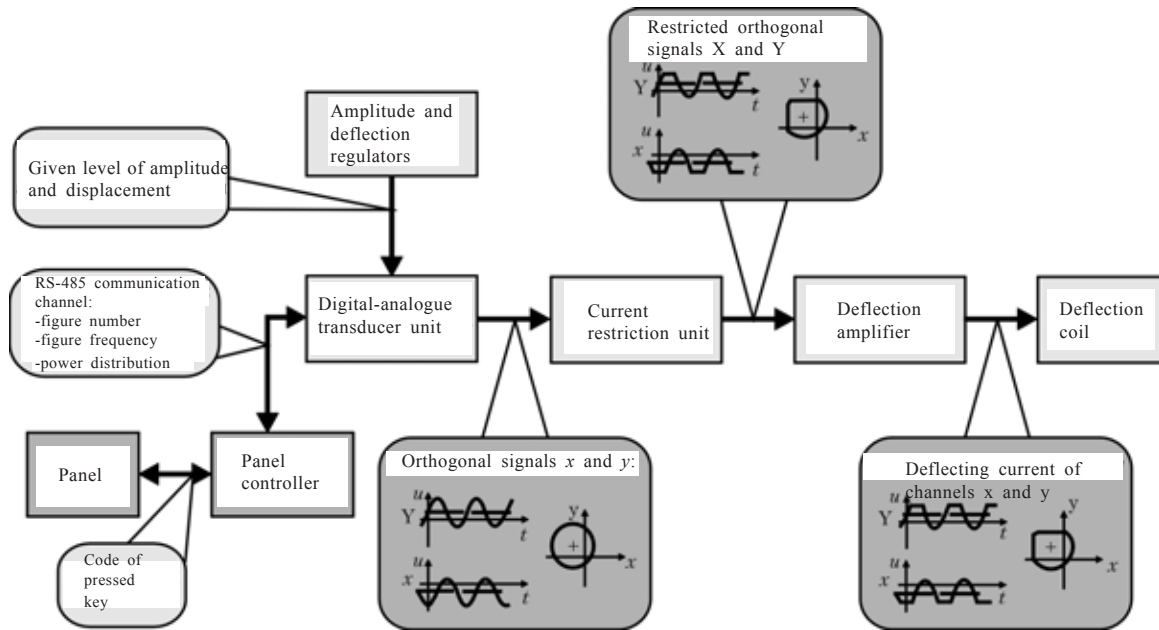


Fig. 3. The flow diagram of the working algorithm of ARME 01 equipment.

the control program to the initial states; the centre - three?.

The flow diagram of ARME 01 equipment is shown in Fig. 3.

Functionally, the guns 1 ensure heating of the remelted briquettes (zone I) and melting of the briquettes in the cold hearth (zone II). The zone I is characterised by the gradual heating and degassing of the briquettes, followed by melting in zone II, resulting in an increase of the productivity of melting and a reduction of the losses due to splashing and evaporation.

The gun 2 is used for heating the metal in the cold asked (zone III) and periodic discharge of the melt from the cold hearth into the solidification mould by melting the skull layer in the zone IV. The gun 3 operates successively in the zones V-VII, ensuring heating of the metal and the solidification mould, formation of the high quality surface of the ingot and the cleaning of the spout of the cold hearth.

In the course of the experimental melts, MV-1 equipment was used to solve the problem of super heating the metal in the zones I and II. Thus melting of the initial charge with the guns 1 was carried out in the zone

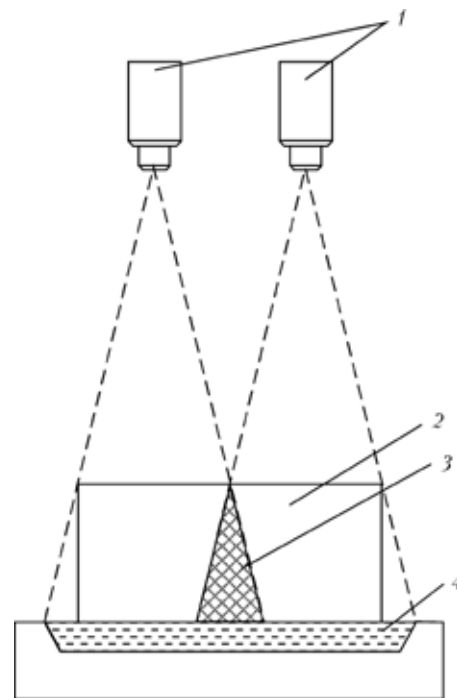


Fig. 4. Overlapping of the zones of the effect of the electron beams: 1) the electron beam guns; 2) the billets (0.8 m wide); 3) the combined heating zone; 4) the cold hearth.

of combined heating, situated at the end of the billets (Fig. 4). This zone is characterised by superheating of the metal and also by more intensive melting and evaporation.

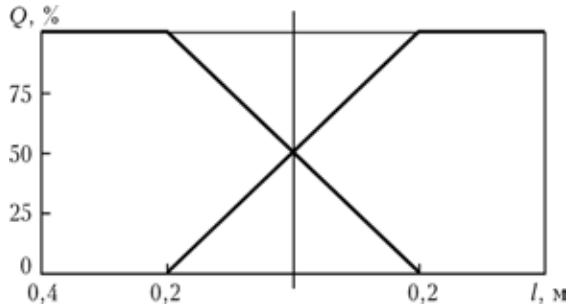


Fig. 5. Variation of power Q of electron beam guns in relation to distance l from the axis of the billet.

To remove superheating, it is necessary to program the ??? of the electron beams in accordance with a specific law. The removal of combined superheating takes place as a result of the redistribution of the power of the electron beam from 100 to 0% during the passage of the combined heating zone (Fig. 5).

To ensure mutual compensation of the beams 1 and 2 of the electron beam and gas, investigations were carried out into the two variants of the distribution of the power (Fig. 6): the variation of the number of passes of each ??? and the variation of the number of points (holding time of the beam) in each segment. Both variants were used and they provided positive results, i.e., uniform heating of the cross-section of the cold hearth in the zone of the effect of the first and second beams. Further investigations are necessary to determine which variant is preferred.

As a result of controlling the electron beam guns of MV-1 equipment in the system for zone heating of metal in melting of molybdenum it was possible to produce ingots with a diameter of up to 130 mm, characterised by the highest quality surface without any significant corrugation or cracks.

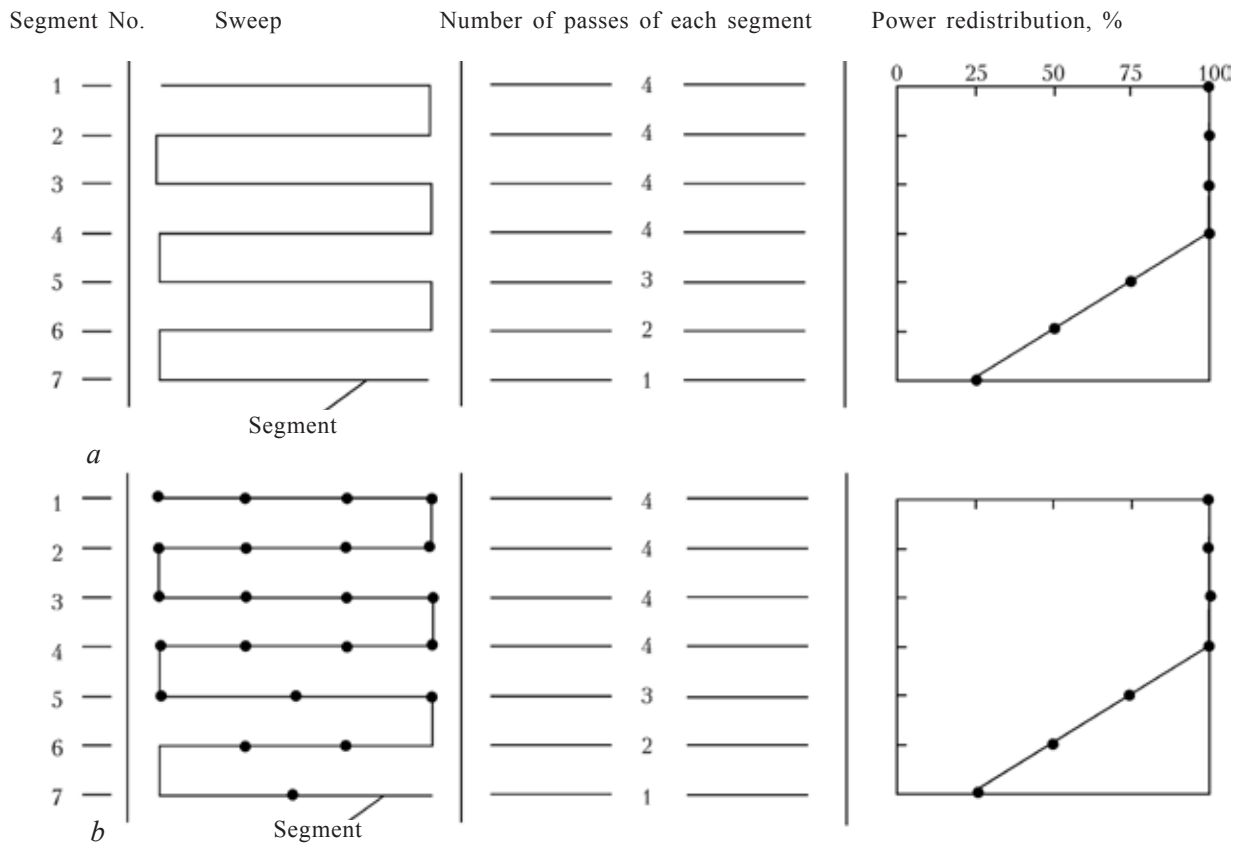


Fig. 6. Redistribution of beam power in beam sweep by varying the number of passes of the segment (a) and points (b) in segment.

The chemical purity of the investigated ingot with respect to the given elements corresponds to the requirement for the molecule and grades MCh (pure molybdenum, 99.96 wt.%) used for important applications [6]. The content of the impurities decreased by more than a factor of 3, and the gas content 10-100 times.

Conclusions

(1) Equipment and the procedure were developed for the efficient control of electron beam heating in the melting of refractory metals in the cold hearth.

2. The problem of the nonuniform heating of the metal is a result of warbler in of the beams has been solved.

3. The experimental results show that the system is used efficiently in the melting of molybdenum ingots in MV-1 electron beam equipment and can be used to produce high-quality ingots with the required chemical

composition.

4. The system will be used in future in more powerful multi-gun melting systems and combined systems for vacuum melting and evaporation.

References

1. Zaboronok G.F., et al., Electron beam melting of metals, Metallurgiya, Moscow, 1965.
2. Movchan B.A., et al., Electron beam melting and refining of metals and alloys, Naukova Dumka, Kiev, 1972.
3. Paton B.E., et al., Electron beam melting, Naukova Dumka, Kiev 1997.
4. Zelikman A.N. and Korshunov B.T., The metallurgy of rare metals, Metallurgiya, Moscow, 1991.
5. Paton B.E., et al., Electron beam melting of titanium, Naukova Dumka, Kiev, 2006.
6. Mushegyan V.O., *Sovremenn. Elektrometall.*, 2009, No. 4, 26–28.
7. Udris Ya.Ya. and Chernov V.A., Powerful electron beam guns with the high-voltage glow discharge, in: Proceedings of the Second International conference on the electron beam technologies, Varna, Bulgaria, 1988, 254.



Plasma metallurgy and service life of plasma torches

V. A. Shapovalov, K. A. Tsykulenko, I. V. Sheiko and V. I. Kolesnichenko

E.O. Paton Electric Welding Institute, Kiev

The article describes the application of plasmotrons (plasma torches) in metallurgy for melting of metals and alloys, the effect of different factors on the service life of the plasmatron and measures taken for its improvement are shown.

The rapid development of plasma metallurgy started in the 60s of the previous century [1, 2] and at the present time it is used in the industry of many developed countries. Plasma heating is used in many stages of metallurgical production, including the processes of extraction of metals from ores, melting and processing of metals and alloys in plasma reactors and furnaces, and also for the intensification of the methods of melting and processing of materials.

The melting of the steels and alloys, and also remelting of billets is aimed at increasing the quality of metal are carried out in plasma-arc furnaces. The principal diagrams of these furnaces are shown in Fig. 1.

The specific feature and obvious advantage of plasma heating is the possibility of treating the metallic melts with different gas mixtures of the appropriate composition at a given pressure. The results of a large number of investigations of interaction of gas with metals in the conditions of plasma-arc melting and remelting, and also the technological features of this processes have been generalised in a number of monographs [2–5].

The inert atmosphere and the absence of traditional contamination sources of metal typical of electric arc melting (for example, graphite electrodes) result in the formation of a metal from the conversion charge with the high content of waste, in particular, stainless steels with a superlow mass fraction of carbon. When using argon–nitrogen gas mixtures as plasma forming mixtures, the metal is alloyed with nitrogen without application of nitrided ferroalloys.

Plasma arc melting (PAR) at high or normal pressure results in the conservation in the alloys of alloying elements with high vapour tension (chromium, manganese, etc), saturation of the alloy with nitrogen, and at reduced pressure – more extensive degassing of the metal (for example, titanium).

PAR is used for improving the quality of special alloyed steels, precision and creep-resisting alloys, refractory metals, for producing austenitic steels with a higher nitrogen content which can be obtained in and the melting methods, and for reducing the losses of volatile and easily oxidised elements. The application of plasma-arc heating in interac-

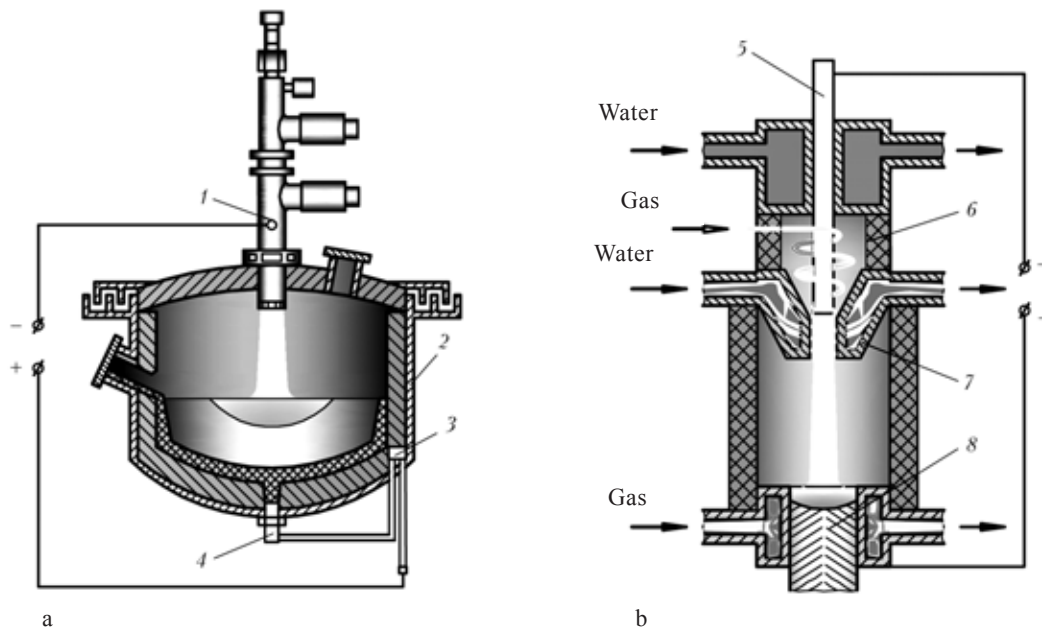


Figure 1. Plasma-arc furnaces for melting steels and alloys (a) and remelting billets (b): 1) the plasma torch; 2) the furnace chamber; 3) the solenoid for mixing of liquid metal; 4) the hearth electrode–anode; 5) the electrode for remelting; 6) the chamber; 7) the nozzle of the plasma torch; 8) the solidification mould.

tion melting reduces the melting time of the charge and increases the intensity of the process of refining of the metal.

One of the main problems of plasma metallurgy is the formation of low-temperature plasma. According to the operating principle, the arc plasma torches used most frequently in plasma metallurgy are divided into two types: with the independent (jet) and dependent (direct action) arc.

In jet plasma torches (indirect action), the electric arc burns between the electrode and the nozzle, i.e., between the two electrodes, installed in the plasma torch. A gas is blown through this arc and, consequently, the gas is partially ionised. Heating on melting of the treated material takes place as a result of the heat content of the plasma forming gas, discharged from the nozzle of the plasma torch in the form of a high-temperature jet.

In the direct action plasma torches, the electric arc forms between the electrode and the heated material. The material is heated mainly as a result of the direct effect of the arc discharge (the main amount of heat is generated in the near-electrode regions) and only 25% of the total amount of heat is

transferred by the plasma flow [6, 7].

Multi-atomic plasma gas is used for intensifying the processes of heating on melting the process material. The high-enthalpy plasma of gases such as hydrogen and nitrogen results in more extensive heat transfer not only to the processed material but also to the structural elements of the plasma torch in contact with the material (electrode, nozzle), and this reduces the service life of the plasma torch.

The increase of the service life of individual plasma torches and the furnace (reactor) is one of the main problems delaying the application of the plasma torches and development of plasma metallurgy. The increase of the volumes of the simultaneously processed materials and, consequently, the power of the plasma systems requires the development of reliable plasma torches with a long service life. If the service life of the cutters and torches is not important for the processes of plasma welding and cutting of metal because of the relatively short in duration of these processes (the replacement of the electrodes and nozzles at the end of the design life is a relatively fast and simple), in plasma metal-

lurgy in which the duration of the process may be several tens or even hundreds of hours the service life of the plasma torches is of controlling importance.

In some cases, to replace the structural elements of the plasma torch at the end of the design life it is necessary to arrest the process, disconnect from the supply systems, take the torch out of the equipment, dismantle the torch into individual parts. This reduces the efficiency and increases the idling time. In most cases, the increase of the power of the plasma torch reduces the service life, and the increase of the number of plasma torches in the plasma system results in the increase of the number of shutdowns for replacing the components at the end of the design life.

In plasma torches with the dependent arc, the variations of the service parameters of the plasma torch (rapid increase of current, the diameter of the column of the constricted arc, reduction of the flow rate of the variation of the nature of supply of the gas, cooling of the nozzle, etc) may result in an electrical breakdown between the electrode and the nozzle. The result of the breakdown, instead of the single arc, burning between the electrode and the processed material, there are two arcs (between the electrode and the nozzle, and also between the process material and the nozzle), leading to a rapid failure of the material.

As regards the electrode, the degree of wear is one of the most important parameters which determines in the final analysis, the service life of the plasma torch. The permissible wear of the electrode depends on the design of the plasma torch, and the erosion eight on the condition of the process. Specific erosion is used for characterising the rate of erosion of the electrode in the conditions of a specific process [8, 9].

In generation of a plasma arc discharge, to sustain the electrical current between the electrodes, charged particles should be supplied into the plasma. As a result of one of these circumstances it is possible to avoid failure of the surface of the electrode material.

The failure of the material of the electrode

under the effect of electrical discharge is regarded the same property of matter as other properties. Erosion of the electrodes of the plasma torch as a consequence of complicated thermal, electrical, chemical and other processes in the near-electrode region, on the surface and inside the electrode material. Various methods can be used to reduce the erosion but it is not possible to stop erosion completely.

Various methods of increasing the service life of the electrodes of the plasma torch and the plasma equipment as a whole will be discussed.

Taking into account the fact that the erosion of the electrode is of thermal nature, the most evident methods of improving the service life is to ensure the optimum (for the given electrode material) thermal state. The electrodes of the plasma torch are divided into hot (graphite, tungsten, tantalum, etc) and cold (copper, steel, aluminium). The values of the maximum thermal flows leading to intensive failure may greatly differ.

For example, the cold cathodes may operate on the other relatively low thermal flows (not greater than $1 \cdot 10^5$ kW/m²) and, therefore, efficient water cooling is essential when using these electrodes.

The hot electrodes must also be cooled but direct cooling of the electrodes may lead, as a result of high thermal stresses, to sudden failure and malfunction and, consequently, these electrodes are usually placed in special water-cooled attachments – holders, clamps, etc. The hot electrodes, in particular, electrodes made of tungsten, should be installed without extension at $l_k = 0$ [9] thus ensuring efficient heat removal and preventing the wear of the side surface of the electrodes.

In addition, the service life of the tungsten electrode (cathodes) can be extended by increasing the thermal emission properties. Alloying of tungsten with elements such as lanthanum (approximately 1 % La) and thorium (approximately 1 point % ThO₂) not only increases the thermal emission properties but also reduces the specific heat flow into the cathode.

However, it should be mentioned that for the optimum operation of the electrodes made of alloyed tungsten ensuring the appropriate diffusion rate and the uniform yield of the emission material, it is necessary to maintain the appropriate temperature not only on the working surface but also the entire electrode. Therefore, these electrodes are installed with some extension [10].

The operation of the tungsten electrode is strongly affected by the structure of the material and the presence and nature of impurities. The increase of the dispersion and homogeneity of both the inclusions and the material of the base of the electrode reduces the rate of the process of formation of dislocations. In some cases, the service life is increased using cathodes made of porous tungsten ($P = 20\%$). When argon is blown through the porous cathode, the cathode is cooled at a higher rate.

In addition to porous cathodes, there are also various thermal emission inserts made of powder material based on the oxides of the titanium subgroup with different additions. The specific erosion of these electrodes at current of up to 1000 A is approximately $1 \cdot 10^{-10}$ kg/C.

The erosion rate of the tungsten electrode (or of another thermal cathodes) depends greatly also on the diameter of the electrode. When the diameter of the tungsten electrode is increased (from 2 mm), the rate of specific corrosion initially rapidly decreases and then smoothly increases. The optimum diameter of the tungsten electrode at which the specific erosion is minimum is 4–5 mm for the electrodes working at the current of approximately 400 A, and 5–6 mm for the current of approximately 1000 A [9, 10].

In addition, the erosion rate of the electrode also depends on the nature of connection (diffusion or contracted) with the arc column. Arc constrictions results in the formation of the so-called anode and cathode spots with high current density.

The highest rate of corrosion is recorded usually in cathode spots. If the spots form on the cold cathodes, the electrode metal

droplets may be rejected during boiling.

Spots form on the hot cathodes if the pressure of the working gas is lower than $1.33 \cdot 10^4$ Pa. At higher pressures, the thermal autoemission arc discharge with the spots moving randomly on the cathode changes to the thermal emission arc discharge without the cathode spot.

Thus, the constricted connection increases the degree of erosion. However, in the case of diffusion connection with a longer extension of the tungsten cathode ($l_k > 0$) erosion may be higher than in the case of the contracted connection with $l_k = 0$ [9].

One of the methods of increasing the service life of the electrodes is to move the arc spots on the surface. On the one side, this makes it possible to reduce the specific heat flow into the electrode and, consequently, reduce the erosion rate and, on the other side, even in the same rate of loss of the material by the electrode in the case of the large increase of the area from which the material is removed to the total service life of the electrode increases. The displacement of the arc spot on the electrode surface may be realised using different gas-dynamic and electromagnetic methods of twisting the arc or combination of these methods. The surface of the electrode is characterised by the formation of a narrow erosion groove (trace), corresponding to the trajectory of movement of the reference arc spot. To increase the area of the working surface of the electrodes and, consequently, the service life, the arc spots are moved not only around but also along the electrode axis (hollow electrodes). The spots carry out translational movement in the longitudinal direction which is referred to as scanning.

By changing the ratio of the frequency of rotation of the spot of connection of the arc and the scanning frequencies is possible to obtain various types of the trajectory of the arc spot on the internal surface of the hollow electrode (Fig. 2).

As regards the service life, not only the area of scanning but also the uniform processing of the surface is important.

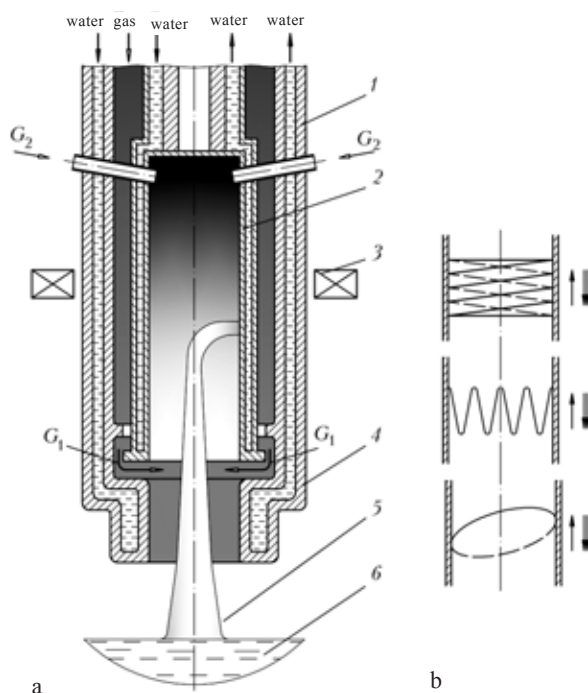


Fig. 2. The plasma torch with a hollow electrode and displacement of the arc spot on the surface of the electrode (a), and also the types of trajectory of the arc spot on the internal surface of the hollow electrode (b): 1) the body; 2) the hollow electrode; 3) the electromagnetic coil; 4) the nozzle; 5) the arc; 6) the melt; G_1 , G_2) the consumption of gases.

To ensure uniform wear of the working surface, it is recommended to use various measures (continuous or discrete scanning, special methods of connecting magnetic lenses, maintenance of the required angle of phase shift between the two lenses, etc).

The scanning area is determined by the internal diameter of the electrode and the length of the scanning section. For each internal diameter of the whole electrode there is a critical current resulting in the jump-like increase of the erosion rate (the level of critical current increases with increasing diameter).

The service life of the electrodes of the plasma torch is strongly affected by the composition of the surrounding atmosphere, especially the presence of oxygen and hydrogen. For example, at an oxygen concentration of the plasma forming gas (nitrogen) of molten 0.7%, the specific erosion of tungsten rapidly increases and reaches $(2...4) \cdot 10^{-8}$ kg/C.

An increase of the pressure of the plasma

forming gas increases the level of the specific erosion of the electrodes. The service life of the electrode in a specific medium can be increased only by the efficient selection of the electrode material, the dimensions of the electrode and by ensuring the optimum cooling conditions.

The strongest effect is exerted on the electrode erosion by the current passing through the electrodes. Therefore, various measures are taken to reduce the current load on the electrode (splitting of the arc column, work at high voltages and reduced current or application of different multi-electrode systems).

The splitting of the arc or of part of the arc into several current-conducting channels can be carried out both on the cathode and anode radial sections by creating, on the internal surface of the electrode, local areas of preferential arc connection, for example, by placing thermal emission inserts into the body of the copper tubular electrodes. In this case, it is possible to reduce the local thermal load on the electrode, reduce the degree of erosion of the electrode material and, consequently, increase the service life.

There are also electrodes with a solid copper tip in which a large number of thermal cathode inserts (assembled cathodes) is installed. In this case, the process of displacement of the arc is spontaneous and, consequently, erosion of the insert is nonuniform. During operation of the electrode the arc either jumps from one insert to another or is split into several channels.

The application of high voltage in the plasma torches makes it possible to work (at the same power) at relatively low values of arc current and ensure longer service life of the electrode. However, the application of high voltage increases the dimensions of the plasma torches, complicates service of the torches and results in unpredictable failure of operation as a result of breakdown on the insulating inserts.

The application of multi-electrode systems, in contrast to the splitting of the already existing arc column, is based on the formation of initially several separate arcs with

subsequent transformation into a single arc with high power. The method of splitting of the arc is used in the indirect action plasma torches, and the multielectrode circuits are used in the direct action plasma torches. Taking into account the fact that the service life of the cathode and the anode differs (in some cases it differs by an order of magnitude), to increase the total service life of the plasma torch it is necessary to change the polarity of the electrodes, i.e., operation with alternating current. In fact, in addition to the direct current plasma torches, the multielectrode alternating current plasma torches, characterised by higher unit power in comparison with the DC plasma torches are used on an increasing scale.

Recently, special attention has been paid by the investigators and developers to the formation of the common arc column by 'contraction' of the single low-power local arc of the multielectrode plasma torch (Fig. 3) [11]. For this purpose, it is necessary to avoid shunting and 'throwing' of the individual local arcs to the adjacent electrodes.

The required increase of the power of the

plasma melting systems may be achieved by using several simultaneously working plasma torches. Such a furnace may be powered by the three-phase system and ensure uniform loading of the electrical circuit, and each individual plasma torch can work with the single-phase circuit.

The presence of several plasma torches enables processing of a large volume of the material at a relatively low power of the plasma torch. It should be mentioned that the increase of the power of the plasma furnaces result of increasing the number of the store plasma torches cannot continue to any high values.

An increase of the number of the plasma torch is greatly complicates the design of the system and servicing and increases the duration of breakdown. Therefore, these systems become economy cleaner efficient and the increase of the unit power of the plasma torch remains to be an urgent task.

Another method of reducing the load on the electrodes of the plasma torch is the application of circuits operating on the basis of the Cascade amplification principle. A suitable example of this amplification is the method based on the force generation of charged particles in the near-electrode region of the arc [12].

In the first stage, the pro-current plasma torch (plasma electrodes) produces some number of the charged particles for operation of the main electrode, and the second stage, the number of charged particles is increased as a result of the main electrode. The main electrode works in the conditions of the relatively low surface temperature and the working current of the plasma torches determined by the total number of electricity carriers. The service life of the plasma torch at a current of 10 kA made reach 200 h.

The total service life of the arc plasma torch may also be increased by other methods – not by increasing the service life of the single electrode, but by periodic replacement of the electrode immediately during operation in the course of wear. In most cases, these changes take place using a multiposition cath-

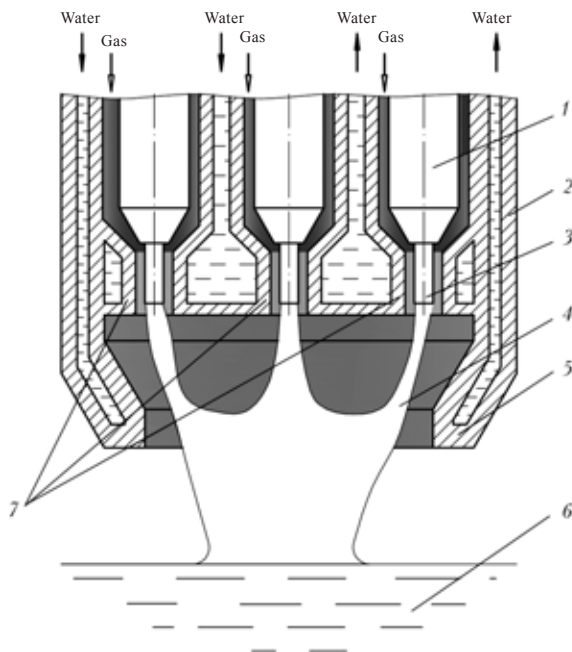


Fig. 3. The diagram of a multielectrode metallurgical plasma torch: 1) the electrode holder; 2) the body; 3) the electrode; 4) the arc; 5) the common nozzle; 6) the melt; 7) the stabilising nozzles.

ode section. The number of electrode-inserts and the distance between them at the uniform distribution around the circumference of the cathode section are selected in accordance with the required duration of the continuous operation of the plasma torch.

In the technological processes in which the erosion of the electrode material has no effect on the quality of the product, both the consumable electrode in plasma torches can be used. For example, the consumable plasma torch is used in plasma arc melting of large steel ingots. Here, the consumable plasma torch is a hollow steel billet after remelting [6, 13, 14].

There are circuits of plasma reactors with liquid metal electrodes [10]. The application of liquid metal as the electrodes and the special features of the design indicate the almost unlimited service life of the electrodes, high current and efficiency of the arc. However, regardless of all the advantages of the design of these plasma torches—the reactors and processing technology, for example, different waste, these methods are relatively expensive and complicated. Therefore, they should be used for processing ‘dangerous’ waste, eliminating chemical weapons or for other purposes.

Conclusions

1. It has been shown that, taking into account the special features of the plasma-arc processes of melting and remelting (treatment of the metallic melts with different gas mixtures of the appropriate composition and at different pressure, and also the effect on the surface life of the plasma torch of almost any change in the design or technological conditions), the arc plasma torches with a long service life can be used for only highly specialised applications.

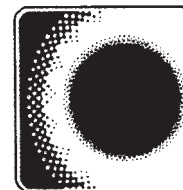
2. It is believed that the promising directions for the plasma-arc processes of melting and remelting are the development of the design of multielectrode plasma torches and of plasma torches with a plasma electrode; the design and technological conditions en-

suring diffusion connection to the internal surface of the hollow electrode, and also the technology and melting systems based on the remelting of consumable electrodes and the plasma torches.

3. It has been established that in the design of multielectrode plasma torches it is necessary to ensure the reliable merger of the individual arc into a single common arc and prevent double arc formation and ‘jumping’ of the arc to the adjacent electrodes (especially when using the three-phase power system). It is important to determine the conditions of reducing several current-conducting plasma flows, the optimum mutual position of the electrodes and the permissible electrical regimes. The diffusion connection of the arc to the internal surface of the hollow electrode may be formed as a result of the appropriate configuration of the internal surface of the electrodes in the direction of gas flows. In the development of the signs with the consumable electrode it is important to consider the application of graphite electrodes and sliding contacts.

Conclusions

1. Paton B.E., et al., *Avt. Svarka*, 1966, No. 8, 1–5.
2. Farnasov G.A., et al., *Plasma melting*, Metallurgiya, Moscow, 1968.
3. Lakomskii V.I., *Plasma arc remelting*, Tekhnika, Kiev, 1974.
4. Erokhin A.A., *Plasma arc melting of metals and alloys*, Nauka, Moscow, 1975.
5. Klyuev M.M., *Plasma arc remelting*, Metallurgiya, Moscow, 1980.
6. Latash Yu.V. and Matyakh V.N., *Advanced methods of production of billets of very high quality*, Naukova Dumka, Kiev, 1987.
7. Dembovskii V., *Plasma metallurgy*, Metallurgiya, Moscow, 1981.
8. Zhukov M.F. (editor), *Experimental investigations of plasma torches*, Nauka, Novosibirsk, 1977.
9. Zhukov M.F., et al., *Electric arc generators of thermal plasma*, Nauka, Novosibirsk, 1989.
10. Cherednichenko V.S., et al., *Plasma electrical engineering equipment*, NGTY, Novosibirsk, 2008.
11. Shapovalov V.A., and Latash Yu.V., *Probl. Spets. Elektrometall.*, 1989, No. 4, 50–56.
12. Paton B.E., et al., Patent 2014412, UK, MPC H05B7.
13. Paton B.E., et al., *Metallurg*, 1974, No. 10, 9–12.
14. Paton B.E., et al., *Probl. Spets. Elektrometall.*, 1975, No. 2, 78–82.



Properties of Kh13-type steels alloyed with nitrogen

G. M. Grigorenko, Yu. M. Pomarin, V. V. Lakomskii, V. Yu. Orlovskii and
I. I. Alekseenko

E.O. Paton Electric Welding Institute, Kiev

The results of comparison of the structure and physical-chemical properties of standard steels of Kh13 type and those alloyed with nitrogen are considered. It is shown that alloying with nitrogen promotes the increase in the mechanical properties of steels.

The production and application of high-nitrogen steels is one of the priority directions of the development of special electrometallurgy throughout the world as a result of the unique properties of these materials. The attention of scientists and technologists has been attracted especially by austenitic steels rather than by ferritic–austenitic and ferritic–martensitic steels.

At the same time, the application of nitrogen as the alloying additions for steels of these types is highly promising [1–7]. For example, the addition of small amounts of nitrogen increases the yield strength whilst retaining the values of hardness, increases the level of corrosion resistance, reduces the heterogeneity of carbides, supports spheroidisation of the carbides, etc [4, 5].

The addition of nitrogen into steel with the chromium content 10–12% increases the heat resistance and, consequently, the steels of this type can be used for the manufacture of turbine rotors, working at temperatures up to 650°C, and also for inlet valves of high-powered engines [1, 2].

One of the promising directions of increas-

ing the service characteristics of the materials of this type is the partial or complete the replacement of carbon with nitrogen which reduces the carbide heterogeneity and results in homogenising and improvement of the structure of the metal.

The aim of the present work is the calculation of the effect of nitrogen on the structure and mechanical properties of the type Kh13 steels. For this purpose, simulation alloys Kh13 and 20Kh13, alloyed with nitrogen from the gas phase (Table 1), where melted in experimental equipment [8]. These alloys were selected in order to compare the properties with the properties of the standard steel 20Kh13.

It should be mentioned that the distribution of nitrogen in the cross-section and height of the billets was uniform.

Table 1. The results of chemical and spectral analysis of the billets

Steel	Mass fraction of alloying elements, %		
	C	Cr	N
Kh13A	0	12.37	0.244
20Kh13A	0.14	12.78	0.240

The billets were pressed in a press to a size of 400 mm and rolled in an experimental single-stand mill to a thickness of 15 mm.

The nonmetallic inclusions were determined in OMNIMet 80-1000 equipment in accordance with GOST 1778-91 standard. The method is based on counting the area of nonmetallic inclusions situated in the unit area of the section followed by classification in size groups. The accuracy of the method depends on the efficiency of polishing the section (without etching).

The results of analysis of the content of nonmetallic inclusions in the molten steels are presented in Fig. 1.

The largest number of the nonmetallic inclusions is found in the steel 20 Kh13A, 1.024 vol. %, and the Kh13A and 20Kh13 steels contain 0.205 and 0.218 vol.%, which is within the range allowed by the standards. The content of the nonmetallic inclusions with the size of 0.15–1.5 μm was the largest in the steels. Evidently, these very small particles should not have any strong effect on the mechanical properties of steels because they are spherical and cannot act as stress concentrators.

The temperature conditions of heat treatment were selected taking into account the requirements of the GOST 5949-75 and GOST 7350-77 standards for the steels of this great. Quenching was carried out in oil at tempera-

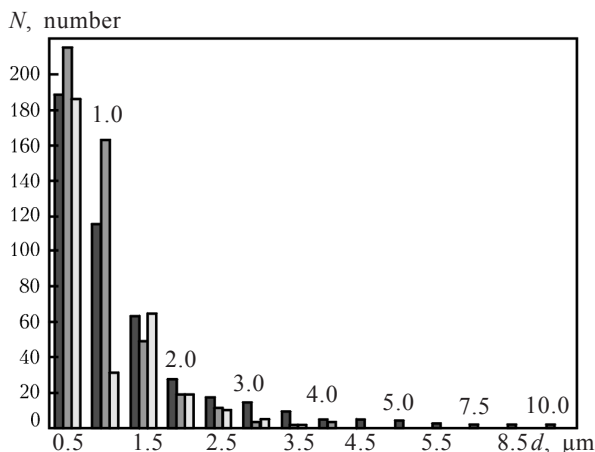


Fig. 1. Distribution of the nonmetallic inclusions in the volume of a billet in steels Kh30A, 20Kh30A and 20Kh13, N , d are the number and size of the nonmetallic inclusions, respectively.

tures of 1050–1100°C, and high-temperature (500°C) and low-temperature (200–300°C) tempering was also carried out.

Quenching and tempering were carried out together with the reference specimens taken from the same material as the specimens for the mechanical tests with the size of $50 \times 12 \times 15$ mm.

The specimens for the mechanical tests were sent for grinding and the reference specimens were clamped in mechanical holders and sent for further metallographic examination.

Figure 2a shows the microstructure, penetrated by the martensite needles. Low carbon was found in Kh13A steel. In the literature, these grains are referred to as pseudo-martensite. The randomly distributed inclusion of the spherical and irregular shape (Cr_2N) were also found.

Figure 2b shows the microstructure of 20Kh13A steel. The structure is martensitic. The grain boundaries of the steel contain spherical inclusions of Cr_{23}C_6 . There are sometimes dark inclusions of irregular shape, possibly Cr_2N . The structure of the 20Kh13 steel (Fig. 2c) is also martensitic, with misoriented grains. Inclusions of the circular shape Cr_{23}C_6 are found along the rolling bands at the grain boundaries.

The microstructure of Kh30A steel after quenching (Fig. 3a) consists of plate-shaped and acicular martensite with the relatively thick needles. In some areas, there are precipitates of inclusions of the irregular shape Cr_2N .

In the microstructure shown in Fig. 2b, II, there are grains penetrated by the martensite needles. In some areas there are precipitates of the inclusions of irregular shape, Cr_2N . The distribution of the spherical inclusions Cr_{23}C_6 is uniform. Figure 2c, II shows the microstructure of 20Kh13 steel, consisting of high-dispersion martensite. There are also Cr_{23}C_6 inclusions distributed uniformly throughout the entire specimen.

The microstructure shown in Fig. 2a, III consists of plate-shaped bainite. The space between the bainite plates is occupied by Cr_2N inclusions.

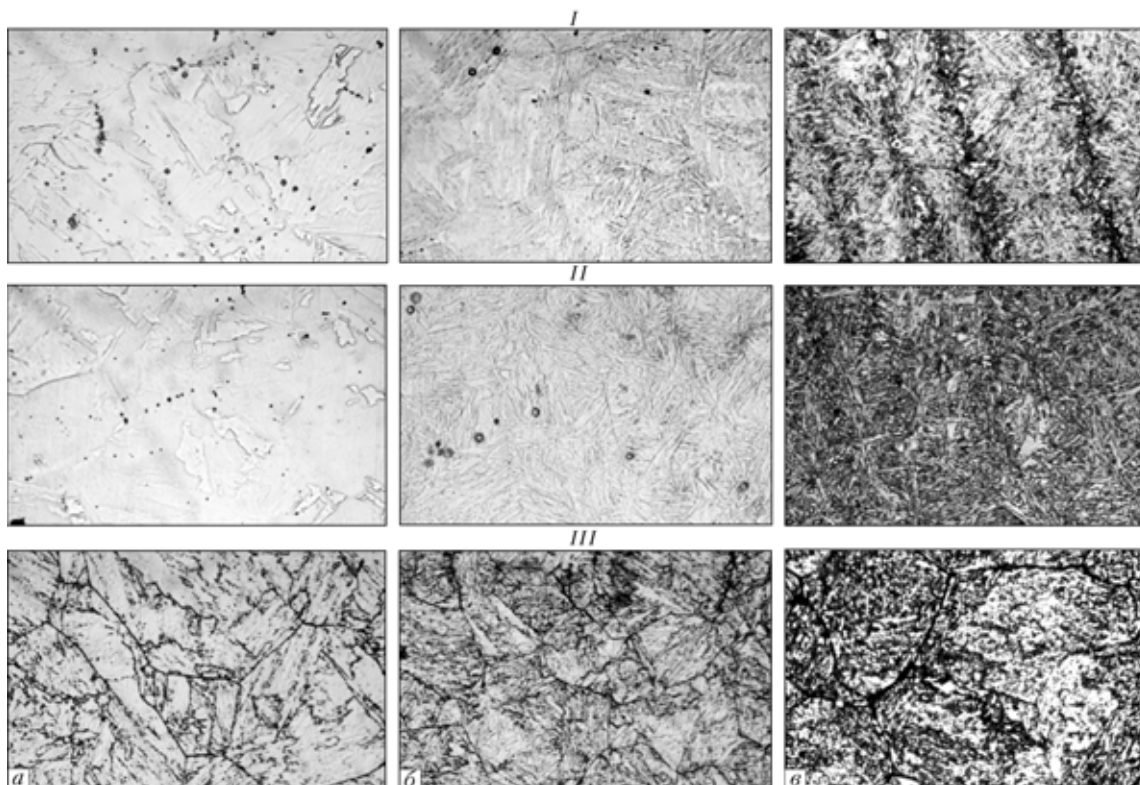


Fig. 2. Structure ($\times 500$) of the Kh13A (a), 20Kh13A (b), and 20Kh13 (c) after quenching from 1100°C and tempering at 200 (I), 300 (II) and 500°C (III).

The microstructure of 20Kh13A steel after tempering at 500°C (Fig. 2b, III) consists of large grains penetrated by fine-dispersion bainite and the needles of tempered martensite. The space between bainite and martensite is filled with the inclusions of the $Cr_{23}C_6$ type and a small amount of the Cr_2N inclusions.

The microstructure of 20Kh13 steel (Fig. 2c, III) contains grains of different sizes. High-dispersion bainite is found inside the grains. The inclusions of $Cr_{23}C_6$ are also found between the bainite plates.

As indicated by Fig. 3, the highest hardness of all the investigated steels was detected at a tempering temperature of 200°C. The hardness of all steels decreases as a result of tempering at 300 and 500°C. The Kh13A alloy has the highest hardness, the hardness of the 20Kh30A steel is lower, and 20Kh13 steel has the lowest hardness.

When the tempering temperature is reduced, the microstructure of the steels becomes more dispersed and this in turn increases the hardness, strength, etc. Tempering at 500°C is accompanied by the formation of a bainite-like structure. The hardness of this structure is lower than that of the martensitic structure.

Analysis of the results indicate that the pseudo-martensite of the nitrogen-alloyed steels has higher hardness than conventional martensite and, because of this, the nitrogen shows a tendency for ordering of the structure, whereas the carbon results in cluster formation.

The results show that nitrogen alloying greatly increases the strengths of the steels

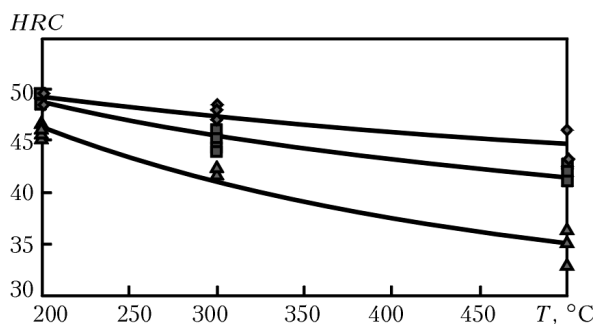


Fig. 3. The hardness of steels Kh13 (◆), 20 Kh13A (■◆) and 20Kh13 (▲) after tempering at different temperatures.

Table 2. The mechanical properties of the alloys Kh13A, 20Kh13A and 20 Kh13 after different heat treatments

Steel	Ingot No.	T_s , °C	σ_T , MPa	σ_B , MPa	δ , %
Kh13A	1	500	1139.3	1298.6	13.2
	2	500	1185.7	1351.3	12.7
	1	300	-	284.8	-
	2	300	-	385.5	-
	1	200	-	1250.3	-
	2	200	-	1060.1	-
20Kh13A	1	500	-	953.8	-
	2	500	-	717.2	-
	1	300	-	529.9	-
	2	300	-	920.0	-
	1	200	-	907.5	-
	2	200	-	1186.7	-
20Kh13	1	500	-	1364.1	-
	2	500	-	1523.5	-
	1	300	1480.6	1829.3	17.3
	2	300	1520.0	1816.2	26.7
	1	200	-	253.3	-
	2	200	-	239.9	-

Comment. Quenching temperature T_q was 1100°C in all cases, T_t is tempering temperature.

(Table 2). To compare the mechanical properties, the values for the standard 40Kh13 steel are also presented. The results of comparison are shown in Table 3.

The daytime Table 3 shows that the steels were subjected to the sign he treatment (conditions) and the mechanical characteristics of the steels are similar. However, all these data can only be treated as preliminary, and additional investigations are required for obtaining more accurate and reliable data.

Conclusions

1. The experimental results show that the microstructure of the nitrogen-alloyed steels dissimilar to that of the carbon steels of the same grade, but the martensite in nitrogen-alloyed steels is replaced by pseudo-martensite or nitrogen martensite, and the microhardness of this martensite is similar to that of carbon

Table 3. Comparison of the mechanical properties of the industrial steel 40Kh13 and Kh13A

Steel	Heat treatment conditions, °C	σ_B , MPa	$\sigma_{0.2}$, MPa	HRC
40Kh13	$T_s = 1050$ $T_t = 500$	1165	960	34.0
Kh13A	$T_s = 1100, T_t = 500$	1352	1160	44.5

or classic martensite. At the same time, the matrix of the steels with the higher nitrogen content is considerably softer and more elastic in comparison with that of the classic composition.

2. It was found that the hardness of the quenched specimens and mechanical properties of the Kh30A and 20Kh13A steels is similar to the mechanical properties of the 40Kh13 steel and equals approximately 50 HRC. This indicates that alloying with 0.2% nitrogen replaces alloying with 0.4% carbon. The highest mechanical properties were detected in the steels tempered at 500°C, and the mechanical properties in this case are higher than those of 40Kh13 steel.

3. On the basis of the experimental results it is recommended to alloy the steels with higher carbon content with nitrogen instead of 40Kh13 steel because the mechanical properties of the former steels are similar or slightly higher than those of the conventional steels.

References

1. Gavriljuk V.G. and Berns H., High-nitrogen steels, Springer-Verlag, Berlin, Heidelberg, 1959.
2. Stein G. and Diehl V., High-nitrogen alloyed steels on the move – field of applications, International conference High nitrogen steels, HNS-2004, Ostend, Belgium, 2004, 46–52.
3. Klotz U.E., et al., Materials Science Forum, 1999, vol. 316–320, 437–442.
4. Babaskin Yu.Z., et al., Economically efficient alloying of steel, Naukova Dumka, Kiev, 1987.
5. Babaskin Yu.Z., et al., Lit. Proiz., 2003, No. 1, 36–48.
6. Kostina M.V., et al., Tekh. Metallov, 2000, No. 10, 2–12.
7. Kostina M.V., et al., Materialovedenie, 2001, No. 1, 35–44.
8. Pomarin Yu.M., et al., Probl. Spets. Elektrometall., 1996, No. 2, 46–50.



Development and application of the innovation technology of melting ShKh15SG-V ball bearing electric steel

A. I. Panchenko, A. S. Salnikov and M. I. Gasik

Dneprospetsstal', Zaporozh'e, National Metallurgical Academy, Dnepropetrovsk

The results of development, industrial mastering and implementation in production of innovation technology of melting bearing steel ShKh15SG-V in arc furnaces DSP-60, refining in the furnace–ladle unit and vacuum treatment with diversification of deoxidizers and alloying elements are analyzed and generalized. The increase in the output of efficient batches of section rolled steel ShKh15SG-V of all five dimensional groups after the first acceptance control as to the non-metallic inclusions and control by ASTM E-45 (method A) from 63 % (according to existing technology) up to 90 % (according to developed technology), and by separate dimensional groups of rolled metal – 100% was achieved.

Importance of increasing the quality of ShKh15SG-V ball bearing steel by reducing the degree of contamination with nonmetallic inclusions

The ball bearing steel, produced at the Dneprospetsstal' a company is supplied in large quantities to the Khar'kov Ball bearing Plant (AO KhARP) which is now occupying one of the leading positions in the domestic and international market for ballbearings, including for Russian Railways Company. A strong stimulus for the development of the production of the ballbearings at the AO KhArp from the electric steel supplied by Dneprospetsstal' is the supply by the company of ballbearings of different dimensional groups for the developing automobile industry

in Russia.

It is important to increase the efficiency of production of the ShKh15SG-V steel by increasing the evils of suitable batches of rolled stock from the first delivery inspection with respect to the nonmetallic inclusions in accordance with the estimate of GOST 801-78 and ASTM E-45 (method A), and also to reduce the specific consumption of deoxidation and alloying agents in melting of the steel.

Main assumptions of the currently available and new technology of melting and treatment of ShKh15SG-V steel outside the furnace

The technology used in 2007 for the melting of ShKh15SG-V ball bearing steel in the

DSP-60 arc furnaces was based on deoxidation and alloying of the metal product in the arc furnace and in the furnace ladle by ferrosilicium FS65 (DSTU 4127-2002) and also high-carbon ferromanganese FMn78A (DSTU 3547-97) [1]. In the discharge of the metal product from the failures into the ladle-furnace it was necessary to add solid slag materials (SSM), consisting of limestone and fluorspar. The metal in the ladle-furnace was deoxidised with aluminium. The ShKh15SG-V steel was poured into ingot moulds producing ingots weighing 3.4 t.

The physical-chemical audit of the processes, carried out in all stages of melting the metal product in the arc electric furnaces, treatment of the steel in the furnace-ladle unit and in the vacuum system, pouring of the metal and the formation of nonmetallic inclusions in solidification of steel in the ingot moulds, shows that the type and number of the inclusions are determined by the calcium and aluminium content of the steel and the

prior history of preliminary deoxidation and alloying of the metal product using specific types of ferroalloys with different content of calcium and aluminium.

When the solidification temperature of the steel with different residual concentrations of calcium and aluminium is used, calcium aluminates may form with different molecular composition and melting point (Fig. 1):

Calcium aluminates $\text{CaO}\cdot 6\text{Al}_2\text{O}_3$, $\text{CaO}\cdot 2\text{Al}_2\text{O}_3$, $\text{CaO}\cdot \text{Al}_2\text{O}_3$, $3\text{CaO}\cdot \text{Al}_2\text{O}_3$

Mass fraction of CaO, % 16.5 26.5 37.1 58.1

Melting point, °C 1852 1762 1604 1540

All the CaO compounds with Al_2O_3 formed by the peritectic reactions. The system also contains the eutectic with the chemical composition (wt.%): 49.1% CaO and 50.9 Al_2O_3 with the temperature of 371°C. It should be stressed that the references in the journal publications regarding the existence of the $7\text{CaO}\cdot 12\text{Al}_2\text{O}_3$ ($\text{Ca}_{12}\text{Al}_{14}\text{O}_{33}$) compound in the $\text{CaO}\text{--}\text{Al}_2\text{O}_3$ have not been substantiated. In [1], investigations were carried out into the $\text{CaO}\text{--}\text{Al}_2\text{O}_3$ and $\text{CaO}\text{--}\text{Al}_2\text{O}_3\text{--}\text{SiO}_2$ system and it has been confirmed that the $7\text{CaO}\cdot 12\text{Al}_2\text{O}_3$ compound, detected in a number of investigations, is the $\text{Ca}_{12}\text{Al}_{14}\text{O}_{32}(\text{OH})$ hydrate phase. The most complete and convincing investigations of the composition of the phases and ion-variants transformations in the $\text{CaO}\text{--}\text{Al}_2\text{O}_3$ system were described in [2] (Fig. 1).

At a constant calcium content of the steel, for example 10 ppm, depending on the concentration (activity) of aluminium calcium aluminates with different mineral composition can form in the steel and, consequently, with different numbers of the nonmetallic inclusions. In the case of a constant aluminium content and variation of the residual calcium concentration, suitable conditions may be created for the formation of calcium aluminates.

The sources of calcium in the melting of ShKh15SG-V ball bearing steel are ferrosilicium of FS65 grade (DSTU 4127-2002) and high-basicity slag in the ladle-furnace. Physical-chemical analysis of the processes of industrial melting confirms that the application of FS65 ferrosilicium with the uncontrolled

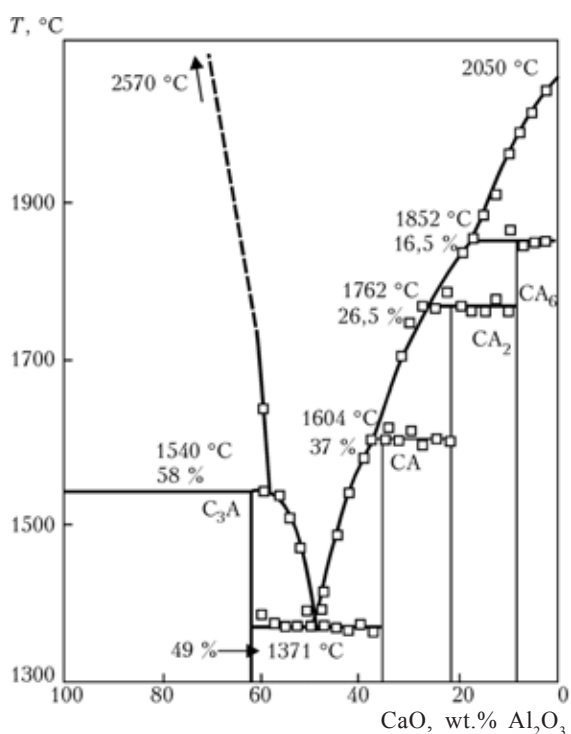


Fig. 1. Equilibrium diagram of the $\text{CaO}\text{--}\text{Al}_2\text{O}_3$ system, the numbers are the coordinates of the eutectic and peritectic transformations of the chemical compounds $3\text{CaO}\cdot \text{Al}_2\text{O}_3$ (C_3A); $\text{CaO}\cdot \text{Al}_2\text{O}_3$ (CA); $\text{CaO}\cdot \text{Al}_2\text{O}_3$ (CA_2), $\text{CaO}\cdot 6\text{Al}_2\text{O}_3$ (CA_6) [2].

standard of the calcium content (0.3–0.6%) is one of the main uncontrolled factors influencing the formation of a globular and oxide inclusions in ShKh15SG-V electric steel [3, 4]. At the same time, the application of 75% ferrosilicium with almost no impurities of calcium and aluminium, as established in the investigations carried out by the authors, did not solve the problem of increasing the load of suitable batches of rolled material from the first delivery inspection regarding the nonmetallic inclusions.

In a number of industrial melts of ShKh15SG-V steel using imported 75% ferrosilicium (the content of calcium and aluminium was not higher than 0.12% each) the size of the globular inclusions was reduced but this was accompanied by an increase of the extent of contamination of the steel with the nonmetallic inclusions and, consequently, there was no increase in the yield of the suitable batches of rolled material at the first delivery inspection [4].

Taking into account this important factor, to ensure the stable high yield of suitable batches of rolled material at the first delivery inspection with respect to the nonmetallic inclusions in evaluation in accordance with GOST 801-78 and ASTM E-45 standards (method A) a technology was developed for melting the ShKh15SG-V steel using the ferrosilicomanganese of the grade MnS25 and MnS17 DSTU 3548-97).

The calcium and aluminium content of ferrosilicomanganese, although it is not controlled by the standard, but taking into account the technology of production in the ferroalloys furnaces is always stable at a low value (no more than 0.10–0.15% each).

In the new technology of melting ShKh15SG-V steel the preliminary deoxidation of the metal product and alloying with chromium and manganese is carried out in an arc furnace using high-carbon ferrochrome and ferrosilicomanganese, and the chemical composition of the metal with respect to silicon was corrected with ferrosilicium in the ladle-furnace.

Thus, the new technology of melting

ShKh15SG-V electric steel uses the concept of ensuring in all stages of technology of melting and treatment outside the furnace of the steel of the justified and experimentally confirmed amount of calcium and aluminium in the steel in a specific concentration range. This is achieved by using ferrosilicomanganese, by developing the conditions of introduction of these substance into the metal product, deoxidation of the steel with aluminium and adherence to the vacuum treatment parameters [5].

Comparative analysis of the data on the quality of rolled sections with respect to the content of the nonmetallic inclusions in ShKh15SG-V steel, melted by the existing and new technology with the valuation in accordance with GOST 801-78

The ShKh15SG-V electric steel was melted in 2007 by the existing technology, and in 2008 and 2009 by the new technology. The data on the number of inspected batches and specimens of the metal. With respect to 5 dimensions groups and the number of rejects of specimens on the basis of the content of oxides, sulphides and globular inclusions in ShKh15SG-V steel are generalised in Table 1.

The data in Table 1 shows that the 'old' technology of melting the steel in DSP-60 furnace and refining in the furnace–ladle unit followed by vacuum treatment did not result in any high yield of the suitable batches from the first delivery inspection which equalled 62% with respect to 5 size groups, and only 48% with respect to the first size group.

In 2008 and 2009, the ShKh15SG-V steel was melted by the new technology with improvement of operations in every stage of melting: the addition of ferrosilicomanganese to the arc furnace or ladle–furnace, correction of the silicon content of the metal by ferrosilicium and deoxidation of the metal with aluminium, vacuum treatment of the steel.

The yield of suitable batches of rolled stock of ShKh15SG-V electric steel in 2008 increase to 80% and in 2009 to 90%. The number of rejects in all five size groups of

Table 1. The yield of suitable batches of rolled stock of five size groups of rolled material from the first delivery inspection of ShKh15SG-V steel melted by the existing and new technology in evaluation by GOST 801-78

Size group of rolled stock	Number, No.		Oxides			Sulphides			Globules			Yield of suitable batches at first inspection	
	Batches	Samples	Mean size	Rejects		Mean size	Rejects		Mean size	Rejects			
				No.	%		No.	%		No.	%		
2007													
1	391	3652	2	237	6.5	2	4	0.1	2	569	15.6	187	48
2	136	1337	2	10	0.7	2	0	0	2	95	7.1	107	79
3	141	1110	2	89	8.0	2	5	0.5	2	119	10.7	84	60
4	51	388	2	8	2.1	2	0	0	2	17	4.4	46	90
5	480	5142	3	158	3.1	3	84	1.6	3	331	6.4	332	69
Σ	1199	11629	—	502	4.3	—	93	0.8	—	1131	9.7	756	63
2008													
1	356	3075	1.9	169	5.5	1.6	1	0	1.9	270	8.8	227	64
2	91	770	1.8	4	0.5	1.6	0	0	1.9	14	1.8	84	92
3	128	904	2.2	50	5.5	2.0	0	0	2.1	32	3.5	98	77
4	69	551	2.3	6	1.1	2.1	0	0	2.3	6	1.1	65	94
5	413	4108	2.5	61	290	1.5	3.1	2.2	0	0	0	376	80
Σ	1057	9408	—	129	1.5	—	1	0	—	372	1.2	850	91
2009													
1	137	1246	1.8	21	1.7	1.7	0	0	1.7	28	2.2	114	83
2	1	6	1.5	0	0	1.5	0	0	1.5	0	0	1	100
3	20	174	2.1	3	1.7	2.1	0	0	1.9	5	2.9	16	80
4	6	43	2.2	0	0	2.1	0	0	1.9	0	0	6	100
5	285	2877	2.6	29	1.0	2.3	1	0	2.2	13	0.5	269	94
Σ	449	4146	—	53	1.28	—	1	0	—	46	1.11	406	90

the inspected specimens of the ShKh15SG-V steel with respect to oxidising 2008 and 2009 was 3.10 and 1.28 in comparison with 4.3% in 2007. The number of rejects of the specimens with respect to the globular inclusions in 2007 was 9.7% and rapidly decrease in 2008 (3.7%) and 2009 (1.11%).

Thus, the application of the new technology of production of ShKh15SG-V electric steel in the evaluation of the degree of contamination of the metal with nonmetallic inclusions in accordance with GOST 801-78 standard increase the yield of acceptable batches of rolled material from the first inspection from 63 in 2007 to 90% in 2009.

Analysis of contamination with nonmetallic inclusions of ShKh15SG-V steel melted by the new technology with the evaluation in accordance with ASTM E-45 (method A)

In the situation existing at the beginning of 2008, the Dnepropetsstal' company could not only satisfy the requirements on foreign companies for the supply of rolled stock of ShKh15SG-V steel because of the more stringent method of inspecting the content of nonmetallic inclusions in the metal in accordance with the ASTM E-45 (method A) standard. At the same time, the orders by the companies Dapinia Krasnik S.A. *(TU

Table 2. The requirements of foreign companies on ShKh15SG-V electric steel for the content of nonmetallic inclusions in rolled material in evaluation by the ASTM E-45 (method A) method.

Company - customer	Permissible limiting values of size number for types and series of inclusions							
	Sulphides A		Oxides B		Silicates C		Globules D	
	Thin	Thick	Thin	Thick	Thin	Thick	Thin	Thick
Dapinia TP No. 278—05* (TU DCC 002)	2.0	1.5	1.5	1.0	0	0	1.0	1.0
Timken TP No. 278-05*	2.0	1.5	1.5	0.5	0	0	1.0	0.5
Krasnik S.A. (TU WTm-138)	2.0	1.0	1.5	0.5	0	0	0.5	0.5

* Standard technological documents of Dneprospsstal'

WTm-138), Timken, etc, were of considerable interest for the production programme of the company because of the large volumes of rolled material with high profitability parameters.

A special feature of the ASTM E-45 (method A) method of inspecting the for the content of the nonmetallic inclusions of four series (sulphides A, oxides B, silicates C, globules D) with the differentiated estimation of each of the four types on the basis of the so-called thin and thick inclusions is shown in Table 2.

As indicated by Table 2, the most stringent requirements of the previously mentioned companies using the ball bearing steel are the requirements of the Polish partner of Dneprospsstal' WTm-138, since the size numbers for the oxides in the 'thick' series B_{thick} and also the globules of the thin D_{thin} and thick D_{thick} series are 0.5 smaller in comparison with the requirements of Dapinia.

It should be mentioned that in accordance with the requirements of the customer WTm-138, it is necessary to take into account only the maximum and not mean size numbers of the nonmetallic inclusions, as in the case of orders from the Dapinia company and, correspondingly, the technological standard documents of Dneprospsstal' (TU DSS 002).

Analysis of the statistical data of the estimates of the size of the nonmetallic inclusions

in the metal of the batches of rolled material of ShKh15SG-V melted by the technology available in 2008 using ferrosilicomanganese, shows that the yield of suitable batches at the first delivery inspection with respect to the nonmetallic inclusions estimated using the ASTM E-45 (method A) method for the orders of Dapinia increased to 86%.

The main type of inclusions causing rejection were oxide inclusions (90%).

Thus, the difficulties in fulfilling the orders from this company were based on producing rolled material inspected on the basis of the oxide inclusions of series B, in particular, thin series B_{thin} .

The results of evaluation of the degree of contamination of the melt produced by the existing technology in accordance with the WTm-138 standard shows that the yield of suitable batches of rolled material at the first inspection was only 43%. The main type of inclusions because of which the delivery characteristics of the Lord material may not satisfied where the oxide inclusions in the steel of series B, and also the globular inclusions D_{thick} and D_{thin} . The fraction of these inclusions taking into account the rejects on the basis of the inclusions B_{thick} and B_{thin} was 55%, and the fraction of the inclusions B_{thin} was dominant for all the inclusions.

Analysis of the data in the inspection of the batches of rolled stock of ShKh15SG-V steel, melted to fulfil the order Wtm-138, with the quality of material inspected in accordance with the ASTM E-45 (method A) method

In 2009, experimental melts produced of the steel in order to develop the technology of melting metal to fulfil the order Wtm-138, taking into account the inspection of rolled material for the content of the nonmetallic inclusions in accordance with ASTM E-45 (method A). The difference between the new technology and that used in 2007 was that the metal in the DSP-60 furnace was the oxidised, after skimming the oxidation slag, by MnS17 ferrosilicomanganese with the addition of this substance to the mean grade Mn content taking into account the residual content in the steel.

A small amount of FS65 ferrosilicium for

correcting the silicon content of the metal was added together with solid slag materials (SSM) to the ladle-furnace.

The metal product in the ladle-furnace was deoxidised with aluminium (on average 1.3 kg/t). The degree of pickup of the introduced alloying and deoxidation agents was as follows, %: manganese 93.8, silicon 72 and aluminium 37.

During treatment of the metal in the later-furnace samples were taken from experimental melts for determining the variation of the chemical composition of the slag: No. 1 – after treatment of the metal with SSM in the ladle-furnace, No. 2 – in the furnace-ladle unit after renewing the slag, No. 4 after vacuum treatment (Table 3).

The MgO content in the slag of the experimental melts was considerably lower in comparison with the slags of the standard melts whose metal was characterised by large size numbers of the nonmetallic inclusions.

Table 3. Variation of the chemical composition of the slag of experimental melts during the refining of ShKh15SG-V steel in the ladle-furnace

Melt No.	Sample No.	Mass fraction of components, %						
		CaO	MgO	Al ₂ O ₃	SiO ₂	FeO	CaF ₂	S
Experimental melts								
B21445	1	43.7	8.00	17.0	11.30	0.67	17.0	2.19
	2	60.5	3.40	8.14	7.27	1.80	18.0	0.42
	3	45.3	5.10	12.38	5.93	0.23	30.1	0.79
	4	52.4	3.88	18.57	8.65	0.24	15.0	0.98
B21928	1	51.4	6.06	9.12	8.69	2.41	21.4	0.62
	2	47.7	6.79	10.92	10.77	1.08	22.0	0.56
	3	47.7	5.58	17.90	10.12	0.23	17.1	1.02
B21960	1	48.9	7.28	13.68	11.47	0.43	16.03	1.54
	2	53.3	3.40	6.52	9.00	1.22	22.9	0.53
	3	54.4	4.61	11.08	10.12	0.27	18.37	0.72
Series melts with higher MgO content								
B14405	1	50.26	15.36	6.80	22.09	0.66		
	2	49.75	17.88	6.80	23.43	0.81		
	3	50.26	17.37	7.30	20.06	0.15		
B14407	1	51.43	15.88	8.20	22.85	0.77		
	2	48.14	17.60	7.0	16.34	0.91		
	3	54.25	9.84	13.6	14.96	0.70		

To stabilise the quality of the rolled stock of experimental melts, the technological instructions included the measures for reducing the MgO content of the melt in the stages of melting and refining the steel.

In accordance with other parameters of melting the ball bearing steel by the new technology, the content of the elements, in particular, aluminium and the calcium, were stabilised. These elements determine the type and amount of the nonmetallic inclusions. The actual mass fraction of aluminium, calcium, titanium, oxygen and nitrogen in ShKh15SG-V steel in the experimental melts was in the following ranges:

Al, %	Ca, ppm	Ti, %	S, %	[O], ppm	[N], ppm
0.024...0.038	6...10	0.002...0.003	0.002...0.008	9...12	60...90
0.028	7	0.002	0.004	10	75

The results obtained in the delivery and research inspection of the material of the experimental melts using the size scales of GOST 801-78 and ASTM E-45 (method A) standards, and also taking into account the requirements of the companies Dapinia and WTm-138, are presented in Table 4.

The data in Table 4 shows that of the metal of the 15 melts of the steel after fulfilling all the technological instructions was certified at the first delivery inspection. The rolled material of the three steel melts, pro-

duced with the variation of the normalised conditions of the technological instructions, did not fully satisfy the requirements of the foreign standards in accordance with ASTM E-45 (method A), and because the mean size of the series of the oxide inclusions B_{thin} was exceeded (1.60...1.86 size number with the standard not higher than 1.56).

Analysis of technological documents for the three melts of the steel showed that the deviations in the operations in the course of melting consisted of long-term treatment of the metal in the furnace-ladle unit (110–120 min, with the standard value not higher than 90 min), which did not provide for the carburisation of the steel prior to vacuum treatment with coke packets, and also with the high content of aluminium (0.039...0.050%), with the control value not higher than 0.035% of is repeated delivery inspection, the rolled material for three melts was also certified as suitable.

As mentioned previously, a special feature of the requirements WTm-138 is the regulation of the number of inclusions for each series on the basis of the maximum (not mean) size.

The quantitative evaluation of the efficiency of the proposed technology regarding the purity of the produced rolled material with respect to the nonmetallic inclusions, investigations were carried out on 51 specimens of metal of nine batches of rolled material in the

Table 4. Comparative data obtained in the delivery inspection of rolled material of the experimental melts of ShKh15SG-V steel for the content of the nonmetallic inclusions in accordance with GOST 801-78 and ASTM E-45 (method A) standard taking into account the authors by foreign companies

Number of melts	Number of inspected batches (four deliveries from first inspection)	GOST 801-78 for standards for five groups of rolled stock						ASTM E-45 (method A) for standards			
		1	2	3	4	5	Yield of suitable metal from first inspection	Dapinia		WTm1-138	
								Batches, No.	Yield of suitable metal, %	Batches	Yield of suitable metal, %
15	29/29	-	-	-	7/7	8/8	100	11/11	100.0	3/3	100
36	77/74	2/2	3/3	-	8/8	9/9	100	49/46	93.9	-	-
E51	106/103	2/2	3/3	-	15/15	17/17	100	60/57	95.0	3/3	100

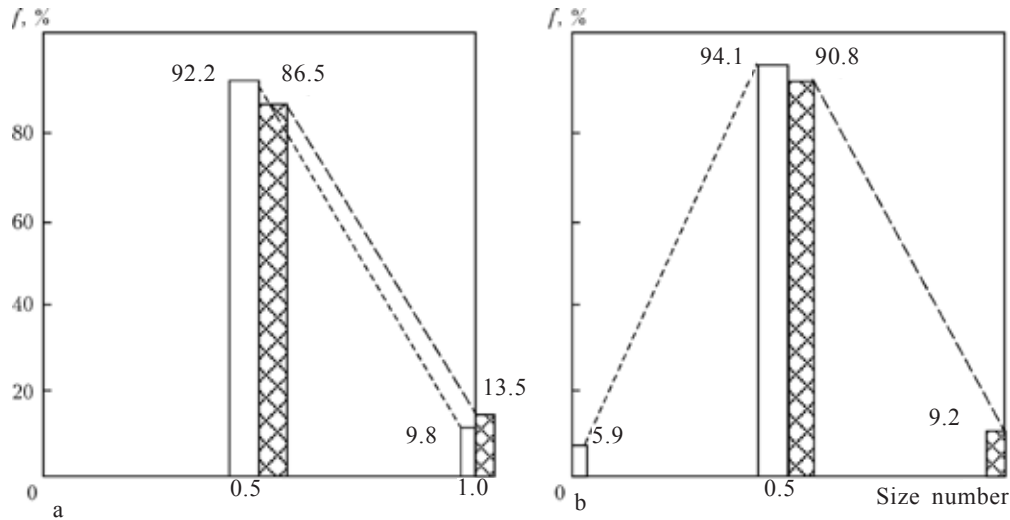


Fig. 2. The frequency of distribution of the specimens f of the ShKh15SG-V steel with the sizes of nonmetallic globular inclusions D_{thin} (a) in D_{thick} (b) of rolled stock of the experimental (open columns) and series (cross hatched columns) melts in evaluation of the contamination with nonmetallic inclusions using the standards WTm-138 and ASTM E-45 (method A).

range 18–90 mm, and also delivery inspection of 783 specimens of the standards melt of the steel, produced in 2008. The results are presented in Fig. 2 and 3.

Analysis of the data in Fig. 2 shows that the number of the inclusions larger than the normalised size number (Table 2) in the rolled material of the experimental is considerably smaller than in the series melts, according to the types of globular inclusions D_{thin} 1.2 times, D_{thick} 9.0 times, and oxide inclusions B_{thin} 1.6 times. The mean size of the oxide inclusions B_{thick} of the rolled material the experimental mouse was considerably lower than that of the metal produced by the ‘old’ technology, and equalled 1.2 in comparison with 1.59.

In October 2009, the ShKh15SG-V electric steel was melted in a DSP-60 furnace in accordance with the direct order of WTm-138 company. The results of research and delivery inspection of the quality of rolled material (36–50 and 45 μm cylindrical stock) with respect to the content of the nonmetallic inclusions showed that the quality fully satisfies the standards of WTm-108 and the order was sent to the customer. The results of comparative analysis of the quality of metal indicate that it should be efficiently wide in the range of production of ShKh15SG-V steel also in accordance with the stringent

standards of WTm-138.

In addition to increasing the quality of the ShKh15SG-V with respect to the content of the nonmetallic inclusions, the new technology reduces the specific consumption of ferroalloys. In producing 51 industrial melts of the steel ShKh15SG-V in the DSP-60 furnace, the specific consumption of the ferroalloys decreased by 3.14 kilograms/t, and one FMn 78A ferroalloys was used it decreased by 3.34 kg/t, and in the case of FSsix 5 x 1.62 kg/t.

The production cost of ShKh15SG-V steel, produced using MnS17 ferrosilicomanganese, in comparison with the currently available technology using FMn78A ferromanganese and FS65, decrease by 29.53 hrivna/t. Analysis of the technical and economic parameters of melting the ball bearing electric steel confirms that it would be possible to increase further the economic efficiency of production of this steel.

Conclusions

1. The innovation technology of melting the ShKh15SG-V electric steel in the DSP-60 arc furnaces with ladle treatment in the furnace–ladle unit was developed and introduced into production. The technology is based on vacuum treatment and diversification of the

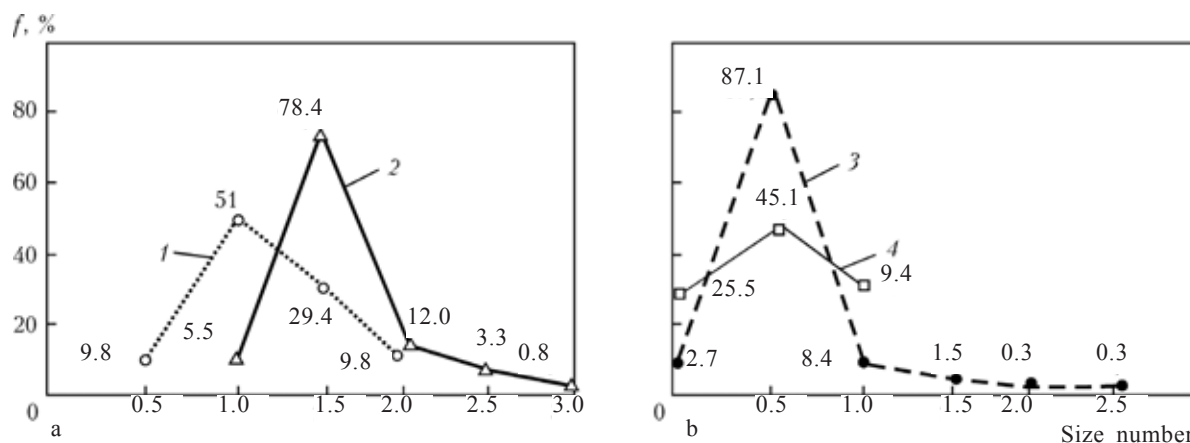


Fig. 3. The frequency of distribution of the specimens of ShKh15SG-V steel with the size of the oxide inclusions B_{\min} (a) and B_{thick} (b) of rolled stock of the experimental (1, 2) and standard (3, 4) melts in evaluation of the degree of contamination with the nonmetallic inclusions using the standard ASTM E-45 (method A) and WTM-138.

ferroalloys (ferrosilicomanganese Mn17 replaces high-carbon ferromanganese FMn 78A) with the reduced consumption of FS Ferris silicon and showing the increase of the yield of suitable batches of rolled material from the first delivery inspection in accordance with the standards of the foreign companies based on the evaluation by the ASTM E-45 (method A) standard.

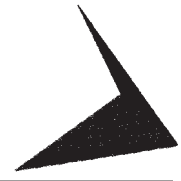
The experimental results show that the quality of rolled stock of ShKh15SG-V steel, produced by the new technology of production of metal, in the evaluation in accordance with the ASTM E-45 (method A) is considerably higher in comparison with the rolled material produced by the existing technology using the FMn78A ferromanganese and FS65 ferrosilicium; the yield of suitable fractions from the first delivery inspection of the degree of contamination with the nonmetallic inclusions in accordance with GOST 801-78 and ASTM E-45 (method A) standards increased from 63

to 90%, and for the individual size groups of the rolled material up to 100%.

3. It is also shown that the new technology of melting electric steel ShKh15SG-V, developed and introduced into industrial production, using MnS17 ferrosilicomanganese reduces the consumption of ferromanganese FMn 78A by 92%, and that of ferrosilicium FS65 x 30%, in comparison with the standard technology, and the production cost of steel is reduced by 29.53 hrivna/t with the possibility of further improvement of technical and economic parameters.

References

1. Panchenko A.I., et al., *Sovremennaya Elektrometallurgiya*, 2007, No. 4, 49–55.
2. Zaitsev A.I., et al., *Materialovedenie*, 1998, No. 5, 18–25.
3. Zhrebtsov D.A., et al., 1999, No. 2, 63–65.
4. Gasik M.I., et al., *Elektrometallurgiya*, 2010, No. 5, 2–14.
5. Gorobets A.P., et al., 2008, No. 1, 48–54.



Brazing of titanium aluminide with rapidly hardened foils

S. V. Maksimova and V. F. Khorunov

E.O. Paton Electric Welding Institute, Kiev

The results of investigations of the structural state of rapidly-hardened foils based on the Ti—Zr—Fe—(B) system, produced by rapid cooling of the melt, are presented. Peculiarities of the formation of titanium aluminide brazed joints made by high-temperature vacuum brazing and rapidly-hardened strips are studied.

The term rapidly-hardened alloys refers to the alloys produced by rapid cooling of the melt (quenching) or vapour phase condensation. The critical cooling rate is a qualitative criterion of the stability of the super cold melt and determines the temperature–time conditions of suppressing the solidification process.

The rapidly hardened alloys can differ from the cast alloys by the high-dispersion dendritic, microcrystalline and amorphous structure, depending on the technological conditions of production.

A special feature of the rapidly hardened microcrystalline alloys case the formation of metastable intermediate phases [1]. The high cooling rates of the alloys, containing nonmetallic inclusions, are characterised by the susceptibility to suppressing nucleation so that it is possible to produce the amorphous condition without the so-called amorphisation agents (phosphorus and boron).

The rapidly hardened alloys are characterised by high chemical homogeneity, plasticity, corrosion resistance, small thickness and other unique properties. The method of superfast quenching has been used to produce plastic homogeneous foils from brittle alloys [2].

Previously, the alloys were used as brazing alloys only in the form of powder and this required a binding substance. This complicated the brazing process. The brazing alloy with the amorphous structure can be used in the form of base elements of any shape. Chemical homogeneity of the brazing alloy ensures the uniform melting of the brazing alloy through the volume.

The high degree of structural disorder and defectiveness [3] result in high diffusion mobility of the atoms and efficient wetting of the surface to be brazed. This in turn determines the favourable conditions for solidification of the brazed joints, results in the absence of defects and ensures the optimum strength

of the joint.

The brazing alloys with the amorphous structures of the following systems are used widely in industry for brazing: Ni–Cr–Si–B (for stainless steels); Ti–Cu–Ni, Ti–Zr–Cu–Ni (for titanium and its alloys; Cu–Ni–Sn–P (for copper and its alloys).

The amorphous condition of the brazing alloys based on the Ni–Cr system is produced by the addition of small amounts of amorphising elements: boron and silicon. The group of the metallic bulk-amorphising materials including alloys of the Ti–Cu–Ni, Ti–Si Zr–Cu–Ni, Zr–Ti–Ni, Cu–Zr–Ti systems in which the crystalline condition contains the intermetallic compound TiCu, Zr₂Cu, ZrCu_{3,6} and ZrCu with the ternary Laves phase Ti–SiCu₄ [4]. However, for high-temperature applications it is desirable to use brazing alloys with no copper.

In this work, the results are presented of investigations of the rapidly hardened brazing alloys based on the Ti–Zr–Fe–(B) system, produced by melt spinning, and also the compounds of titanium aluminide, produced using these brazing alloys.

For the experiments, the alloys were melted in a vacuum furnace by arc heating. Melting was carried out in a copper watercooled solidification mould with the ingots turned over 2–5 times to ensure the average chemical composition. The produced ingots were placed in a vacuum chamber, melted in purified argon (helium), excess pressure was generated (1.8 · 10⁵ Pa) and used for displacing the metal jet on the external surface of the copper disc–drum spinning at the given speed (no more than 40 m/s).

The quenching rate was regulated in a wide range by varying the linear speed of revolution of the drum in accordance with the geometry of the nozzle through which the liquid metal was discharged, the pressure above the melt, and the distance from the nozzle to the surface of the drum.

The produced rapidly quenched (hardened) foil of the brazing alloy was placed between the specimens of titanium aluminide to be brazed, brazing was carried out in a backing

furnace with radiation heating at a temperature of 1150°C, 60 min. Metallographic examination was carried out by optical and electron scanning microscopy.

The brazed material in the experiments was in the form of intermetallic alloys of gamma titanium of two types: 48XD, produced by powder metallurgy (Fig. 1a), and 4022 (Fig. 1b), produced by conventional casting methods, especially electron beam melting (Fig. 1b).

The alloys of the sub-stoichiometric composition Ti-(46–49)Al were produced in the two-phase ($\alpha_2 + \gamma$) the region, where the α_2 -phase is represented by the Ti₃Al intermetallic compound, and the γ -phase by the TiAl intermetallic compound.

The investigated alloys containing the same atomic fraction of aluminium (48–49%), but the morphology of the structural components of the alloys slightly differs. In the 40XD alloy (Ti–45Al–2Nb–2Mn–0.8 TiB₂) needle-shaped borides form on the background of the lamellar structure of γ -TiAl and the α_2 -phase. The atomic fraction of boron in the borides is 66.67–71.02% (Table 1).

It should be mentioned that in the initial condition, the cast alloy 4822 (Ti–48Al–1.6Nb–2Cr) does not contain the lamellar structure but there are dispersed particles

Table 1. Chemical composition of the structural components of the brazed materials

Spec- trum No. studied	Atomic fraction of elements, %					
	Ti	Al	Mn	Nb	B	Cr
Alloy 48XD						
1	48.00	48.65	1.51	1.85	0	-
2	53.25	42.74	1.94	2.07	0	-
3	22.52	5.54	0.18	0.74	71.02	-
4	25.18	7.04	0.29	0.82	66.67	-
Alloy 4822						
1	48.89	47.70	-	1.61	-	1.80
2	49.36	47.54	-	1.52	-	1.57
3	54.49	34.33	-	1.87	-	9.31
4	52.87	38.47	-	1.96	-	6.70
5	51.22	43.36	-	1.70	-	3.72

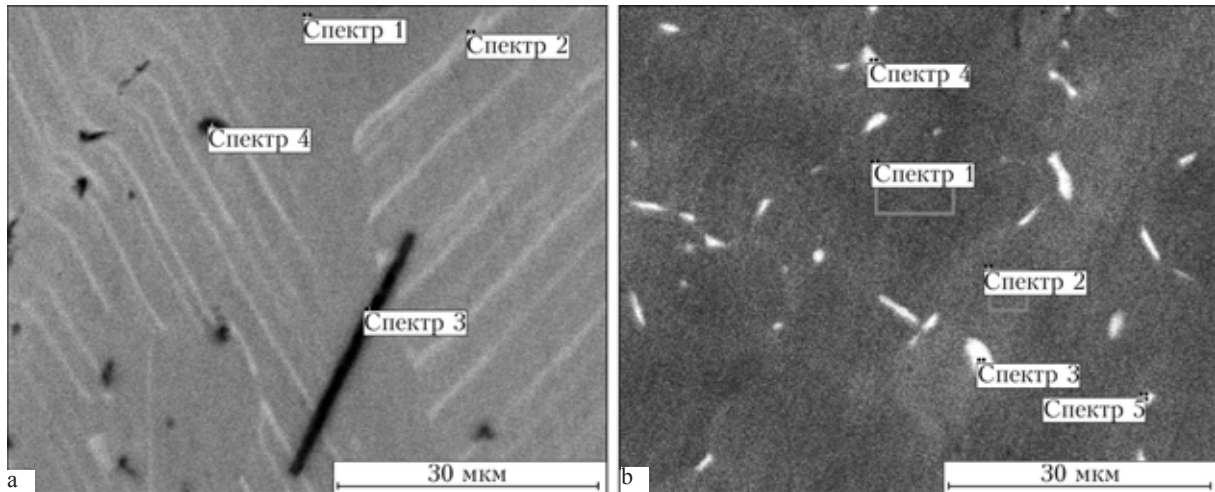


Fig. 1. Microstructure of the brazed intermetallic alloys: a) 48XD, b) 4822.

of the α_2 -phase (white) containing a higher amount of chromium (Fig. 1b).

The brazing alloys in the form of the rapidly hardened foils are characterised by a homogeneous glassy structure (Fig. 2a), both for the Ti–Zr–Fe and Ti–Zr–Fe–B system alloys. In some areas there were discrete discontinuities in the foil in the form of perforated sections. After etching the foil examination shows the cellular ultra-fine dispersed structure of the Ti–Zr–Fe alloy (Fig. 2b), and high resolution equipment is required for studying this structure.

All the component chemical elements of the brazing alloy are distributed uniformly in the width of the rapidly hardened foil (Fig. 3), with the exception of zirconium whose amount decreases of the external surface of

the foil which is in contact with air.

The negative feature of the brazed joints in the 48XD intermetallic alloy, produced by high-temperature vacuum brazing, and of the brazing alloys based on the Ti–Si in–Fe system, containing boron (no more than 2.5 at.%), is efficient wetting and spreading on, aluminate, and also the presence of complete fillets on both sides (Fig. 4a, b).

The presence of boron in the brazed material and the brazing alloy results in the formation of single boride needle-shaped precipitate in the boundary zone of the parent metal and the brazed joint (Fig. 4c, d).

In the metal of the brazed joints on the background of the light matrix with the composition 57.08 Ti–31.16Al–5.16Fe–2.21Zr–2.3Nb there were crystals of dark grey grains,

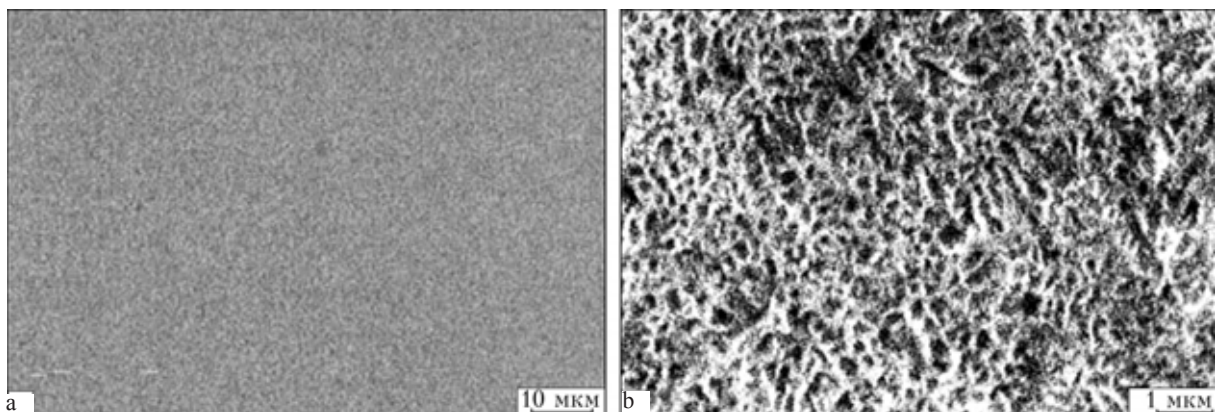


Fig. 2. Microstructure of the brazing alloy of the Ti–Zr–Fe system in the rapidly hardened condition prior to (a) and after (b) etching.

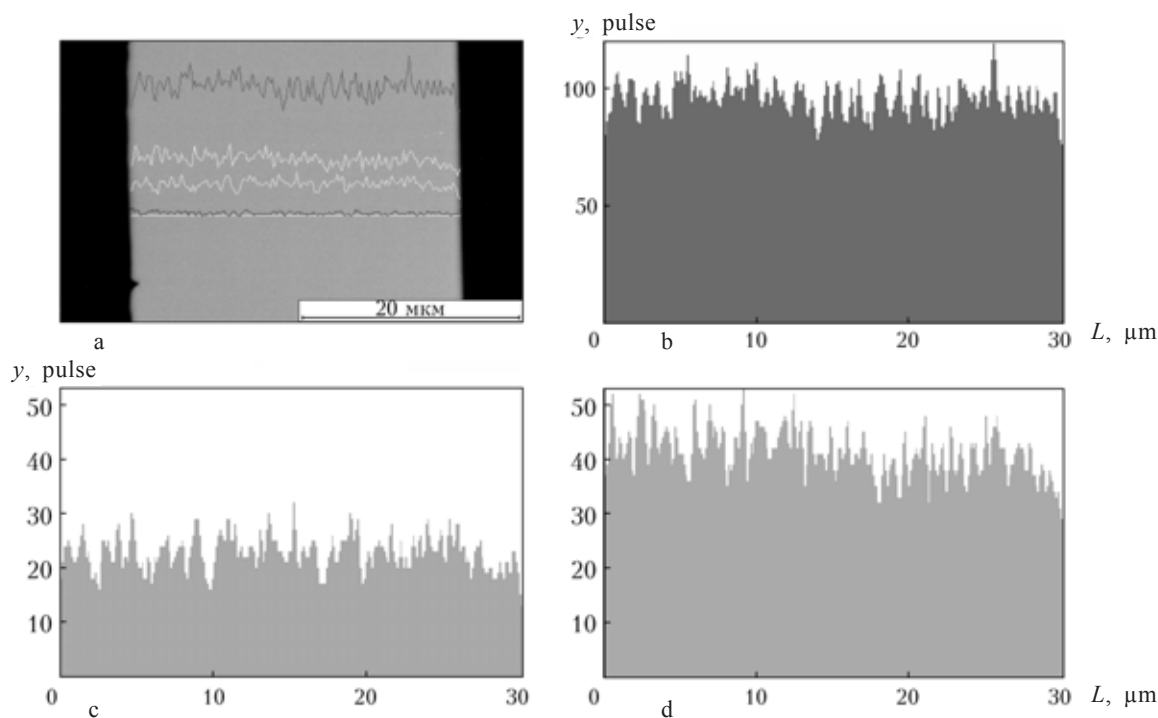


Fig. 3. The investigated section of the rapidly hardened Ti–Fe–Zr foil in the reflected electrons (a) and qualitative distribution of titanium (b), iron (c) and zirconium (d) in the width of the foil; y is the number of pulses, L is the length of the investigated section.

containing approximately 43 at.% of aluminium. The atomic fraction of aluminium in the light grey grains decreases to 28–35%.

In accordance with the equilibrium diagrams [5] it may be assumed that the grains of the phases TiAl and Ti₃Al solidify. In a small number cases the brace joint contained discrete ultrafine precipitates of the light phase with the size of approximately 1 μm or smaller in which the atomic fraction of aluminium decreases to 28% and that of zirconium and does not exceed 2.67%.

In brazing intermetallic alloys of titanium gamma aluminide of two grades (48XD and 4822) together (the alloys differ by the production methods), the structure of the metal of the joint is almost identical with that of the previous specimen.

A small width boundary line is found on the side of the 4022 alloy, and a phase whose chemical composition is identical with the composition of the parent metal and contains approximately 45% aluminium, forms along the joint as a band.

There are sometimes areas in which the

metal of the matrix of the joint, containing 33 at.% of aluminium and approximately 1 at.% of chromium, penetrates approximately 25 μm into the depth of the alloy (Fig. 5a). Relatively complete fillet sections (Fig. 5b) form.

On the side of titanium gamma aluminide of grade 48XD there was the area with the typical directional growth of the plate-shaped formations of the two phases TiAl and Ti₃Al which form on the substrate of the parent metal and grow into the 4822 alloy (Fig. 5c).

The width of the welded joint is the same for the two brazing alloys. This is approximately 125 μm and is determined by the width of the foil. The reduction of the mass fraction of boron from 1.0 to 0.5% in the brazing alloy has no significant effect on the formation of the brazed joints.

It should be mentioned that the needle-shaped borides solidified only in the zone of the 48XD alloy in the vicinity of the welded joint (Fig. 5c). In the formation of the brazed joint on the side of the fillet section at the axis examination showed the precipitation

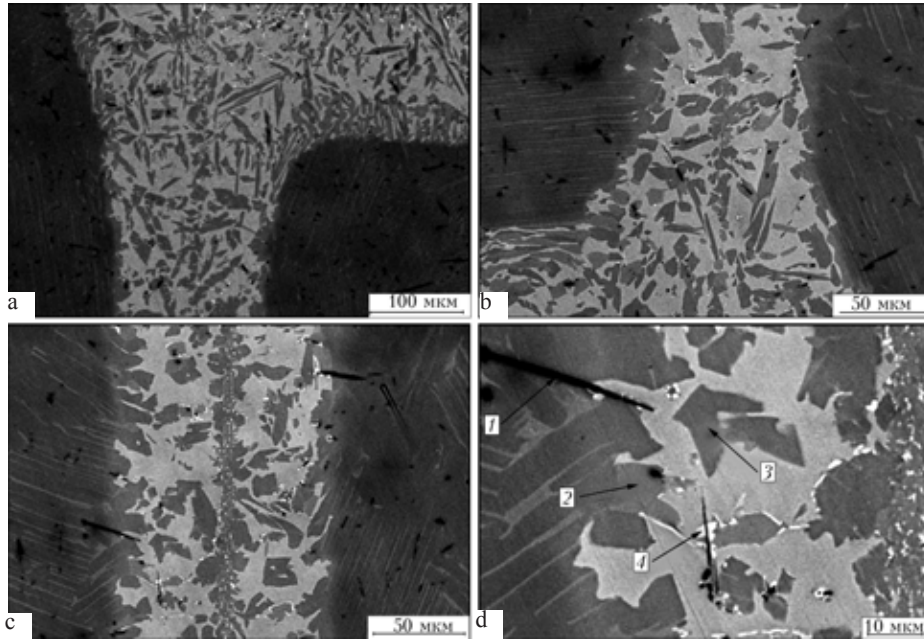


Fig. 4. Direct (a) and inverse (b) fillet of the brazed joints in the 40XD alloy, produced using the Ti–13.1Zr–24.7Fe–5B alloy, and also the microstructure of the brazed joint (c, d ; 1) borides, 2) light grey grains, 3) dark grey grains, 4) white ultrafine phase.

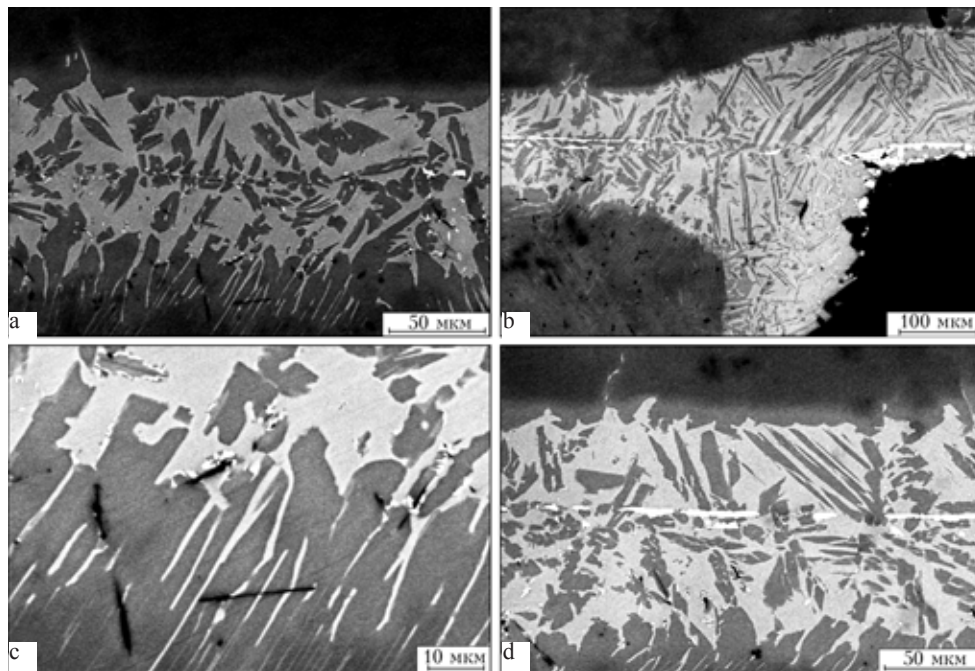


Fig. 5. Microstructure of the brazed joint in the 4822 and 40XD intermetallic alloys, produced using the Ti–13.4Zr–24.4Fe–2.5B brazing alloy.

of intermittent filament-like precipitates of a light phase containing approximately 2 at.% of zirconium (Fig. 5d).

This intermittent precipitation of the phase

is preferred to the continuous and does not disrupt the integrity and density of the brazed joint and of the fillet section.

Conclusions

1. It has been established that the rapidly quenched foil is based on the Ti–13Zr–24 Fe–(2.5–5) B are characterised by the microcrystalline structure with the uniform distribution of the components of the chemical elements in the width of the foil.

2. The experimental results show that the application of the brazing alloys in the form of the rapidly quenched foil based on the Ti–Zr–Fe–B system for brazing the intermetallics alloys 48XD (Ti–45Al–2Nb–2Mn–0.8TiB₂) and 4822 (Ti–48Al–1.6Nb–2Cr) and shows the formation of high-density brazed joints and fillet sections. In the brazing of 48XD intermetallic alloy, containing TiB₂ (in the homogeneous condition), the solidification of the borides in the form of discrete needle-shaped precipitate was detected not only in the 48XD parent metal but also in the zone of the brazed joints adjacent to the parent metal.

3. The results also show that in brazing the

48XD and 4822 intermetallic alloys together, the borides precipitate only in the zone of the 48XD alloy bordering with the joint line.

4. It has been established that when brazing intermetallic titanium alloys with the rapidly hardened brazing alloys of the Ti–Zr–Fe–(B) system with no aluminium, the joint is saturated with the aluminium of the brazed material as a result of high diffusivity of the latter, and cooling is accompanied by the crystallisation of the phases with the composition similar to that of the parent metal.

References

1. Fatkulin O.Kh., Tekhn. Legkikh Splavov, 2005, No. 1, 24–31.
2. Khorunov V.F. and Maksimova S.V., Avt. Svarka, 2005, No. 10, 35–40.
3. Matveeva N.M., et al., Metally, 1997, No. 6, 109–112.
4. Kovneristyi Yu.K., Bulk-amorphising metallic alloys, Nauka, Moscow, 1999.
5. Lyakishev N.P. (editor), Equilibrium diagrams of the binary metallic systems, a handbook in three volumes, Mashinostroenie, Moscow, 1997.

Repair of flaps of the regulating nozzle of aviation gas turbine engines by high-temperature vacuum brazing

I. S. Malashenko, V. E. Mazurak, V. V. Kurenkova, T. N. Kushnareva and Yu. V. Gusev

E.O. Paton Electric Welding Institute, Kiev

The possibilities of using a binary boron-containing brazing alloy and a similar alloy with a filler of 20 % eutectic composition Ni–12%Si in the formation of joints of ZhS6K alloy in the conditions of repair brazing in vacuum are compared. The effect of different conditions of annealing on the physical–mechanical properties of parent metal of a flap of an adjustable nozzle of aircraft gas turbine engines (AGTE) and its joints after brazing is considered. The prospects of application of a complex brazing alloy with boron and silicon in the technology of restoration of hot circuit parts of GTE by brazing are shown.

Introduction

The components of the hot circuit of thermally stressed turbines are subjected to thermal fatigue as a result of the formation of high alternating internal stresses associated with the cycling variation of the temperature of the gas flow and, correspondingly, with nonuniform heating and cooling of the walls of the component. The stresses, formed during the heating and cooling cycles at the maximum level results in local failure of components in the form of thermal fatigue cracks.

The failure in thermal fatigue may be regarded as low- or high-temperature and is determined, in accordance with [1], by the type of fracture – transcrystalline or intragranular. The most important factor, influencing the nature of deformation and failure of the component (in addition to the structure of the metal of the casting), is the temperature resulting in the maximum stresses or deformation in the thermal loading cycle.

To recondition the damaged guide blades of

the nozzle system or the flaps of the regulating the nozzle of the aviation gas turbine engine (AGTE), produced by casting, it is efficient to use high-temperature vacuum brazing [2–4] or use a neutral medium – argon [5].

Brazing has a number of advantages in comparison with argon-shielded arc welding, especially in the repair of components produced from high-alloyed creep-resisting nickel alloys.

Because of the high-strength of the brazed joints, brazing is regarded as an alternative of welding. Brazing is not accompanied by the formation of high thermal stresses, typical of argon-shielded arc welding, there is no risk of cracking of the weld metal or the heat affected zone in the precipitation of the hardening γ' -phase during cooling of the welded joints or heat treatment [4, 6, 7].

In [5–8] investigations were carried out into the technological special features of isothermal vacuum brazing of creep resisting alloys with different levels of alloying. The application of composite brazing alloys

results in the chemical composition and physical–mechanical characteristics of the brazed joints being similar to the properties of the brazed metal so that the components of aviation gas turbine engines can be efficiently prepared by brazing.

The application of the multicomponent composite brazing alloys with a filler produces brazed joints (structures) with reliable functional properties: creep resistance, corrosion resistance, resistance to thermal and multi-cycle fatigue. It is essential to optimise the conditions of high-temperature brazing in subsequent heat treatment of the components recondition by brazing for creep resisting alloys with different degrees of alloying.

The main task in the investigation was the evaluation of the universality of the boron- and silicon-containing brazing alloys for high-temperature brazing of ZhS6K alloy in comparison with the basic binary brazing alloy 40% (Ni–Co–Cr–Al–2.5%B) + 60% Rene-142.

Experimental materials and procedure

The brazed joints in ZhS6K alloy were produced from the metal of cast flaps of the regulating nozzle of the aviation gasturbine engine after approximately 500 hours in service. 1.6 mm sheets were machined into blanks for the specimens for the mechanical tests. Prior to brazing, the blanks were annealed in vacuum at 1220°C for 1 h to dissolve the fine-dispersion precipitates of the γ' -phase in a nickel matrix [8].

When selecting the variants of the brazing alloys, it was taken into account that the chemical composition of the brazing alloys should be similar to the composition of the brazed alloy and ensure wetting of the surface of the component at the brazing temperature with minimum dissolution of the base. The basic brazing alloy was the alloy produced by Praxair Surface Technologies (USA), wt. %: Ni–9Co–14 Cr–4Al–2.5B (No. 1). The reduction of the degree of dissolution of the parent metal in the molten brazing alloy was ensured by adding to the brazing mixture the fillers produced from the powders of the nickel

superalloys, in particular, Rene-142, used in repair technology [9].

A promising brazing alloy is the composition consisting of two low-melting brazing alloys – boron-containing Ni–9%Co–40%Cr–3.5% Al–2.5%B and silicon-containing alloy with the eutectic composition Ni–12%Si (HC12) and also the filler in the form of the Rene-142 alloy. The binder was in the form of a solution of acrylic resin in commercial acetone.

In the group of the powder fillers, the René-142 alloy (wt. %: Ni–6.7Cr–11.5Co–1.4Mo–4.7 W–6.4 Ta–6Al–2.8Re–1.5 Hf–0.12C) differs by the irrational alloying system – tantalum, hafnium and rhenium result in the formation of the brazed joint with satisfactory strength and creep resistance, hafnium and tantalum limit the extent of diffusion processes in the Ni–Cr–Co–W–Mo–Ti–Al creep resisting systems and increase the energy of atomic bonds [8].

The joints in the ZhS6K alloy were produced by filling a 1 mm wide gap with the brazing mixture or by contact brazing of the sheets with the initial gap of approximately 100 μm . To prevent displacement of the powder of the brazing alloy from the gap, a mesh made of EI-435 wire was welded to the rear part of the component. The length of the transverse gap in the 12 mm thick blank was 9 mm and, therefore, in the preparation of the specimen the brazed joint spread over the working part of the blank.

Brazing was carried out and temperatures of 1220...1225°C, 20–15 min in a vacuum of $8 \cdot 10^{-3}$ Pa.

The main methods of investigations of the structure of the brazed joints in the nickel group-resisting alloys in this study is scanning electron microscopy (CamScan-4) and electron probe microanalysis (Energy 200 energy-dispersing analyser). The microhardness of the individual zones of the brazed joint was determined using equipment Duromat 4000E for a Polivar Met optical microscope.

The characteristics of the strength and yield limit of the brazed joints were determined by testing the specimens in uniaxial tensile

loading in a R-0.5 tensile machine with the speed of movement of the clamp of $v = 1$ mm/min (strain rate of approximately $1.65 \cdot 10^{-3} \text{ s}^{-1}$). The tests were carried out at room temperature and at 900°C in air.

The mechanical properties of ZhS6K alloy and of brazed joints in the alloy

The task of the study was the optimisation of the composition of the brazing alloy for application in repair of the flaps of the regulating nozzle of the aviation gasturbine engine by high-temperature brazing. The main criterion for evaluating the brazing alloy used for this operation was the strength of the brazed joint at the working temperature of the component.

According to Fig. 1, the highest ultimate strength and yield limit were obtained in the specimens after service and annealing at 1220°C , 1 h + 900°C , 4 h. The basic strength of the ZhS6K alloy at 20°C was the mean ultimate strength of the specimens of ZhS6K alloy, subjected to heat treatment in the conditions of formation of the brazed joint, equal to 906.7 MPa, and the yield limit was 734.7 MPa.

The required combination of strength and plasticity of the metal was obtained after annealing in the conditions of thermal treatment of the cast flaps at 1160°C , 2 h + ageing

at 900°C , 4 h, or ageing after austenitising at 1050°C , 4 h (Fig. 1). The high strength (more than 1000 MPa) was combined with the relative elongation in the range 9–11%. The data in Fig. 1 show that various types of heat treatment in vacuum can be used to produce the required functional characteristics of the brazed joint in the service conditions.

The strength of the brazed joint was 0.78–0.98 of the strength of the parent metal (Table 1), and the higher values corresponded to the brazed joints produced using the 20%No. 1+20% HC12+60%Rene-142, ensuring efficient wetting of the brazed surfaces (wetting angle $\theta = 3\text{--}5^\circ$), the flow into the gap and the formation of a high-density high-quality joints with the minimum number of defects.

In addition to the high values of the strengths characteristics, the three-component brazing alloy guarantee the formation of brazed joints with satisfactory level of plasticity (the relative elongation 1.8–7.7%).

The content of HC12 in the complex brazing alloy and the type of binder were optimised. The results shows that the yield limit of the brazed joints produced with the brazing alloy with 20%HC12, was 742 MPa, and in the case of the brazing alloy with 15%HC12 it was 724.6 MPa. In welding, the first areas of plastic flow formed in the brazed metal and subsequently, with increasing strain hardening, they were transferred into the metal

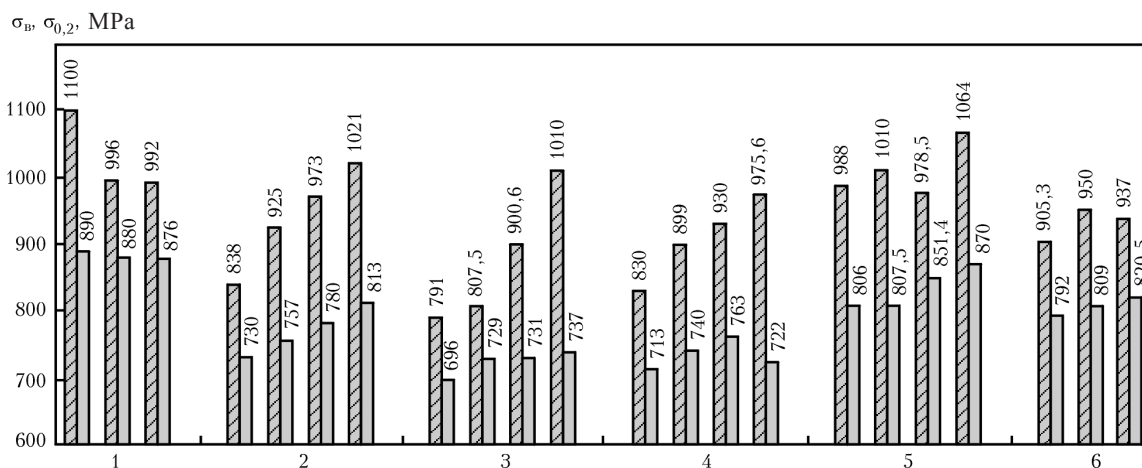


Fig. 1. Strength characteristics of the ZhS6K alloy (the metal of the flap) after service (1) and different heat treatment conditions in vacuum: 2) 1220°C , 1 h; 3) 1220°C , 1 h + 1160°C , 2 h; 4) 1220°C , 1 h + 1160°C , 2 h + 1050°C , 4 h; 5) 1220°C , 1 h + 900°C , 4 h; 6) 1220°C , 1 h + 1050°C , 4 h;) B,) 0.2.

Table 1. The mechanical properties of the brazed joint in ZhS6K alloy produced using the vicarage-reaction technology of brazing with composite boron- and boron-silicon-containing brazing alloys

Investigated item	Specimen No.	Cross section S , mm ²	$\sigma_{0.2}$, MPa	σ_B , MPa	ϵ , %
Initial metal	2-0	4.77	689.0	841.0	11.2
	2-1	4.24	752.0	978.6	10.7
	2-2	4.96	761.5	926.6	8.3
	9	3.62	722.3	975.6	6.7
After annealing at 1220°C, 1 h + 1160°C, 2 h + 1050°C, 4h	12	3.69	763.0	930.5	13.2
	4.1	13.48	—	628.6	0
	4.2	13.63	—	743.0	0
	5.7	3.93	711.4	719.0	0.2
Joint brazed with 40%No. 1+60%Rene- 142 alloy	5.8	4.57	730.0	796.4	1.7
	5.9	4.01	—	697.2	0
	6.0	4.28	680.0	761.0	3.0
	6.1	3.64	674.0	674.0	0
	6.3	3.78	—	623.0	0
	1-6**	3.16	745.0	826.0	1.8
	2-7**	4.50	654.0	700.0	0.5
Joint brazed with 20%No. 1+ 20% HC12 60%Rene-142 alloy	3-1**	4.00	742.0	777.6	0.7
	2-8*	3.88	745.8	847.0	2.0
	2.9*	4.56	677.6	882.0	7.7
	3.2*	4.75	722.5	831.0	3.0
	3.9*	4.62	717.7	877.0	4.0

*final heat treatment in vacuum at 1160°C, 2 h + 1050°C, 4 h; ** Final ageing at 960°C, 2 h

of the brazed joints.

The statistical processing of the results of the tests of the brazed joints in the ZhS6K alloy in tensile loading at 20°C is shown in Fig. 2. The basic composite brazing alloy No. 1 +60%Rene-142 and the complex brazing alloy with the addition of 20 wt.% of HC12 were compared. As indicated by the results obtained in [9–11], the addition of 15–20 wt.% of HC12 to the basic brazing alloy improves the fluidity and technological properties of the relatively ductile binary brazing alloy No. 1 +60%Rene-142. The Ni–Si eutectic brazing

alloy supports the filling of the gaps (cracks) without shrinkage defects and formation of pores, neutralising the higher activity of the boron-containing brazing alloy in comparison with the brazed alloy.

In accordance with the results presented in Fig. 2, there were no large differences not only in the level but also stability of the strength values. More than 70% of the tested specimens of the ZhS6K alloy, brazed with the brazing alloy containing HC12, showed the ultimate strength corresponding to 0.85–0.95 σ_B of the parent metal (760–850 MPa) and

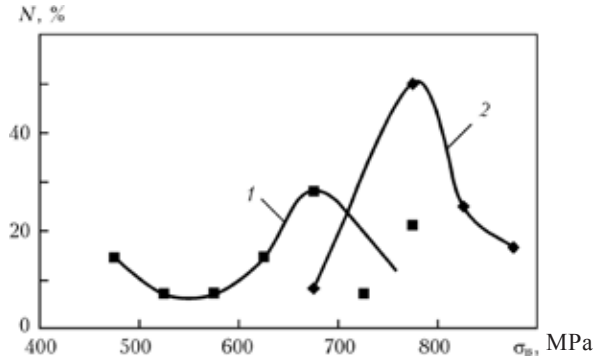


Fig. 2. Statistical curves of the values of ultimate strength B of the brazed joint in the ZhS6K alloy, produced with the boron-containing brazing alloys No. 1 +60%Rene-142 (1 – 18 specimens) and the complex brazing alloy 20% No. 1 +20%HC12+60%Rene-142 (2 – 12 specimens), N is the number of the specimens.

fractured at stresses above the yield limit in a wide range of σ_B (Fig. 2).

The lower level of the values of brittle strength (550–750 MPa) was recorded for the brazed joints produced with the boron-containing brazing alloy without HC12. This result also applies to the high-temperature brazing of the cast nickel alloys: VZhL12U, ZhS26, ZhS26NK, ZhS6U. The guarantee of plasticity (the relative elongation) of the joint is most evident for the complex brazing alloys with 15–20 wt.% HC12 [10].

Figure 3 shows the brittle strength of the brazed joints, produced with the boron-containing brazing alloy with the filler of Rene-142 powder without the addition of HC12. The mechanical properties of the brazed joint in ZhS6K alloy after standard two-stage heat

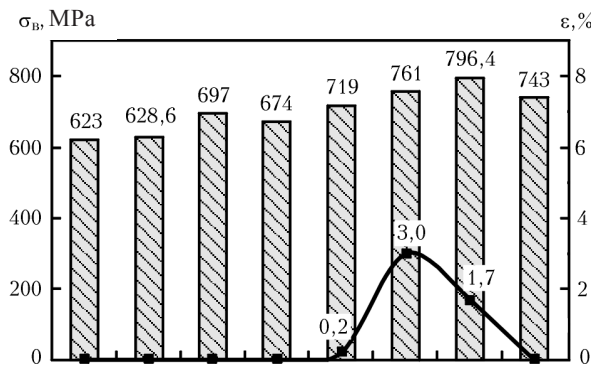


Figure 3. The mechanical properties of the brazed joint in the ZhS6K alloy, produced using the binary brazing alloy No. 1 + 60%Rene-142, after standard two-stage heat treatment (ageing at 10 50°C, 4 h).

treatment (ageing at 10 50°C, 4 h). At the maximum plasticity $\epsilon = 1.7\text{--}3.0\%$ the value $\Delta\sigma (\sigma_B - \sigma_T)$ is only 60–80 MPa.

Investigations were carried out into the strengthening tensile static loading, and also the endurance of the parent metal and the brazed joint at 900°C in air. The resultant values of the strengths of the brazed joint and high-temperature were fully satisfactory (Fig. 4). The specimens of the parent metal and the brazed joint (the width of the gap 1 mm) of the ZhS6K alloy, produced with the complex brazing alloys with the filler of Rene-142 powder, and annealed at 1160°C, 2h + 1050°C, 4 h, were tested at stresses of 294 10, 196.0 and 176.5 MPa (Table 2

Table 2. The endurance of the parent metal (ZhS6K alloy after two- and three-stage heat treatment) at a temperature of 900°C and loading at a stress of 294 MPa in air

Sample No.	Endurance τ , min	Elongation e , %	Heat treatment in vacuum
0-1	1320		
0-2	1200	6.1	
0-3	210		1220 °C, 1 h + 1160 °C, 2 h + 900 °C, 2 h
0-0	110	4.1	
0-6	730	9.5	
4-4	1260	11.7	1220 °C, 1 h + 900 °C, 4 h

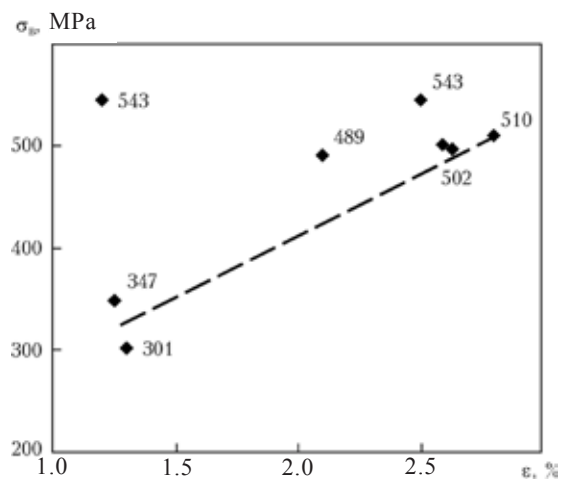


Fig. 4. Relationships of the strength of the brazed joint in ZhS6K alloy and relative elongation at 900°C.

Table 3. The endurance of the brazed joint in the ZhS6K alloy (second Lutskaya flap) produced with the complex brazing alloy 20 No.1+20% HC12+6% Rene-142 after two-stage heat treatment ($T_{\text{test}} = 900^{\circ}\text{C}$)

Sample No.	σ , MPa	Endurance τ , min	Elongation ε , %	Vacuum heat treatment
0	196	180	1.02	
1	176	540	8.00	
2	176	90	4.30	1160 °C, 2 _H + + 900 °C, 2 _H
3	176	600	7.30	

*Annealing at 1050°C, 4 h inclusive to check the possibility of increasing endurance

and 3). The values of the endurance of the brazed joints reached 1.5–22 h. In the test of the specimens for long-term strength at a gap of 1 millimetre, the actual long-term strengths of the solidified metal of the brazed joint was determined.

In the long-term tests of the parent metal, the specimens fractured in the lugs, indicating the low quality of the alloy in the peripheral sections of the flat along the reinforcement strip characterised by the formation of thermal fatigue cracks. The peripheral sections of the flap contained casting micro-porosity which was the reason for premature failure of the components in service.

Analysis of the results of the mechanical tests of the specimens of the brazed joint, formed using the three-composition brazing alloy with a gap 1 mm wide after various types of heat treatment (Table 1) shows that the more stable values of the ultimate strength

at room temperature were obtained for the specimens subjected to homogenising at a temperature of 1220°C, 20 min, and high-temperature annealing at 1050°C, 4 h.

The relative elongation was 2.0–7.7%. This type of heat treatment resulted in sufficiently high plasticity and strength at temperatures of start-up of the engine. Low-temperature annealing at 950°C, 2 h, reduce the strength and ductility parameters of the weld metal as a result of the precipitation of a large amount of the hardening γ' -phase and changes in the morphology of carbide phases.

Repair of specimens of the brazed joints in ZhS6K alloy

In a number of specimens, special attention was given to repair (repeated) brazing of components of the joints or already produced brazed specimens depending on the stage of preparation of the brazed joint in which shrinkage porosity was detected.

To prevent the formation of lack of brazing joints in the brazed joints, the injection filling of the technological gap 1 mm wide was carried out by manual filling, and at the top a bead of the brazing alloy, saturated with the solution of acrylic resin was deposited. High-temperature ageing at 1050°C was carried out for 5h.

The results of the tensile test of the specimens after repeated brazing were always positive (Table 4). The properties of the brazed joints, produced with the binary brazing alloy repeatedly and with the brazing alloy with 20 wt.% Ni–12% Si were compared.

Table 4. The mechanical properties of the brazed joint (repeated brazing and heat treatment)

Brazing alloy variant	Sample No.	S , mm ²	$\sigma_{0.2}$, MPa	σ_B , MPa	ε , %	Reconditioned item
11 ([#1] + 60%Rene-142)	0–7	3.94	–	665.0	0	Specimen*
	4–2	3.65	–	743.0	0	Blank*
	4–4	4.73	653.3	788.0	5.0	Specimen*
12 ([#1] + 20%HC12 + 60% Rene-142)	4–6	3.49	739.2	877.0	6.2	Blank*
	4–8	5.0	755.4	775.0	1.0	Blank*
	4–9	3.23	774.4	841.3	2.8	Single brazing

*Variant 11 and 12 were reconditioned by repeated using of variant 12 brazing alloy.

When using the binary boron-containing brazing alloy, the stable reduced values of ultimate strength (648.5–699 MPa) were obtained at a residual plasticity of 0.2–0.6%. The addition of HC12 to the brazing alloy increase the yield limit and tensile strength of the brazed joints to 719.5–745 MPa, the relative elongation was 1.0–6.2%.

The brazed joints, produced with the binary boron-containing brazing alloys, were more brittle in a stable manner in comparison with the brazed joints produced with a complex brazing alloy with HC12. The joints failed at the elasticity limit after reaching the yield limit at a stress of 650–700 MPa.

The metallographic analysis results

The composition of the brazing alloys was optimised on the basis of the results of mechanical tests of the specimens of the brazed joint together with the examination of the structure of the metal of the brazed joint. The main criterion for evaluating the quality of the brazed joint was the homogeneity of its structure whilst retaining the minimum amount of large carbide phases and complexly alloyed interdendritic eutectics. The brazing alloy No. 1 + Rene-142 and No. 1 +20% HC12+Rene-142 resulted in a sufficiently high level of the mechanical properties of the brazed joint and was closely linked with the appropriate structure of the brazed joint.

The addition of the Ni–12%Si eutectic brazing alloy to the No. 1 + Rene–142 binary alloy reduced the volume fraction of the brittle secondary phases to 4.6–5.2%, and the carbide phases were distributed in the inter-axial regions, whereas the chromium boride phases could not be found. In addition to the silicon, approximately 17 wt.% of Ni was transferred into the metal of the brazed joint from HC12. This resulted in a corresponding reduction of the degree of alloying of the brazed joint and the equilibrium in the solidified brazing alloy was displaced in the direction of formation of the γ -solution and the cementite-type phases (Ni_3B [11,12]). This was accompanied by the formation of

a distinctive dendritic-cellular structure with the cell size of approximately 30–50 μm .

Table 5 shows the phase composition of the brazed joints of two systems of the brazing alloys after brazing and two-stage heat treatment, filling the advantages of using the brazing alloy with silicon 20% No. 1 +20% HC12+60%Rene-142 (Fig. 5c, d) in comparison with 40%No. 1+60%Rene-142 (Fig. 5a, b) as regards the degree of homogeneity and uniformity of the structure.

After heat treatment, the metal of the brazed joints of the complex brazing alloy consisted of a homogeneous solution with a small number of precipitate of binary carbides MeC (microhardness 26 600 MPa). These are precipitates based on tantalum (up to 40%) and hafnium, titanium and niobium – the products of breakdown of the primary banded carbide phases and high-temperature interdendritic eutectics – are characterised by a stable structure in service in the high-temperature conditions (Table 5, Fig. 5d) [13].

When using the basic composite brazing alloy No. 1 +Rene-142 after final two-stage treatment it was not possible to avoid completely brittle fracture of the brazed joint in the tensile test as a result of the presence in the metal of the brazed joint of large carbide (carboboride) phases $\text{Me}_{23}(\text{C}, \text{B})_6$ which have the microhardness of 12 000–15 000 MPa (Table 5, Fig. 5c) and remained sufficiently stable at the homogenising temperature and acted as the areas of transcrystalline failure of the brazed joints in loading.

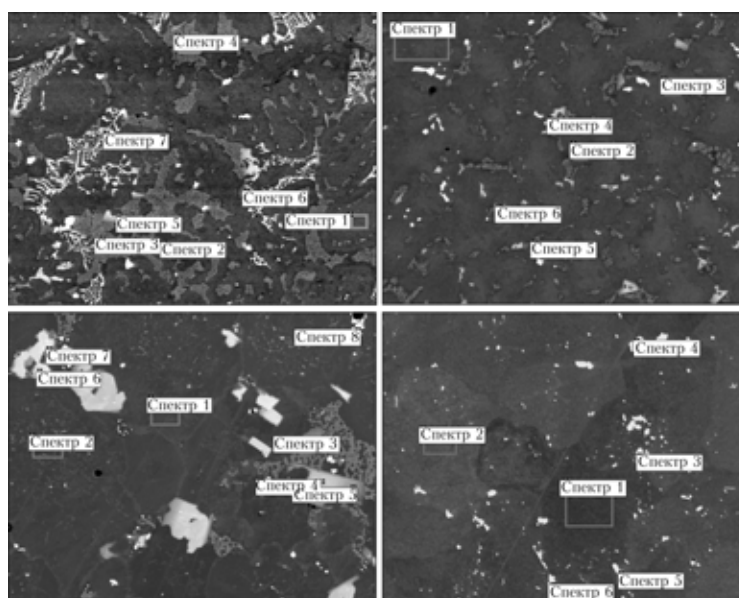
Figure 6 and Table 6 shows the structure of the brazed joint produced using the brazing alloy 20% No. 1 +20%HC12+60% Rene-142 in the specimens of the ZhS6K alloy after all types of heat treatment. The cellular nature of the solidified metal and the minimum number of the secondary interdendritic carbide phases in the joint at clearly evident. At a gap of 1 mm the joint had a dense structure without any traces of shrinkage or lack of brazing defects, and the width of the diffusion zone reached 50–70 μm .

In the initial stages of the investigations, the brazed joints are produced using the

Table 5. Microanalysis of the individual phases, forming the metal of the brazed joint, produced at a temperature of 1220°C, 20 min, using different brazing alloys with annealing and after annealing

Spec- trum No.	Mass fraction of components, %											Type of phase	HV, MPa	
	C*	Al	Cr	Co	Ni	Mo	Hf	Ta	W	Re	Si			
No. 1 + 60% Rene-142 no annealing (Fig. 5a)														
1	1.50	5.15	9.35	11.3	64.96	0.79	-	2.46	2.80	1.71	-	4015		
3	1.63	2.19	7.53	13.8	62.49	0.54	3.61	7.5	0.75	-	-	8085		
6	6.77	-	48.53	4.84	5.67	5.32	-	0.76	11.30	16.8	-	181110		
No. 1 + 60% Rene-142 after annealing at 1160°C, 2 h + 1050°C, 2 h (Fig. 5b)														
2	2.23	4.90	9.27	10.9	63.37	0.81	-	2.72	4.03	1.75	-	4200		
3	1.92	1.98	7.42	13.5	60.96	-	6.79	5.15	1.50	0.79	-	8480		
5	3.72	-	48.64	4.32	4.69	5.27	-	-	13.80	19.60	-	13180		
6	3.26	-	26.34	3.66	6.64	12.53	-	3.87	35.50	7.94	-	18785		
8	7.35	-	0.70	1.09	4.66	-	27.1	57.1	-	-	-	22150		
No. 1 + 20%HC12 + 60% Rene-142 no annealing (Fig. 5c)														
3	2.20	3.71	6.50	9.13	60.41	0.89	-	4.22	3.13	2.36	1.45	4465		
4	5.73	0.34	15.18	3.33	13.42	8.26	4.65	27.6	10.90	10.20	0.46	-		
6	3.13	0.53	4.64	10.3	66.93	-	5.82	4.45	0.92	-	3.27	6140		
No. 1 + 20% HC12 + 60% Rene-142 after annealing at 1160°C, 2 h + 1050°C, 2 h (Fig. 5d)														
2	1.97	4.16	7.14	9.58	65.96	0.28	-	3.72	3.97	2.17	1.06	4240		
4	5.96	-	3.37	5.97	13.77	13.58	-	11.1	39.90	6.39	-	19730		
6	6.76	1.78	4.02	5.93	34.63	4.96	5.83	13.4	16.50	4.20	2.00	-		

*Carbon content is qualitative because of the error of the device in determination of the type of phases


Fig. 5. Microstructure of the metal of the brazed joints, produced with the brazing alloys No. 1 + 60% Rene-142 (a, b) and No. 1 + 20% HC12 + 60% Rene-142 (c, d) in solidification (a, b, $\times 200$) and after heat treatment (c, d, $\times 500$).

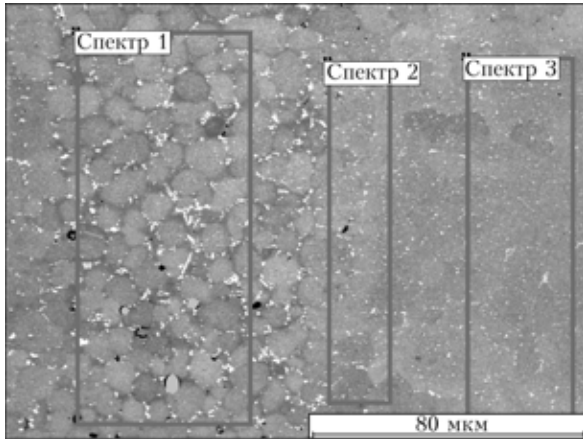


Fig. 6. Sections of x-ray spectrum microanalysis of the brazed joint, formed using 20%HC12+20% No. 1 +60% Rene-142 brazing alloy at 12 20°C, 20 min and annealing at 1160°C, 2 h +1050°C, 2 h.

No. 1 +60%Rene-142 brazing alloy with and without HC12 experiments were carried out with the variation of the conditions of final heat treatment after brazing, including homogenising at 11 60°C, 2 h, and ageing at 950°C, 2–4 h or 1050°C, 2–5 h (Fig. 7).

To produce a less distinctive heterophase structure of the metal of the brazed joints more than 1 mm wide, homogenising at 11 60°C, 2 h should be followed by high-temperature annealing (ageing) at 10 50°C, 4–5 h. In this case, the processes of dissolution of the coarse carboboride phases and of the complexly alloyed eutectics are more extensive.

The application of the silicon free brazing alloy No. 1 + 60%Rene-142 and the given conditions of final heat treatment does not result in structural homogeneity of the metal of the brazed joint: the volume fraction of the secondary carbide phases, distributed mostly in the interdendritic regions, is 11–18% (Fig. 7a, b). The presence of large carbides and boundary eutectics results in the embrittlement of the brazed joint and induces early failure under loading.

The system of the 20% No. 1 +20% HC12+60%Rene-142 brazing alloy was used as an example to show that the ageing of the brazed joint at 950°C, 2 h, increases the volume fraction of the sub-dispersed γ' -phase, but the grain boundaries contain an undesirably high number of the secondary carboboride phases (Fig. 8c, d).

After finding annealing at 1050°C, 5 h using the 20%No.1 + 20%HC12 + 60%Rene-142 brazing alloy, the liquation heterogeneity of the brazed joints which is most distinctive after metallographic etching becomes minimum (Fig. 7e,f). When using the brazing alloy in the given heat treatment (ageing at 1050°C, 4–5 h), all the areas of the brazed joint are characterised by the precipitation of the regular hardening γ' -phase, and the particle size in the brazed joint reaches 0.1–0.5 μm so that it ensures the required creep strengths of the brazed joint.

Table 6. Chemical composition of the main zones of the brazed joint, produced using the brazing alloy 20%HC12 +20%No. 1+60% Rene-142 at 1220°C, 20 min and annealing at 1160°C, 2 h +1050°C, 2 h

Investigated zones of brazed joint	Spectrum No.	%											
		Ni	Al	Co	Ti	Cr	W	Mo	Ta	C	Nb	Re	Si
ZhS6K	Alloy composition (reference)	Base	5.0...	4.0...	2.5	9.0...	1.1	3.5	-	0.1	-	-	-
			6.0	5.0	3.2	12.0	1.8	4.8					
Base metal	3	66.03	3.92	9.82	1.87	10.01	4.31	3.13	-	-	0.16	0.75	—
Diffusion zone metal	2	66.77	3.77	9.07	1.31	8.02	4.5	1.99	1.01	-	0.48	1.77	1.32
Weld metal	1	66.79	3.80	7.84	1.34	7.86	5.08	2.54	1.29	-	0.64	1.23	1.59

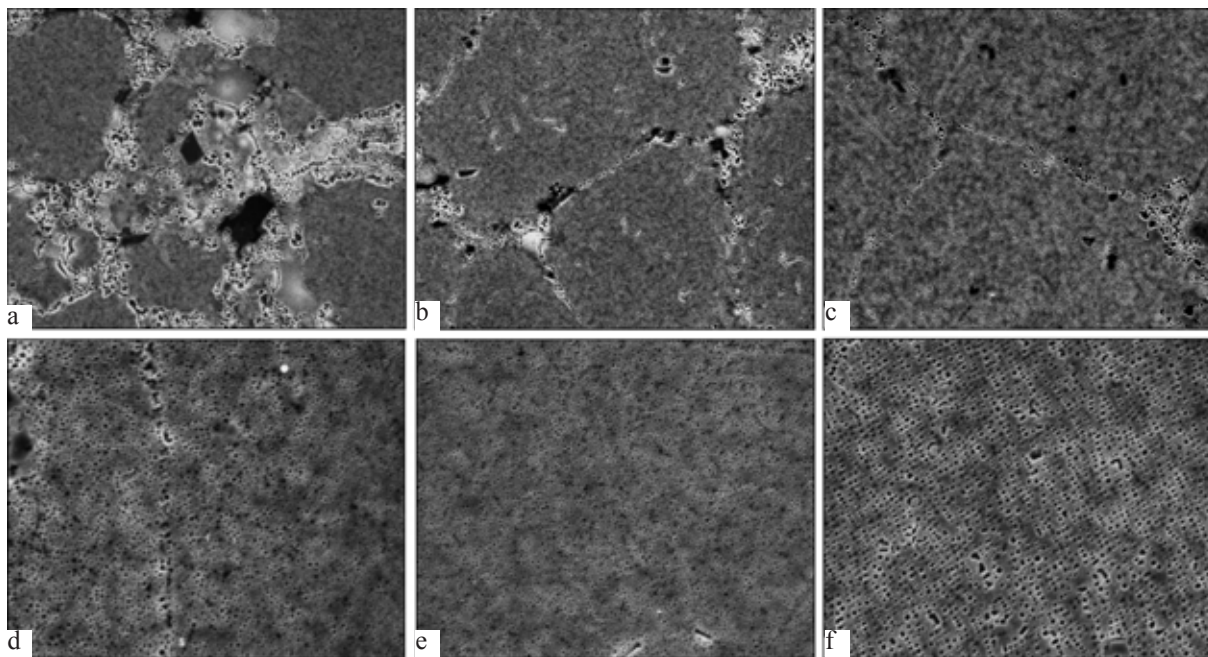


Fig. 7. (+ ')-Structure of the metal of brazed joints, formed using the brazing alloys No. 1 +60% Rene-142 (a, d) and 20% No. 1 +20%HC12+60% Rene-142 (b, c, e, f) at 1220°C, 20 min and annealing at 1160°C, 2 h: a, c, e, f) 1050°C, 5 h, c, d) 950°C, 2 h, a-c) × 500, e-f) × 1400.

Fractographic examination of the specimens of the brazed joint under tensile loading

In the laboratory conditions, the deformation process of the specimens is often reduced to uniaxial tensile loading. The most interesting results, obtained under this effect on the investigated joints, are the anomalous properties of the joints in tensile loading and the nature of strain hardening of the specimen. Special attention should be given to the elongation of the specimen.

The multiphase nature of the metal of the brazed joint and the shrinkage microporosity are the main reasons for premature failure of the brazed joint in loading. The type of fracture or the microstructure of the specimen in the fracture zone are the main sources of information for the investigated object [14].

In the analysis of the special features of failure of the brazed structure when it is necessary to determine the zone of failure in the brazed joint, the heat affected zone or the parent metal, special attention was given to examine in both parts of the fractured specimen because the examination of only

one half of the specimen is not efficient. The nature of failure of the specimens was linked with the chemical composition of the brazing alloys.

Analysis of the fracture surfaces of the specimens of the brazed joints after testing showed the presence of a mixed pattern of failure of the joint, with the transcrystalline cleavage of a large number of grains of the matrix solid solution being the dominant mechanism.

It is important to mention the identical appearance of the fracture surfaces of the specimens of the brazed joints, produced with the brazing alloys with different fillers and annealed at different temperatures. The ageing temperature has only a slight effect on the size of the carboboride phases. These phases precipitate from the melt and to change their morphology it is necessary to increase the annealing temperature and ensure long holding time in homogenising of the brazed joint.

The large segregates of the particles with an indistinctive boundary with the matrix facilitate the nucleation of cracks and reduce the fracture stress. The cavity is nucleated in the brazed joint (the weld metal) when the

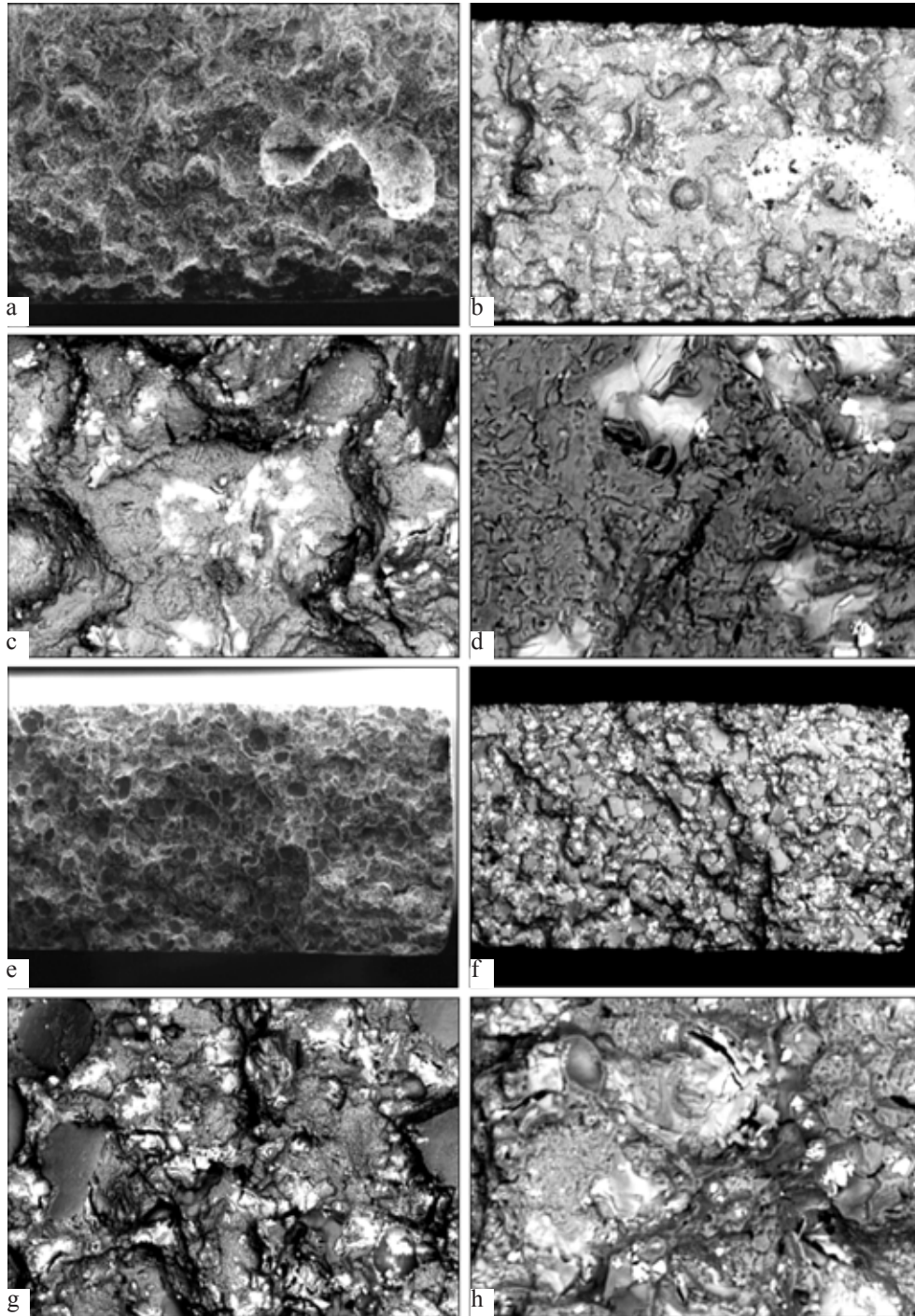


Fig. 8. Fracture surfaces ($T_{test} = 20^{\circ}\text{C}$) of the specimens, produced using the brazing alloys 20% No. 1 +60% Rene-142 (a-d) and No. 1 +20% HC12+60% Rene-142 (e-h); a, e) SEI (general view); b-d, f-h) BEI; a, b) $\times 25$, $\times 50$; e, f) $\times 25$; c, g) $\times 200$; d, h) $\times 500$.

local stressed exceeds the bonding strengths of the precipitated phases with the matrix solution. This results in separation along the contact surface. In a number of cases, the nucleation of discontinuities is detected when

the stress is sufficiently high for fracturing the particle (inclusion).

The fracture surfaces of the specimens of the brazed joints failed as a result of uniaxial tensile loading are presented in Fig. 8. The

specimens, subjected to final annealing at 1050°C, 4 h, showed relative elongation in the range from 4 to 7–10% (Table 1). Failure usually took place through the metal of the brazed joint. In most cases, the weak area was the boundary of the solidified grains along which the carboboride precipitated.

It should be mentioned that the energy of the propagating crack was rapidly absorbed at the grain boundaries [15].

The brazed joints, produced using the composite boron-containing brazing alloys No. 1+60%Rene-142 without HC12 were characterised by low plasticity (not higher than 1.7%) and, correspondingly, low strength (Fig. 3). Brittle fracture of the specimens took place either after reaching the elasticity limit or immediately above the yield limit.

The fracture surface (Fig. 8a, b) of the specimen ($\sigma = 628$ MPa, $\varepsilon = 0$) demonstrates brittle separation with single areas of the dimpled ductile failure on the surface of the individual grains. The areas of intragranular failure show particles of the carboboride precipitates. They are also found on the cleavage planes in the case of transcrystalline failure (Fig. 8c, d). The investigation of the fracture surface shows (Fig. 8d) that there is partial (incomplete) melting of the individual grain; since the brazing alloy does not contain silicon (brazing without HC12), there are areas of lack of fusion (Fig. 8a).

When adding silicon to the brazing alloy in the form of the eutectic composition Ni–12% Si (TL = 11 43°C), the dispersion of the excess carboboride phases and eutectics increases together with the increase of the uniformity of the distribution of these phases in the matrix solution of the brazed joint (Fig. 8f–h) [16].

The reduction of the amount of the coarse carboboride particles in the intragranular spaces results in dispersion hardening of the solution leading to the higher level of short-term strengths and satisfactory plasticity of the brazed joints under uniaxial tensile loading.

The maximum difference ΔG in the values of the yield limit σ_T and ultimate tensile strength $\Delta\sigma_B$ already reaches 250 MPa. This

indicates the high intensity strain hardening of the joint with the relative elongation of the specimen being 5–7% (Fig. 2).

The yield limit of the brazed joints, produced with the complex brazing alloy with 20% HC12, was slightly higher than that of the remaining specimens. Failure to place mostly through the joint metal of the specimens in the vicinity of the fusion line (Fig. 8e–h)) and the nature of failure (intergranular) was associated with the cracking of the carboboride phases along the grain boundaries and with decohesion of the particles in the matrix solution.

The discrete carboboride phases were uniformly distributed in the volume of the weld metal, and the number of the phases was minimum when the addition of HC12 was equal to 20% instead of 15% (Fig. 9a, b).

Examination of the fracture surfaces (Fig. 9e, f) showed decohesion of the carbide particle Me_6C , MeC and the matrix. Fracture zone takes place along the grains of the submatrix solution.

Evaluation of the nature of failure of the brazed joint on the longitudinal microsections shows that when using the brazing alloy No. 1+20%HC12+60%Rene-142, failure took place in most cases at the fusion line (Fig. 9). With satisfactory strain hardening, i.e., the long-term effect of the stress, fracture (cracking) was detected in the carbide interaxial phases (Fig. 9f).

The reduction of the content of the eutectic component (15% HC12) on the composite brazing alloy resulted in the formation in the metal of the brazed joint of quasi-boundary carboboride eutectics based on CrB with the structure of the type of Chinese hieroglyphs (Fig. 9, e, f). They are clearly indicated by the shades (grey, spherical form and light, almost polyhedral).

The light particle size enriched with elements with a high atomic number (tantalum, rhenium and tungsten). The grey inclusions are the carbide particles based on chromium, titanium and nickel. Thus, the increase of the mass fraction of boron in the composite brazing alloy as a result of the lower fraction

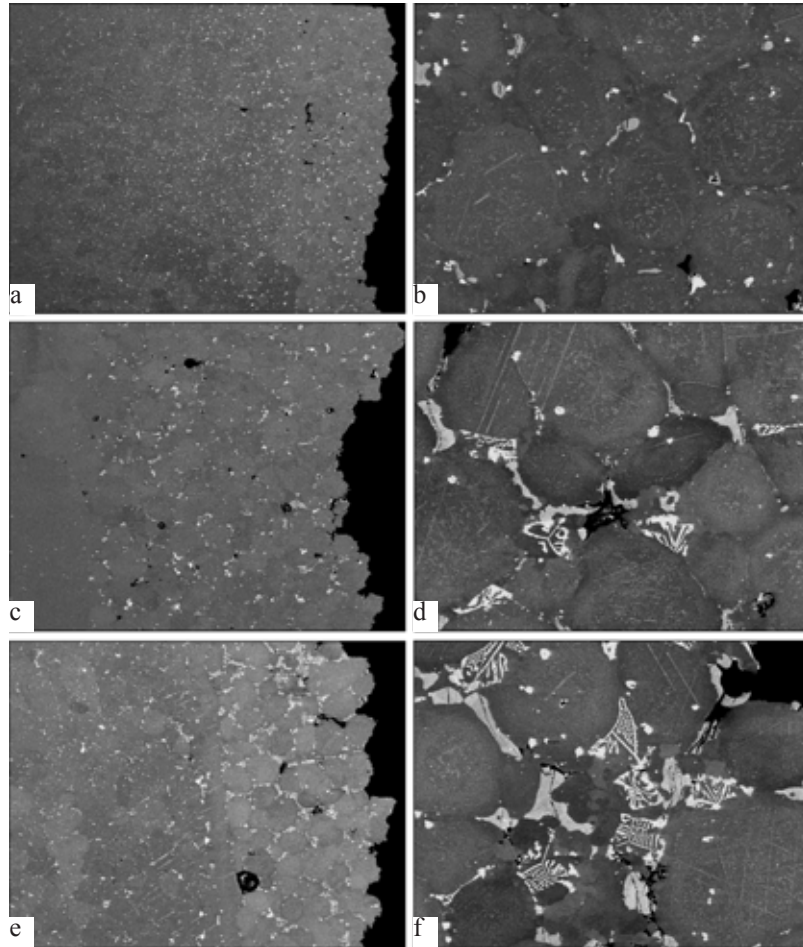


Fig. 9. Fracture and structure of the specimens of the brazed joints, produced using different types of brazing alloys, after the tensile test at 20°C: a, b) No. 1 +20%HC12+60% Rene-142; c, d) No. 1+15%HC12+60%Rene-142; e, f) No. 1+60%Rene-142, a) ×20, b, d, f) ×200, c, e) ×45.

of HC12 increases the number of the carboboride and interdendritic complexly alloyed eutectics which have a strong effect on the mechanical characteristics of the brazed joint and lead to early failure of the joints.

The addition of HC12 to the brazing alloy results, in addition to the change of the morphology of the carboboride phases and refining of these phases, in a homogeneous distribution of the particles in the volume of the polycrystals. In addition to the hardening phase Ni₃Al, the addition of silicon is accompanied by the uniform precipitation of the Ni₃B particles smaller than 1 μm. These particles are used the active sliding path and, consequently, the fracture stress increases [15].

The refining of the precipitated phases

reduces the length of the slip band and, consequently, reduces the stress in front of the particles or grain boundary. This measure increases the plasticity of the brazed joints.

To produce the fine grains of the brazed joints, it is necessary to increase the cooling rate in practice.

Creep resistance of the brazed joints in the ZhS6K alloy

The holding of the brazed joint of ZhS6K alloy in air for 70 hours at 1000°C resulted in a low degree of oxidation of the surface layers of the metal. The oxide film at a relatively high chromium (more than 15 wt.%) and aluminium content (more than 3 wt.%) in the alloy consisted mostly of Al₂O₃; the

width of frontal cooling was 10–30 μm and of local cooling almost 50 μm .

A subsurface layer of the solid solution, fully depleted in the hardening γ' -phase approximately 20 μm wide, was found below the layer of the oxidation products. The main role in the oxidation process of high creep strength nickel alloys is played by the mass ratio of chromium and aluminium [17].

The process of oxidation of the creep-resisting alloy is complicated and differs in the individual sections of the oxidised surface. Initial oxidation of the alloy with the formation of the separating oxide films with

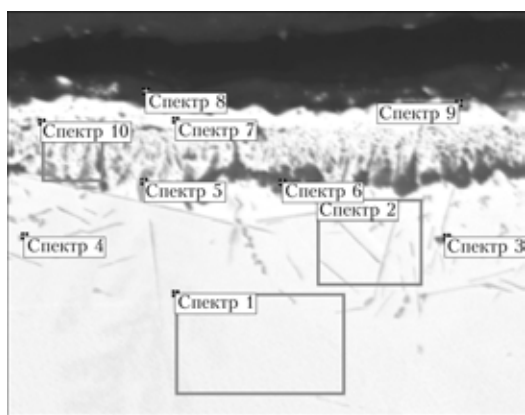


Fig. 10. Section of x-ray spectrum microanalysis of the scale layer on the surface of the specimen of the ZhS6K alloy after isothermal annealing in a furnace at 1100°C, 17 h, $\times 120$.

thermodynamically stable oxide phases Cr_2O_3 and Al_2O_3 formed below these films makes it possible to prevent the fracture consequences as a result of the formation of a continuous protective internal oxide film based on Al_2O_3 ensuring satisfactory functioning of the creep resisting alloy in high-temperature service. However, in the case of early cleavage of the protective film, the alloys subjected to internal oxidation and also the formation of aluminium oxides and titanium nitrides to a depths of up to 50 μm or more (Fig. 10, Table 7).

In comparison with the brazed ZhS6K alloy, the metal of the brazed joint is characterised by high oxidation resistance. The higher content of chromium, tantalum, rhenium and hafnium in the metal of the brazed joints ensures high creep resistance of the joints.

Hafnium has a beneficial effect on the morphology of the precipitated carbide phases and in oxidation partially diffuses into the subsurface layer (Fig. 11, Table 8) with the formation of stable oxides under the film of spinels NiCr_2O_4 and NiAl_2O_4 and this complicates the diffusion of aluminium to the surface and leads to the formation of a barrier which delays the growth of the oxide film.

Since the NiCr_2O_4 and NiAl_2O_4 spinels are mutually soluble and compatible, slow-grow-

Table 7. Chemical composition of the individual oxide and nitride phases in the scale layer and on the surface layer of the flap made of ZhS6K alloy as a result of isothermal oxidation in a furnace at 1000°C, 70 h

Spectrum No.	Mass fraction of components, %										
	N	O	Al	S	Ti	Cr	Fe	Co	Ni	Mo	W
1	—	0.97	3.12	—	2.07	7.63	1.35	9.08	66.74	3.92	5.11
2	—	—	2.89	—	3.97	5.19	2.25	8.89	66.01	5.29	5.50
3	23.82	—	32.97	—	7.41	2.00	1.12	3.69	26.19	1.31	1.51
4	11.29	—	1.34	—	17.18	4.49	1.78	6.27	49.69	4.34	3.62
5	—	24.45	19.77	—	3.25	0.71	1.66	5.11	37.84	3.99	3.24
6	—	49.23	40.38	—	5.62	0.44	—	0.48	2.82	0.72	0.31
7	—	—	—	—	—	0.66	3.42	8.81	69.62	9.19	8.28
8	—	57.36	16.49	1.93	1.63	12.34	8.26	—	11.98	—	—
9	—	46.05	3.24	—	1.38	40.17	0.45	0.85	6.98	0.89	—
10	—	15.40	12.38	—	1.51	0.79	2.38	6.84	49.72	5.76	5.22

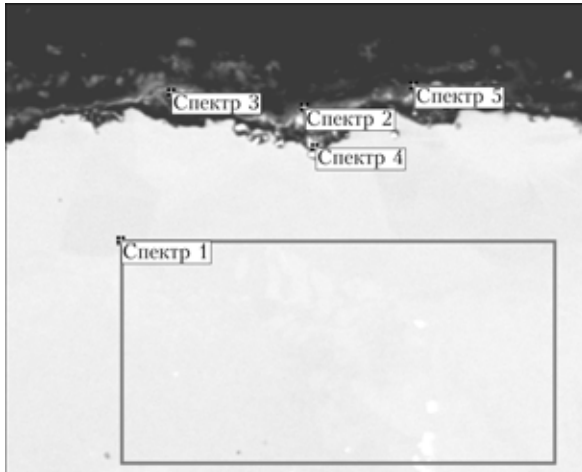


Fig. 11. Sections of x-ray spectrum microanalysis of the scale layer on the surface of the brazed joint No. 1+20% HC12+60% Rene142 in the specimen of the ZhS6K alloy is the result of isothermal oxidation in a furnace at 1000°C, 70 h, $\times 120$.

ing phases with the formation of the internal continuous oxide film based on Al_2O_3 form.

On the basic material of the flap (ZhS6K alloy) in comparison with the metal of the brazed joint the thickness of the scale layer was approximately twice as large. Comparing the brazing alloys with different types of fillers, it may be concluded that in the case of Rene-142 the morphology of the carbide phases and the distribution of these phases in the brazed joints are more favourable and this guarantees the frontal oxidation of the surface of them metal of the brazed joint to a depth not exceeding 10 μm .

Since the efficiency of the brazed joint is controlled by the width of the technological gap in the solidification of the molten brazing alloy (as the width of the gap and the volume of the melt increase, the probability

of formation of brittle centrally axial carboboride eutectics in the solidifying brazed joint increases [18]), it has been decided to insert high-quality fragments into the body of the component in the repair of the flaps. These fragments replace the damaged areas with cluster-like branched thermal fatigue cracks. The width of the gap did not exceed 200 μm .

Figure 12 shows the external appearance of such a fragment, brazed with the complex brazing alloy with the binary filler produced from the powders of nickel creep resisting alloys. The technology of reconditioning the components using boron- and silicon-containing additions is standard.

Table 9 shows the strength characteristics of the reference specimens, produced together with the fragment of the flap in a single technological charge.

As indicated by Fig. 12, the formation of the brazed joint on the components, reconditioned by brazing, is quite satisfactory.

The cylindrical test of the specimens of the brazed joints in cantilever bending shows that the fatigue resistance of the metal of the brazed joints with the technological gap of up to 150–180 μm corresponds to the fatigue resistance of the initial pore-free ZhS6K alloy and equals approximately (400 \pm 20) MPa at a test base of $20 \cdot 10^6$ cycles at a temperature of 20°C.

Conclusions

1. The results of the tests of the structure and physical–mechanical properties of the brazed joints in the ZhS6K alloy (material of

Table 8. Mass fraction of the components in structural components in the scale layer on the surface of the brazed joint No. 1+20%HC 12-60% Rene-142 of the specimens of the ZhS6K alloy as a result of isothermal oxidation in a furnace at 1000°C, 70 h

Spectrum No.	O	Al	Si	Ti	Cr	Fe	Co	Ni	Nb	Mo	Hf	Ta	W	Re
1	—	2.98	1.30	0.64	5.86	0.46	7.69	70.51	0.24	1.67	—	4.37	3.07	1.20
2	45.32	12.28	3.14	4.17	16.79	—	3.06	11.31	0.29	0.24	2.06	—	1.10	0.25
3	43.70	4.36	5.07	1.67	9.05	—	2.03	22.6	0.20	0.74	2.66	6.62	1.32	—
4	27.13	11.85	—	0.58	1.16	—	—	3.79	0.69	0.15	48.75	4.18	—	1.72
5	43.67	6.97	1.81	4.47	14.52	—	1.56	15.69	0.24	0.76	2.50	5.28	2.54	—

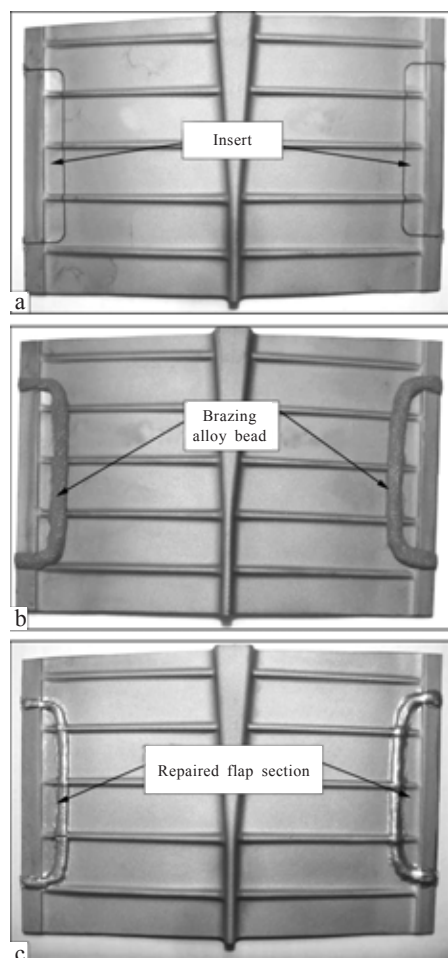


Fig. 12. Fragment of the flap of the regulating nozzle of the aircraft gas turbine engine after a repair by brazing; the flap prior to (a, b) and after brazing (c).

the flap of the regulating nozzle of the aircraft gas turbine engine) shows that the application has the basic boron-containing brazing alloy NiCoCrAl-2.5%B (No. 1) + 60%Rene-142 results in the satisfactory strength characteristics of the brazed joints with minimum plasticity. The specimens failed after reaching the yield limit as a result of the presence in the structure of the brazed joints of a large number of the carboboride and complexly alloyed interdendritic eutectics (up to 11–20 vol.%) which remain in the metal after finishing two-stage heat treatment.

2. It has been shown that the addition of the Ni-12%Si (HC12) eutectic addition to the No. 1+60%Rene-142 brazing alloy ensures sufficiently high fluidity of the melt of the composite the brazing alloy, efficient

Table 9. Strength characteristics of the reference specimens in brazing of fragments of the flap (ZhS6K alloy) with the complex brazing alloys with binary fillers

Sample No.	S , mm ²	$\sigma_{0.2}$, MPa	σ_B , MPa	ϵ , %	$\Delta\sigma/\epsilon$
1	4.12	707.0	821.5	4.8	23.8
2	4.31	710.0	758.0	2.2	21.8
3	4.13	745.2	843.2	3.0	31.0
4	4.01	795.0	917.4	6.7	18.0
5	5.54	752.5	796.8	1.7	26.0
6	4.29	754.0	882.7	6.8	18.8
7	4.70	795.0	878.5	3.2	26.1

filling of the gaps, prevention of shrinkage and microporosity in the brazed joints and reduces the reactivity of the boron-containing brazing alloy.

3. The results of the tensile test on the brazed joints, produced with a complex brazing alloy containing simultaneously two depressants (boron and silicon) in the optimum amount (0.5 and 2.4%) confirmed the considerably higher plasticity in loading and the stability of the strengths characteristics of the brazed joints in ZhS6K alloy on the level of (0.85–0.97) B. This result shows that the complex brazing alloy of the 20% No. 1 + (15–20)%HC12+60%Rene-142 can be used universally for the formation of the brazed joints in cast nickel alloys.

4. The results of the tests of the brazed joints in air at 1000°C for 70 h showed high oxidation resistance of the metal of the brazed joint, in particular of the brazing alloy No. 1+20%HC12+ 60%Rene-142 in comparison with the brazed metal of the base ZhS6K. The width of the zone of frontal oxidation of the base was 30 μm , local oxidation up to 50 μm . The subsurface zone, with no aluminium, was 20–30 μm wide. The metal of the brazed joint was oxidised to a depth not greater than 10 μm using the effective alloying complex of the alloy-filler – René-142.

References

1. Petukhov, A.N., Fatigue strength of components of gas turbine engines, Mashinostroenie, Moscow, 1993.
2. Mattheij J.H.G., Mater. Sci. Technol., 1996, No. 8,

- 608–612.
3. Duvall D.S., et al., *Welding J.*, 1974, No. 4, 203–214.
 4. Rabinkin A., *Sci & Technol. of Welding & Joining*, 2994, No. 3, 181–199.
 5. Klyuchnikov I.M., in: *Brazing in construction of advanced technology components*, Moscow, 1997, 151-155.
 6. Khorunov V.F., *fundamentals of brazing scene wall structures produced from high alloyed steels*, Naukova Dumka, Kiev, 2008.
 7. Wikstrom N.P., et al., *Mater. Sci. & Eng.*, 2006 A417, 299-309.
 8. Kablov E.H., *Cast blades of gas turbine engines*, Moscow Institute of Steel and Alloys, Moscow, 2001.
 9. Xhessness R.P. and Xu R.R., Patent 6.454.885 USA, IC17 C 22 C 19/96, Nickel diffusion brazed-alloy and methods for repair of superalloys.
 10. Malashenko I.S., et al., *Sovremennaya Elektrometallurgiya*, 2006, No. 4, 26-42.
 11. Kurenkova V.V. and Malashenko I.S., In: *Surface engineering. New powder the composite materials. Welding, proceedings of the international conference*, Minsk, 2009, volume 2, 209-217.
 12. Goldstein H.G., *Interstitial alloys*, in two volumes, Mir, Moscow, 1971.
 13. Shalin R.E., et al., *Single crystals of nickel creep-resisting alloys*, Mashinostroenie, Moscow, 1997.
 14. Balter M.A., et al., *Fractography - a means of diagnostic self fracture of components*, Mashinostroenie, Moscow, 1987.
 15. Gerland G., *Microstructural aspects of failure of two-phase alloys*, in: *Fracture*, volume 7, Mir, 1976, 472-512.
 16. Kurenkova V.V., In: *Adhesion of melts and brazing of materials*, 2008, No. 41, 63-87.
 17. Vasilevski V.V. and Malashenko I.S., *High-temperature oxidation. Creep resisting alloys*, Metallurgiya, Moscow, 1976, 266-293.
 18. Miglietti W.M., *Diffusion bonding of gaps*, Pat. 6.520.401, B1 USA, IC17 B 23 K 20/22,